

PROCESSING, CHARACTERISTICS AND PROPERTIES OF CNT-ENHANCED PA

66

By

NOFEL ZUHIER WHIEB

A dissertation submitted to the

Graduate School-New Brunswick

Rutgers, The State University of New Jersey

In partial fulfillment of the requirements

For the degree of

Doctor of Philosophy

Graduate Program in Materials Science Engineering

Written under the direction of

Bernard H. Kear

And approved by

New Brunswick, New Jersey

October 2017

ABSTRACT OF THE DISSERTATION

Processing, Characteristics and Properties of CNT-Enhanced PA 66

By Nofel Zuhier Whieb

Dissertation Director: Professor Bernard H. Kear, Ph.D.

In this research, structure-properties-processing relationships of melt-processed CNT-PA 66 composites are investigated. Using a novel high-shear mixing device, efficient dispersal of CNTs in molten PA 66 is achieved, forming a well-bonded composite that displays enhanced mechanical properties. Post-fabrication heat treatment of some graphite-polymer composites also changes properties in new and unexpected ways.

Observations by SEM and TEM indicate good bonding between CNTs and PA 66. DSC measurements show a second crystallization peak in the cooling curve, as the CNT content in PA 66 matrix increases from 1 to 5 wt. %. This new type of crystallization becomes a dominant feature in the range of 6-8 wt. % CNTs. Such interactions correlate with changes in elastic modulus and impact strength. FTIR analysis shows a steady increase in peak intensities for 1-5 wt. % CNT-PA 66 composites, until at 6 wt. % there is a sudden decrease in Amide I and II stretching peak intensities, accompanied by a shift to lower wave numbers. This behavior may be attributed to transformation of the original matrix structure to a new C-C rich bonded crystalline state.

Three-point bend tests show a decrease in elastic modulus up to 3 wt. % CNTs in PA 66 due to minor degradation of the polymer matrix. At higher CNT concentrations, covalent bonding between fractured-ends of CNTs and polymer matrix occurs, which

increases elastic modulus via a load transfer mechanism. At even higher CNT concentrations, a bridging effect occurs between adjacent covalently-bonded regions that increases impact strength. Eventually this results in a fully cross-linked structure of high stiffness and low impact resistance. As might be expected, peak stress at fracture shows an inverse relationship with stiffness.

A two-step heat treatment is used to modify the structure and properties of 35 wt. % graphite-PEEK composite. It involves heating the composite at 200°C for 20 hours and then at 380°C for 18 hours. Examination of samples by TEM and XPS showed some polymer has gasified and the remaining polymer is a well-crystallized PEEK. 35 wt. % graphite-PA 66 composite was heat treated at 280°C for 24 and 48 hours. A new highly crystalline phase led to increase in elastic modulus was investigated by DSC and FTIR. This opens new opportunities to enhance properties and performance of injection-molded components or parts.

DEDICATION

To my family; Mother, Father

Ameer, Zeineb, Ahmed

To my friends.

Thank you.

ACKNOWLEDGEMENTS

Here, I would like to express my deep gratitude to my dissertation defense committee, chaired by Professor Bernard H. Kear, and including Professor Thomas J. Nosker, Professor Thomas Tsakalakos, Professor Jennifer K. Lynch, Professor Larry McCandlish and Professor Stephen Tse.

Professor Kear has been particularly helpful. He kept encouraging me during the research and sharing his insights and assistance at every step of the way. For his inspiring role, unwavering seeking of excellence, and extraordinary character as research advisor, I am sincerely thankful.

I would like to express my profound appreciation to Professor Nosker, Professor Lynch and Professor McCandlish for their immense help, supportive advice, and instruction throughout the entire research project. They went beyond being members of my dissertation committee by providing access to their laboratories, resources, and most importantly to their knowledge.

I would like to acknowledge and thank Arya Tawatia and Justin Hendrix from Professor Nosker's research group for their constant help in completing the research requirements. I would like to thank Professor Stephen Tse from the Department of Mechanical and Aerospace Engineering and members of his research group: Zhizhong Dong, Gang Xiong and Mustafa Mozael for their help in materials characterization.

I would like to thank the Department of Materials Science and Engineering, Department of Mechanical and Aerospace Engineering, and Chemistry Department for providing access to their laboratories and equipment.

Last but not least, I would like to thank my family and friends for their support and encouragement, and to you all I express my deepest appreciation.

Table of Contents

Abstract.....	ii
Dedication.....	iv
Acknowledgements.....	v
Table of Contents.....	vii
List of Tables.....	xi
List of Figures.....	xii
Abbreviations.....	xvii
1. Introduction.....	1
1.1. Processing and Characteristics of MWCNT-Reinforced PA 66 Composites.....	1
1.1.1. History.....	1
1.1.2. Carbon Nanotube-Reinforced Polymer Composites.....	2
1.2. Post-Fabrication Heat Treatment of Graphene-Reinforced Polymer Matrix Composites.....	5
2. Overview and Literature Survey.....	12
2.1. Processing and Characteristics of MWCNT-Reinforced PA 66 Composites.....	12
2.1.1. Overview.....	12
2.1.2. Literature Survey.....	13

2.1.2.1. Structure and Properties of Carbon Nanotubes.....	13
2.1.2.2. Carbon Nanotubes CNTs Synthesis.....	16
2.1.2.3. Processing of CNT-Reinforced Polymer Composites.....	17
2.2. Post-Fabrication Heat Treatment of Graphene-Reinforced Polymer Matrix Composites.....	23
3. Experimental Procedure.....	28
3.1. Processing of MWCNT-Reinforced PA 66 Composites.....	28
3.1.1. Starting Materials and Characteristics.....	28
3.1.1.1. Multi-Wall Carbon Nanotubes.....	28
3.1.1.2. Poly Amide 66 (PA 66).....	30
3.1.2. Batch Mixer.....	33
3.1.3. Mixing Procedure.....	35
3.2. Procedure of Heat Treatment of Graphite-Polymer Composites.....	36
3.2.1. 35 wt. % Graphite-PEEK Composite.....	36
3.2.2. 35 wt. % Graphite-PA 66 Composite.....	37
4. Analytical Instruments.....	38
4.1. Scanning Electron Microscope.....	38
4.2. Differential Scanning Calorimeter.....	40

4.3. Rheometer.....	42
4.4. X-Ray Diffraction Unit.....	44
4.5. Fourier Transform Infrared Spectroscopy.....	46
4.6. Universal Testing Machine.....	48
4.7. Impact Testing Machine.....	49
4.8. X-ray Photoelectron Spectrometer.....	50
4.9. Transmission Electron Microscope.....	52
5. Results and Discussion-Processing and Characteristics of MWCNT-Reinforced PA 66 Composites.....	55
5.1. DSC tests and results.....	55
5.2. FTIR tests and results.....	62
5.3. Mechanical Properties.....	69
5.3.1. Three-Point Flexural Test.....	70
5.3.2. Impact resistance.....	72
5.4. Morphology and Fracture Behavior.....	73
5.5. TEM Imaging.....	78
5.6. XRD Analysis.....	79

6. Post-Fabrication Heat Treatment of GNF-Polymer Composites.....	81
6.1. Post-Fabrication Heat Treatment of 35 wt. % GNF-PEEK Composite.....	81
6.1.1. Influence of Post-fabrication Heat Treatment.....	82
6.1.2. Chemical resistance.....	83
6.1.3. FESEM Observations.....	83
6.1.4. TEM Observations.....	85
6.1.5. XPS Analysis.....	89
6.2. Post-Fabrication Heat Treatment of 35G-PA 66 Composite.....	93
6.2.1. Tensile Properties.....	93
6.2.2. DSC Analysis.....	95
6.2.3. FTIR Analysis.....	98
7. Conclusions and Future Work.....	100
7.1. Conclusions.....	100
7.2. Recommendations for Future Work.....	104
References.....	106

List of Tables

Table 2.1: Mechanical properties of CNTs and some common materials.....	15
Table 4.1: AR 2000 Rheometer features and specifications.....	42
Table 4.2: 4100 FTIR Spectrometer features and specifications.....	46
Table 4.3: MTS Q Test universal testing machine features and specifications.....	48
Table 4.4: Instron POE2000 impact machine features and specifications.....	49
Table 4.5: K-Alpha XPS features and specifications.....	50
Table 5.1: FTIR assignments of peaks for PA 66.....	63

List of Figures

Figure 1.1: Functionalization of CNTs and reaction with amines or alcohols.....	4
Figure 2.1: Wrapping a graphene sheet to form a SWNT.....	14
Figure 2.2: Root and tip growth mechanisms of MWCNTs.....	17
Figure 2.3: Left; shows one end of a single MWCNT is attached to the AFM tip and the other is embedded in the solid polymer matrix. Right; shows the process of pull-out of MWCNT. The critical force needed for pull-out was recorded by AFM.....	19
Figure 3.1: A series of SEM images arranged from low to high magnification showing that a typical as-produced particle consists of loosely-agglomerated multi- wall CNTs (MWCNTs).....	29
Figure 3.2: XRD spectra of MWCNT powder showing that single crystallization form is dominant throughout the powder.....	30
Figure 3.3: DSC curves for PA 66 showing that melting and crystallization temperatures are 261.5°C and 225.2°C, respectively.....	31
Figure 3.4: A plot of G' (Pa), G'' (Pa) and δ (degrees) vs. % strain in a stress sweep. The linear viscosity region occurs between 0.1-1% strain.....	32
Figure 3.5: A plot of G' (Pa), G'' (Pa) and δ (degrees) vs. angular frequency (rad/s) in a frequency sweep at 0.4% strain.....	32
Figure 3.6: Viscosity (Pa.s) vs. shear rate (1/s) of PA 66.....	33

Figure 3.7: Laboratory-scale batch mixer used to prepare MWCNT-PA 66 composites.....	34
Figure 3.8: Heat treatment procedure of 35wt. % GNF-PEEK composite.....	37
Figure 4.1: Zeiss-Sigma scanning electron microscope.....	39
Figure 4.2: Schematic of a scanning electron microscope.....	39
Figure 4.3: Q 1000 differential scanning calorimeter.....	41
Figure 4.4: AR 2000 rheometer.....	43
Figure 4.5: Voigt model illustrates the behavior of a polymer under a creep test, and Maxwell model illustrates the behavior of a polymer under a stress- relaxation test.....	44
Figure 4.6: Incident and diffracted beams on a crystal plane.....	45
Figure 4.7: 4100 ExoScan FTIR unit.....	47
Figure 4.8: MTS Q Test 25 universal testing machine.....	48
Figure 4.9: Instron POE2000 low energy pendulum tester.....	49
Figure 4.10: Thermo Scientific's K-Alpha X-ray photoelectron spectrometer.....	51
Figure 4.11: Photoelectric effect (up) and XPS work principle (down).....	52
Figure 4.12: JEOL 2010F scanning transmission electron microscope.....	53
Figure 4.13: Ray diagram for a transmission electron microscope.....	54

Figure 5.1: DSC curves of heat flow (W/g) vs. temperature (°C) for increasing wt. % MWCNTs in PA 66.....	59
Figure 5.2: DSC curves of heat flow (W/g) vs. temperature (°C) for the (a) first heat, (b) cool, and (c) second heat.....	60
Figure 5.3: a) first melting, b) crystallization, and c) second melting temperatures for PA 66 and MWCNT-PA 66 composites.....	61
Figure 5.4: FTIR spectrum for PA 66, plotting absorbance vs. wave number (cm ⁻¹).....	62
Figure 5.5: FTIR spectra showing absorbance vs. wave number (cm ⁻¹) for increasing wt. % MWCNTs in PA 66.....	66
Figure 5.6: A collective draw of FTIR spectra showing absorbance vs. wave number (cm ⁻¹).....	67
Figure 5.7: Manually-operated injection molder.....	69
Figure 5.8: Bar chart showing flexural modulus (GPa) vs. wt. % MWCNTs in PA 66.....	71
Figure 5.9: Bar chart showing peak stress (MPa) vs. wt. % MWCNTs in PA 66.....	71
Figure 5.10: Bar chart showing impact resistance (J/m) vs. wt. % MWCNTs in PA 66....	73
Figure 5.11: Low magnification FESEM images of fractured surfaces, showing wave-like patterns of micro-cracks.....	75

Figure 5.12: High magnification images of fractured surface of 5 wt. % MWCNT-PA 66 composite showing a series of micro-cracks and uniform distribution of MWCNTs.....	75
Figure 5.13: High magnification images of MWCNTs in (a) 3 wt. % composition, and (b) 7 wt. % composition.....	76
Figure 5.14: A series of low (top left) to high (bottom right) magnification images of 8 wt.% MWCNTs in PA 66 showing isolated regions where the MWCNT concentration is much lower than the average, indicating incomplete mixing in these regions.....	77
Figure 5.15: TEM micrographs of (a) multi-wall CNT in intimate contact with amorphous PA 66 matrix, and (b) dark-contrasting regions of higher density crystalline PA 66 in an amorphous matrix.....	78
Figure 5.16: XRD curves of MWCNTs, PA 66, and 1-8 wt. % MWCNT-PA 66 composites.....	80
Figure 6.1: Samples of 35G-PEEK after immersion in 98% sulfuric acid for 24 hours: after heat treatment (left), and before heat treatment (right), showing that the post-annealed sample resists chemical attack.....	84
Figure 6.2: FESEM images of a sample of 35G-PEEK after post annealing, showing (a) textured GNF structure, and (b) evidence for edge-covalent bonding between GNFs and PEEK matrix.....	84

Figure 6.3: (a) TEM image of few-layer graphene flakes, mostly overlapping,(b) and (c) electron diffraction patterns taken at locations A and B in (a).....	86
Figure 6.4: TEM images of (a) amorphous PEEK and (b) crystalline PEEK, and their corresponding electron diffraction patterns.....	87
Figure 6.5: TEM image of as-processed 35G-PEEK, showing a graphite flake in (a), which at higher magnification in (b) appears to be decorated with crystalline PEEK and (c) its corresponding electron diffraction pattern.....	88
Figure 6.6: TEM images with increasing magnification, showing evidence for crystallization of PEEK as a major phase.....	89
Figure 6.7: XPS scans of (a) PEEK, (b) as-processed 35G-PEEK and (c) heat treated 35G-PEEK.....	90
Figure 6.8: XPS (C1s) scans of (a) PEEK, (b) as-processed 35G-PEEK and (c) heat treated 35G-PEEK.....	91
Figure 6.9: Elastic modulus and break stress for 35G-PA 66 Composite, without heat treatment and with heat treatment at 280°C for 24 and 48 hours.....	94
Figure 6.10: Shows (a) first heating - (b) cooling – (c) second heating curves for 35G-PA 66 composite; without heat treatment, with heat treatment at 280°C for 24 hours, and 48 hours.....	97
Figure 6.11: FTIR data for 35G-PA 66 composite: (0 hr) without heat treatment, (24 hr) after heat treatment at 280°C for 24 hours and (48 hr) after heat treatment at 280°C for 48 hours curves.....	99

ABBREVIATIONS

PA 66.....	Polyamide 66
DSC.....	Differential Scanning Calorimetry
XRD.....	X-Ray Diffraction
FTIR.....	Fourier Transform Infrared
CNT.....	Carbon Nanotube
SWCNT.....	Single-Wall Carbon Nanotube
MWCNT.....	Multi-Wall Carbon Nanotube
TEM.....	Transmission Electron Microscopy
(FE)SEM.....	(Field Emission) Scanning Electron Microscopy
CF-PMC.....	Carbon Fiber-Polymer Matrix Composite
GNF.....	Graphene Nanoflake
SAXS.....	Small Angle X-ray Scattering
PE.....	Polyethylene
PET.....	Polyethylene Terephthalate
PC.....	Polycarbonate
AFM.....	Atomic Force Microscopy

CVD.....	Chemical Vapor Deposition
PTFE.....	Polytetrafluoroethylene
PAN.....	Polyacrylonitrile
PMMA.....	Polymethyl methacrylate
PSR.....	Polysulphide Rubber
UPE.....	Unsaturated Polyester
RPM.....	Revolutions per Minute
EDS.....	Energy Dispersive Spectroscopy
EBSD.....	Electron Backscatter Diffraction
EPMA.....	Electron Probe Micro-Analyzer
XPS.....	X-ray Photoelectron Spectrometer
FE-STEM.....	Field-Emission Scanning Transmission Electron Microscopy
EELS.....	Electron Energy Loss Spectroscopy

Chapter 1

Introduction

1.1 Processing and Characteristics of MWCNT-Reinforced PA 66 Composites

1.1.1 History

Starting in the 1970's, a major effort to develop a new class of lightweight composites for structural applications was initiated. From the outset, the emphasis was placed on the development of methods to fabricate strong and stiff carbon fibers for reinforcement of polymers [1]. This effort culminated in the processing of continuous carbon fibers from polymer precursors, e.g. rayon, polyacrylonitrile and mesophase pitch, and their subsequent incorporation into polymeric matrices. Today, high performance carbon fiber-reinforced polymer matrix composites (CF-PMCs) are available commercially, and have become the materials of choice for a host of applications where high specific strength and stiffness offer performance advantages; for example, in sporting goods, transportation vehicles and aerospace systems. Presently, as manufacturing costs are progressively reduced, applications for high performance CF-PMCs continue to expand.

To enhance crystallinity and to reduce defects in the carbon fibers, chemical vapor synthesis methods, utilizing transition-metal catalyst particles to facilitate fiber growth, have been widely studied. The mechanism of vapor-phase growth of carbon fibers was established in the early 1970's [2]. During subsequent research, very small diameter filaments were reported [3]. Later, growth of hollow filaments and a thickening mechanism were described [4, 5]. After the discovery of C₆₀ fullerene in 1985 [6], and a follow-up workshop on carbon-carbon composites in 1990, discussions led to speculation on the existence of carbon nanotubes. In 1991, it was suggested that carbon nanotubes

may be end-capped with fullerene hemispheres [7]. But the breakthrough came with the direct TEM observations of carbon nanotubes (hereafter CNTs) by Ijima [8]. Since then, research on carbon nanotube-reinforcement of polymers has progressed rapidly; even so, property improvements have fallen short of expectations.

1.1.2 Carbon Nanotube-Reinforced Polymer Composites

A carbon nanotube-reinforced polymer matrix composite (CNT-PMC) differs from a conventional carbon fiber-reinforced polymer matrix composite (CF-PMC) in that there is a much higher interface area between reinforcing carbon and polymer matrix. Calvert et al. discussed the advantages of a CNT-PMC, and proposed that introducing a uniform distribution of CNTs into a polymer matrix should yield property improvements exceeding that predicted by the rule of mixtures [9].

CNTs are considered to be ideal reinforcing materials for polymer matrices because of their high aspect ratio, low density, remarkable mechanical properties, and good electrical and thermal conductivities [10, 11]. However, property improvements achieved have not been significant so far, apparently due to poor interfacial CNT/polymer bonding and severe CNT agglomeration [12]. Many methods have been proposed to overcome these limitations, most of which involve chemical functionalization of CNT surfaces to achieve better nanotube dispersion and wetting with polymer matrices [13]. Surface functionalization of CNT with chemical groups can give rise to non-covalent or covalent bonding. Non-covalent bonding of specific groups to CNT surfaces may involve physical adhesion and/or wrapping of polymer molecules, so that structural properties of the composite are relatively changed. On the other hand, in the event that covalent or chemical bonding (“grafting”) of polymer molecules to CNTs occurs, the structural

properties are enhanced. This type of functionalization necessarily breaks the graphitic bonds in the CNT walls to enable attachment of new polymeric groups to its surface.

In general, the grafting method involves reacting polymer chains with the surfaces of as-received, oxidized or previously functionalized CNTs. The objective is to attach radical or carbanion groups to the CNT double bond. Since there is high strain associated with the sp^2 hybridized carbon atoms in a CNT, due to the curvature of its atomic structure, the energy needed to convert these atoms to sp^3 hybridization is reduced, making it easier to establish addition reactions. To take advantage of this behavior, it is necessary to create defects in the CNT surface to attach to carboxylic acid groups, thus allowing covalent bonding with the polymer chains [13]. In order to accomplish functionalization by this method, it is often necessary to oxidize the CNT surface and to form a polymeric transient that acts as a bridge to the polymer matrix. Many methods have been investigated to create such bridges, Figure 1.1, including ester or amide linkages, nucleophilic addition/coupling reactions, and sonochemical reactions [14].

Instead of attaching CNTs to pre-existing polymers, another approach involves polymerization of monomers on initiators (like thermosets), which are low molecular weight groups covalently bonded to a CNT surface using functionalization reactions for small molecules. These reactions include acid-defect group reactions and CNT-sidewall functionalization. This method allows high molecular weight polymers to be bonded efficiently to the surfaces of CNTs; it also allows higher density of bonding reactions on these surfaces. However, careful control of the amount of initiator, choice of substrate, and polymerization reaction are required. There are a number of approaches to accomplish this type of grafting, including atom-transfer polymerization, ring-opening

polymerization, free-radical polymerization, reduction/oxidation polymerization, and cationic/anionic polymerization [13]. There are also methods that involve functionalization of the ends of CNTs, and the use of monomers and radical initiators into CNT cavities followed by polymerization [15, 16].

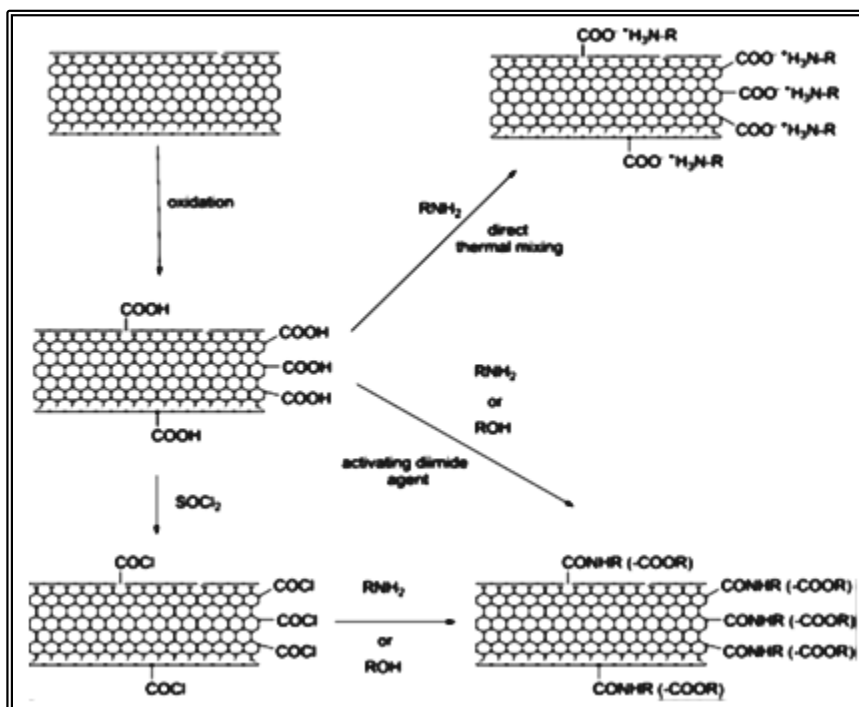


Figure 1.1: Functionalization of CNTs and reaction with amines or alcohols [14].

It has been found that short-fiber composites differ from continuous-fiber composites in that they can be easily molded into complex shapes, but there is a significant reduction in fiber length before processing. This results in aspect ratios of only about 100, which are normally insufficient to make a strong composite. On the other hand, it has been predicted theoretically that this will not be an issue with CNTs, because they can retain aspect ratios of 1000 or more. Even so, it has been noted by some that there are still two main obstacles that limit the use of CNTs as reinforcing material. First, to achieve good load transfer from the polymer matrix to CNTs, the nanotubes must go through a

differential-oxidation treatment to get rid of the catalyst caps and open the ends of the CNTs for bonding with the polymer matrix. Such a treatment causes about 90% weight loss. Second, CNTs tend to form bundles when they are produced because of their high surface area. Accordingly, it has been recommended to use a mixing method that is forceful enough to break up the bundles and create a uniform dispersion of CNTs in the polymer matrix [17, 18].

In this research, these obstacles are being overcome by utilizing a new processing route that involves high-shear mixing in molten PA 66 to induce de-agglomeration and dispersal of CNTs, while enhancing adhesive bonding and covalent bonding by creating new sites on the CNTs to which the polymer chains can bond.

1.2 Post-Fabrication Heat Treatment of GNF-Reinforced Polymer Matrix Composites

Post-fabrication heat treatment of polymers is often used to modify their structure, morphology and properties [19]. Typically, post heat treatment is used to increase chain length and/or degree of crystallinity [20, 21]. For example, when applied to polyethylene, the fully crystallized state consists of thousands of monomers [22].

Post-fabrication heat treatment is found to have a profound effect on the mechanical properties of partially crystalline polymers by increasing the melting point, fractional crystallinity, stiffness, yield stress and brittleness. Accordingly, it decreases the elongation to break, and fracture toughness [23].

These changes in the mechanical properties often come as a result of changes in the morphology, size and distribution of the crystalline phase as the mechanical and thermal

analysis suggest [23, 24]. Scientists divided heat treatment into two types depending on the mechanism of the morphology change:

1. Lamellae thickening by solid state diffusion. This occurs by migration of the chain defects at low temperatures, well below the melting point. In this mechanism thin lamellae melt and re-crystallize as thicker lamellae. This occurs at a temperature below melting but above and close to the crystallization temperature.
2. The second mechanism occurs at temperatures within the melting region. It involves partial melting of the lamellae surface inwards towards the core following the chain axis; hence re-crystallization at the heat treatment temperature produces thicker lamellae which will lead to an increase in the crystallinity.

Both mechanisms have been approved by much evidence based on electron microscope analysis of the result morphologies and SAXS measurements of the lamellae size [25].

It is a well-known fact that when a polymer is kept for a short time in a temperature just above its detectable melting point, its crystal nucleation density increases and its crystallization temperature shifts to higher values. This fact was always supported by the Differential Scanning Calorimetry (DSC) results [26].

The above mechanisms have been supported experimentally using regularly stacked polyethylene single crystals. In this system thickening occurs during heat treatment through a mutual chain rearrangement between the adjacent crystals. These rearrangements ultimately lead to a “quantum” increase, or “doubling” of the lamellar thickness. Also, a model was proposed to explain the quantum increase in the lamellar thickness [27].

Any mutual chain rearrangement, after the doubling process has been completed, will stop because of the fact that the surface chains get entangled and the original lamellar stacking in the crystals is lost. The thickening process of the doubled lamellar crystals requires surface melting or melting and recrystallization [25, 28].

It has been shown that the rate of the lamellar thickening which leads to the quantum increase strongly depends on the heat treatment temperature. The higher the temperatures, the faster the doubling process. Also, it has been found that the kinetics of the doubling process is independent of the molecular weight, according to the low frequency Raman spectroscopy results involving the intermediate stages [27].

Heat treatment of polymers is considered one of the most effective methods of property modification to widen their application. It was shown that heat treatment of polyamide (PA) improved its tribological properties [29].

By studying the deformation mechanisms in semi-crystalline polymers, it was found that the main deformation in the crystalline portions of PE, Nylon, and PET occurs by crystallographic shear on crystallographic chain slip planes.

The weak van der Waals bonding between neighboring covalently bonded molecule chains allows only glide between these chains. According to symmetry considerations, the five independent shear systems requirement for a close packed yield surface has not been satisfied by crystallographic slip in PET for example, because of the low triclinic symmetry of PET crystals. This leads to the violation of the Von Mises compatibility criterion when assuming crystallographic slip as the only mode of plastic deformation [30, 31, 32, 33].

Relying on these facts, the investigation of crystallinity in deformed and heat treated semi-crystalline PET revealed that crystallinity decreases during deformation. This led to the suggestion of amorphization or decrystallization as a deformation mechanism which occurs as an alternative to crystallographic slip depending on the orientation of the nanocrystalline lamellae.

It was also found that heat treatment leads to the enhancement of the original orientation distribution of the crystals before heat treatment by recrystallization of amorphous material. This phenomenon was explained in terms of oriented nucleation where amorphous material crystallizes alongside existing crystalline lamellae [32, 34, 35, 36].

For amorphous glassy polymers like polycarbonate (PC), it has been found that heat treatment just below the glass transition temperature causes a significant drop in the notched Charpy impact strength. While the treatment brought about an increase in the tensile strength. The same embrittlement behavior was noticed by comparing quenched polyethylene terephthalate (PET), in its glassy amorphous state, with the heat treated PET at 51°C for 90 minutes.

It has been suggested that the ductility of glassy amorphous polymers at low temperature is related to the relaxation behavior enabled by a sub-molecular motion at these temperatures. The relaxation process explains the high toughness of PC at temperature as low as -100°C.

It was pointed out that heat treatment results in a reduction in the sub-molecular motion causing the toughness of amorphous glassy polymers to decrease. It was suggested that the heat treatment reduces the size of the local plastic zone at the fracture

tip. This reduction in size leads to the nucleation of internal craze at the tip of the plastic zone transforming the fracture from a ductile to a brittle one [37].

From the above, it was shown the importance of heat treatment as a way to enhance the strength and performance of polymers and polymeric matrices in their composites. In this work, the influence of heat treatment on the performance of GNF-polymer based composites will be also revealed.

According to the tribological facts, when two components slide against each other, the amount of heat generated from frictional motion will depend mainly on friction coefficient (μ), sliding speed and pressure. The frictional heat is responsible for decreasing the tribo-performance by changing friction and wear mechanisms. This heat is dissipated to the environment by conduction, convection and radiation. Accordingly, the heat transfer will depend on the temperature difference between the tribo-couple and the ambience. In this case, various thermo-physical properties of both the surfaces such as specific heat, thermal conductivity, diffusivity etc. will affect the heat flow. Normally, higher thermal conductivity and thermal diffusivity will enhance the heat flow from the friction surfaces which leads to minimizing the damage to these surfaces, as in the case of metal sliding against metal. However, when a polymer slides against metal or another polymer, the excessive accumulation of heat on the surface will result in loss in strength, thermal degradation and melting of the polymeric surface since thermal stability and thermal conductivity of polymers are very low [38].

The problem of low thermal conductivity can be solved to some extent by incorporating appropriate fillers having higher thermal conductivity. Knowing that graphite has a thermal conductivity up to 2000W/m.K parallel to plane and up to 800

W/m.K perpendicular to plane [39], these values make graphite among the best candidates as filler material. On the other hand, it is also known that graphite is a remarkable solid lubricant [40].

Aside from its role in improving the strength and performance of the polymeric matrix, it was noticed in this work, that heat treatment of polymer based composites containing GNFs as reinforcing material can significantly reduce the amount of the polymeric portion on the composite surfaces. This can be accomplished by thermally etching these surfaces exposing the GNFs, which leads to enhancing the tribological properties of the frictional component made of that composite.

Thermal etching process of the polymeric matrix in GNF-polymer composites does not stop at enhancing the tribological properties of the frictional components. In fact, by controlling soaking time at the heat treatment temperature, it is possible to achieve the desired graphite content profile across the composite product.

Knowing the above, heat treatment of GNF-polymer composites can be divided into two categories depending on the desired final product:

1. Keeping the composite at the heat treatment temperature for short times will yield enhancement of the tensile strength by promoting crystallization of the polymeric portion, in which graphene sheets can act as recrystallization sites.
2. Heat treating the composite for longer times will have the same effect but also it will thermally etch the polymer on the surface for few micrometers depth, which will lead to enhancing the tribological properties of the frictional components made of that composite.

In this work, both heat treatments have been investigated to find the best treatment temperatures for the composites involved. Also, the desired results were achieved with maintaining minimum thermal distortion.

Chapter 2

Overview and Literature Survey

2.1 Processing and Characteristics of MWCNT-Reinforced PA 66 Composites

2.1.1 Overview

For optimal mechanical properties of a multi-wall carbon nanotube MWCNT-reinforced polymer matrix composite, the MWCNT/polymer bond strength should be high enough to ensure good load transfer between the exceptionally strong and stiff MWCNTs and the much weaker but tougher polymer matrix. The distribution of MWCNTs within the polymer matrix should also be uniform and free of MWCNT agglomeration.

In this thesis, both challenges are addressed by utilizing a high-shear mixer of novel design that has the ability to break MWCNTs exposing dangling bonds. At the same time, to efficiently and uniformly disperse loosely-agglomerated MWCNTs in molten PA 66. After melt processing, the resulting MWCNT-PA 66 composite displays a significant increase in flexural modulus and impact resistance, which are attributed to effective load transfer between the CNTs and PA 66 matrix. Two mechanisms are believed to contribute to the improved mechanical performance of the MWCNT-PA 66 composite:

- 1) Adhesive bonding between CNT surfaces and polymer matrix, and
- 2) Covalent bonding is believed to occur between fractured ends of MWCNTs and polymer matrix.

The creation of many dangling orbitals at pristine fractured edges of multi-wall CNTs, to which the molten polymer can covalently bond, is believed to be primarily responsible for composite strengthening. Another effect is the degree of texturing or alignment of

MWCNTs developed in the processed MWCNT-PA 66 composite, which introduces a high degree of mechanical anisotropy into the composite.

As will be shown, nanoscale crystallization of the PA 66 matrix occurs at fractured ends of CNTs, which effect increases the thermal stability of the PA 66 matrix.

Potential structural applications for MWCNT-reinforced polymers include sporting goods, transportation vehicles, and aerospace systems. There are also applications that exploit the unique chemical, electrical and thermal properties of MWCNTs, but these are not considered here. Nor for that matter are in field emitters, metrology, biological systems, and as starting materials to form other nanostructures.

2.1.2 Literature Survey

In what follows, a concise review of relevant literature on the known structures of single- and multi-walled carbon nanotubes (CNTs) and methods developed for their production are presented. Methods used to fabricate CNT-reinforced polymer matrix composites (CNT-PMCs) are also discussed, highlighting the uniqueness of the present processing methodology. As will be shown, this process uniformly disperses loosely-agglomerated multi-wall CNTs in molten PA 66, such that measured mechanical properties are reproducible from one sample to the next.

2.1.2.1 Structure and Properties of Carbon Nanotubes

Carbon nanotubes (CNTs) were first observed in 1952 [41]. Later, in 1976, single- and double-walled carbon nanotubes were reported [42]. In 1991, Iijima described the synthesis of multi-walled CNTs using an arc-evaporation process [43]. Although he has been credited with the discovery of CNTs at that time, a small company in the US was already producing CNTs, called “carbon fibrils”, utilizing a chemical vapor growth

process. In 1993, a new process to grow single-walled carbon nanotubes (SWCNTs) was described by two independent research groups [44, 45].

A CNT consists of a sheet of hexagonal-bonded carbon atoms rolled up to form a tube [43]. A single-walled carbon nanotube (SWCNT) comprises a single layer of this tubular structure of carbon atoms, Figure 2.1. However, the structure of a multi-walled carbon nanotube (MWCNT) is still open to debate. In one model, a MWCNT is imagined to be a single graphene sheet rolled up into a scroll [46]. In another model, a MWCNT is considered to be made of co-axial layers of helically-aligned carbon hexagons, with matching at the joint lines, leading to a nested-shell structure [47]. In yet another model, a combination of scroll-like and nested-shell structures was proposed [48].

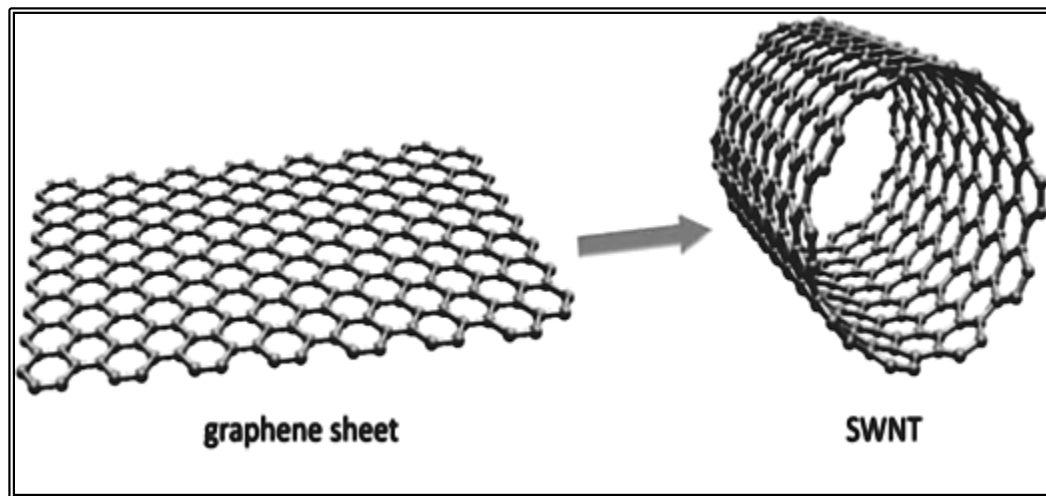


Figure 2.1: Wrapping a graphene sheet to form a SWNT [6].

As indicated in Figure 2.1, a single sheet of graphite (called graphene) comprises a planar honeycomb-like lattice of carbon atoms, in which each carbon atom is strongly bonded to three adjacent carbon atoms. Accordingly, the elastic modulus of the basal-plane of graphite is one of the highest of any known material. Similarly, SWCNTs are expected to be exceptionally strong fibers, although there remains some disagreement

concerning the exact value of its stiffness and strength. Using an atomic force microscope (AFM), the force required to pull a free-standing nanotube out of its equilibrium position has been measured. The most recent value of Young's modulus of SWNTs is about 1 TPa, but other values have been reported. These differences may be a consequence of differences in measuring techniques [49].

Theoretically, it has been shown that the Young's modulus of a SWCNT depends on its size and structural symmetry. On the other hand, a MWCNT displays quite a different behavior. It has been observed that the modulus of MWCNTs, determined by AFM techniques, does not strongly depend on diameter. Instead, it depends on the extent and type of disorder in the nanotube walls. It is not surprising, therefore, that when a MWNT breaks, the outermost layers break first [50]. The present research will demonstrate that fractured ends of MWCNTs are favorable sites for covalent bonding to the polymer matrix.

Table 2.1: Mechanical properties of CNTs and some common materials [51]

Material	Young's modulus (GPa)	Tensile strength (GPa)	Density (g/cm³)
SWCNT	1054	150	
MWCNT	1200	150	2.6
Steel	208	0.4	7.8
Epoxy	3.5	0.005	1.25
Wood	16	0.008	0.6

2.1.2.2 Carbon Nanotubes CNTs Synthesis

Well-developed methods for synthesizing CNTs include arc discharge [52], laser ablation [53], and chemical vapor deposition [54]. Also, there is a rarely used method of arc-discharge in a liquid solution. In addition, vertically aligned CNTs are synthesized using lithographic methods and selective growth of CNTs using nanoporous anodized aluminum oxide as substrate [55].

Initially, high temperature synthesis methods, such as arc discharge or laser ablation were used to prepare CNTs. Currently, these techniques are being displaced by lower temperature chemical vapor deposition (CVD) methods ($<800^{\circ}\text{C}$). The newer methods enable more effective control over the purity, density, alignment, orientation, nanotube length and diameter [56]. Most of these processes utilize transition-metal based catalyst particles to enable controlled growth of SWCNTs and MWCNTs. In practice, particle at-the-tip growth of CNTs appears to be the dominant growth mechanism, although particle-at-the base growth is also observed. These two mechanisms are illustrated in Figure 2.2 [57].

Several industrial-scale processes for the production of high quality CNTs have been developed. For example, C-Nano has commercialized a fluid-bed CVD process that produces tonnage quantities of loosely-agglomerated CNTs. The process utilizes an inert bed of micron-sized ceramic particles as the fluid medium, and flowing nitrogen as the fluidizing gas. When the bed attains a pre-determined temperature, a transition metal precursor is introduced and nano-sized catalyst particles are deposited on the inert ceramic particles. The catalyst particles then serve to grow CNTs when a carbon source gas, such as methane, is introduced into the fluid bed. The as-produced CNT

agglomerates are periodically removed from the bed and the operation continued. In this research, C-Nano MWCNT agglomerates are used exclusively as additive to the molten PA 66 during high-shear mixing in order to generate MWCNT-PA 66 test specimens for evaluation of mechanical properties, particularly flexural strength and impact resistance.

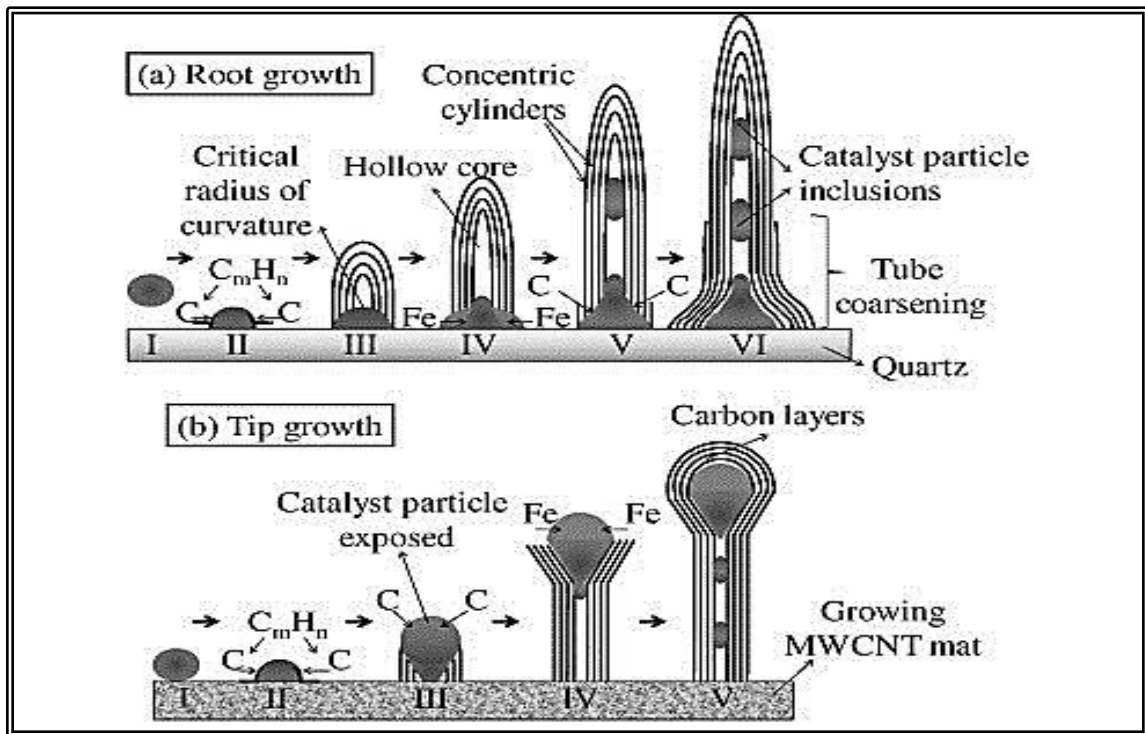


Figure 2.2: Root and tip growth mechanisms of MWCNTs [56].

2.1.2.3 Processing of CNT-reinforced Polymer Composites

Since their discovery in the early 1990s, researchers have investigated CNTs as additives to polymers to enhance thermal, electrical and mechanical properties. First attempts were made to produce polymer-matrix composites that display one or more CNT properties. Some of these trials were successful. For instance, it has been shown that a 1 wt. % CNT addition to epoxy increases the conductivity to 2 S/m [58]. Additions of CNTs to thermoplastic polymers have also been used to increase thermal conductivity [59].

In this research, one of the objectives is to document changes in mechanical properties of MWCNT-reinforced PA 66 composites due to varying weight fractions of MWCNTs and study the mechanisms involved. Many attempts have already been made to enhance the strength of polymers by CNT additions, but these efforts have fallen short of expectations. This shortcoming has led researchers to start thinking about load transfer mechanisms, and particularly the likely controlling effect of CNT/polymer interfaces [60, 61].

In an effort to attain better dispersion, interface optimization and composite properties, researchers have attempted to randomly disperse CNTs in a molten polymer using conventional mixing methods (like sonication or mechanical stirring). However, a great deal of CNT agglomeration is invariably observed in the final composite, significantly reducing the strength outcome [62]. Other researchers attempted to improve dispersion and interfacial bonding between CNTs and polymer matrices by using surfactants, chemical functionalization, and/or oxidation of surfaces of CNTs. Although these attempts increased dispersion and interfacial reactivity of the CNTs, it has been found they compromised bonding of graphitic surfaces of the CNTs, leading to properties degradation in the final composites [63].

The primary issues with processing CNT-PMC composites are still that CNTs tend to agglomerate, are difficult to align within the matrix, and suffer poor surface-matrix adhesion and load transfer. Thus, there have been a number of reported attempts to produce CNT-PMCs using different polymer matrices [64, 65, 66, 67].

A recent research has shown increases in elastic modulus and strength via small additions of CNTs to various polymer matrices [68]. While Van der Waals bonding

dominates interactions between CNTs and polymers, adhesion in some composites also occurs via covalent bonds, which has been shown to play a role in reinforcement of CNT/polymer composites [69].

Measurements by AFM of the pull-out force necessary to remove a given length of an individual MWCNT embedded in a polyethylene–butene copolymer has demonstrated covalent bonding between the outer layer of a MWCNT and the polymer matrix, Figure 2.3. It also showed that the polymer matrix in the near vicinity to the interface behaved differently than the polymer in the bulk, which was attributed to the outer diameter of a CNT having the same magnitude as the radius of gyration of the polymer chain [70].

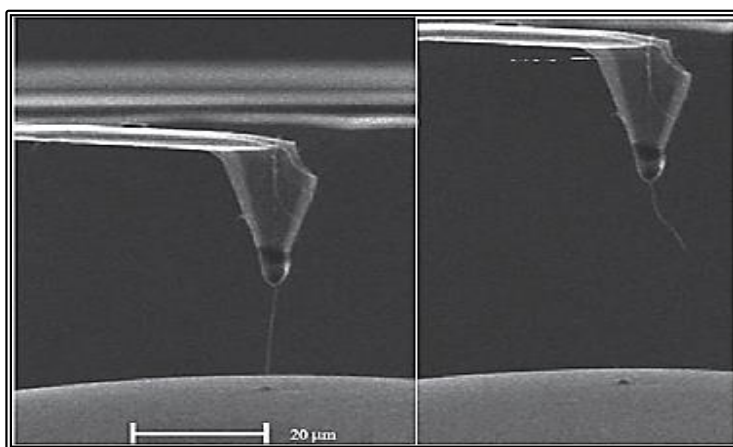


Figure 2.3: Left; shows one end of a single MWCNT is attached to the AFM tip and the other is embedded in the solid polymer matrix. Right; shows the process of pull-out of MWCNT. The critical force needed for pull-out was recorded by AFM [70].

One of the recent successful attempts to produce a relatively high performance MWCNT-PA6 matrix composite was made in 2004. Samples with different loadings of MWCNTs in PA6 were made by a conventional melt-mixing method. A uniform dispersion of the MWCNTs was accomplished throughout the PA6 matrix. Observation of the fracture surface by scanning electron microscopy revealed good dispersion and

interfacial adhesion of MWCNTs in the PA6 matrix. A reduction in the overall length of MWCNTs and absence of segregation in PA6 was also observed.

In that research, a beadlike morphology seen on the MWCNTs and along their bundles indicates the presence of sites for bonding, where load transfer from CNTs and polymer could occur. It was shown by tensile testing, nano-indentation testing, and dynamic mechanical analysis that the elastic modulus and yield strength were improved in the composite, compared with PA6. The increase in mechanical properties went hand in hand with increasing weight percent of the reinforcing MWCNTs. For instance, upon incorporation of only 2 wt % MWCNTs, the elastic modulus of PA6 is greatly improved by about 214% from 396 to 1242 MPa, and the yield strength is improved by about 162% from 18 to 47 MPa. In addition, locations of new crystallization and melting behavior were found in the MWCNT-PA6 composites. Using combined DSC and X-ray diffraction analysis, it was observed that these new crystallization areas appear only in MWCNTs-PA6 composites, which is very different from other reinforcing materials for example clay-PA6 nanocomposites. Still in the processing stage, MWCNTs were subjected to chemical treatments to dissolve the catalyst particles using hydrochloride acid, and to add carboxylic and hydroxyl groups using diluted nitric acid [65].

In another work, functionalization with amine groups was performed on MWCNTs using a ‘grafting’ method. This technique requires oxidizing MWCNT into (MWCNT–COOH), which in turn is reacted with thionyl chloride (SOCl_2) to functionalize the MWCNT with acyl chloride to produce (MWCNT–COCl). Reaction with hexamethylene-diamine is the final step to achieve MWCNT– NH_2 . Using traditional melt compounding, different additions of MWCNT– NH_2 in PA6 were used to prepare the

composites. In this research also, good MWCNT dispersion and interfacial bonding with PA6 matrix was observed, leading to better mechanical properties compared with the original polymer. For example, upon incorporation of 2 wt% of MWNTs, the tensile modulus of nylon 6 went up from 1899 to 3556 MPa and the yield strength was enhanced from 35.0 to 59.3 MPa indicating 87 and 69% improvements, respectively [71].

A more complicated chemical treatment was reported in 2007. In this work, 2.4 M nitric acid was used to soak the MWCNTs for 0.5 hour, and then the CNTs were rinsed with methanol. The resulting MWCNTs were collected using a centrifuge and then dried using a vacuum oven. A solution-crystallization method was used to enhance interfacial bonding between MWCNTs and PA66. Glycerin at 240°C was used as a solvent to dissolve PA66, and then the MWCNTs were dispersed in glycerin at 40°C by ultrasonication. The resulting MWCNT/glycerin mixture was added to the PA66/glycerin solution at 240°C and then quenched to a temperature just below T_c . After controlled crystallization over a time period 0.5–3 hours, the non-crystallized polymer was removed by isothermally filtering the mixture. To obtain the MWCNT/PA66 composites, extra amount of PA66/glycerol solution was added to the mixture at T_c and kept for 3 hours for further crystallization. Upon cooling to room temperature, the system was filtered to remove the glycerol. In the final step, grayish solid samples were collected and washed thoroughly with isopropanol and kept in a vacuum oven overnight [72].

It can be noticed from this previous research and many others, chemical treatments of CNTs to functionalize their surfaces are required to achieve good interfacial bonding, leading to better mechanical properties. However, in one project, it was reported that mechanical drawing and stretching was effective in mitigating segregation and waviness

of CNTs in the polymer matrix. This approach requires drawing arrays of CNTs onto a rotating cylindrical spool of polytetrafluoroethylene (PTFE). While tension is applied, CNT ribbons are infiltrated with PA 66 solution using a dropper. In the next step, a tensile testing machine is used to stretch the CNT-PA66 composite ribbons while at the same time a local heating device is moved slowly along the CNT-PA66 composite to accomplish uniform heating to eliminate the solvent [73].

Other than chemical and mechanical/thermal treatment of the CNTs or the composite itself, another approach utilized in situ polymerization of PA6 containing MWCNTs. In this work, a homogenous dispersion of MWCNTs in ϵ -caprolactam mixture was achieved by sonication at 120°C for 1 hour. After that, a small amount of 6-amino hexanoic acid was added to the suspension. A preheated oil bath (270°C) was used to heat the mixture flask for 6 hours under mechanical stirring in a nitrogen atmosphere. A good dispersion of the MWCNTs in the PA6 matrix was achieved using this process. For better interfacial bonding between the CNTs and the PA6 matrix, chemical treatment of the MWCNTs was required before polymerization [74].

It has been demonstrated by many researchers that the use of MWCNTs as reinforcing materials in polymer matrices is better than SWCNTs for two reasons. First, in their opinion, SWCNTs tend to pull out from their bundles under stress, which eventually suppresses good stress transfer from the matrix to the CNTs. This means that the mechanical properties of the final composite depend on the behavior of CNT bundles rather than on a single CNT [75, 76, 77, 78]. Second, pyrolytically carbon-grown MWCNTs usually contain defects and kinks in their outer layers, which tend to bond

efficiently to the polymer matrix. This effect significantly improves dispersion and increase the amount of load transferred from the polymeric matrix to CNTs [76].

Other than the tendency to use MWCNTs rather than SWNTs for reinforcement of polymers, the widespread usage of PA 66 as matrix material is noteworthy. This is because CNTs have better interfacial bonding and dispersion behavior in PA 66 than other polymers. In addition, the relatively low melting temperature of PA 66 makes it easier to manipulate the processing, also to make the composite more easily scalable.

2.2 Post-Fabrication Heat Treatment of Graphene-Reinforced Polymer Matrix Composites

One of the best known heat treatments of polymers is that performed on polyacrylonitrile (PAN) thermoplastic during the synthesis of carbon fibers. In this process, drawn PAN fibers are stretched and oxidized simultaneously in a temperature range of 200–300°C. In this step, the polymeric composition of PAN is altered to a non-plastic ladder or cyclic structure. Later, the oxidized fibers are carbonized at 1000°C in an inert atmosphere of nitrogen gas. Then the fibers are reheated at about 1500–3000°C to reduce the polymer content by 92–100%. As a result of this treatment, crystallite ordering and orientation in the direction if the fibers axes are enhanced. Heat treatment at high temperature is necessary to drive out the impurities as volatile by-products.

This process results in shrinkage of fiber diameter and the build of a new inorganic structure from the original polymeric one. Also, the strength is improved by removing the initial nitrogen content of PAN. The elastic modulus of the fiber can attain 400 GPa with carefully controlled processing conditions. Generally, the processing procedure is the same for all reported productions of carbon fibers from PAN, although temperatures and

timings differ and vacuum is sometimes used instead of a nitrogen atmosphere [79, 80, 81, 82, 83].

Other than using heat treatment to convert PAN into carbon fibers, in one work, the researcher reported heat treating polyethylene at a temperature higher than the crystallization temperature but below the melting temperature. At this temperature crystals tend to grow in size at the expense of the surrounding amorphous polymer, which causes the overall structure of the polymer to have a “Swiss Cheese” like appearance [84].

Heat treatment of polyethylene in order to improve crystallinity, mechanical and physical properties has been explored since the late sixties. Yet, most of the work focused on heat treating the thermoplastic without reinforcement, at temperatures below its crystallization temperature, mainly to increase the size of the crystals and/or the crystalline domains [85, 86, 87, 88].

In another work, the effect of annealing on the plane-strain fracture behavior of round-notched polycarbonate (PC) and polymethyl methacrylate (PMMA) bars was investigated. It was found that crazes nucleated on the tips of the local plastic zones. Annealing did not have much of an effect on the hydrostatic stresses required for internal craze nucleation, but the shear yield stress increased with increasing annealing time. However, the regression of the plastic zone by annealing caused reduction in toughness [89].

Another research indicates that by using a specific heat treatment of a blend of polyvinyl chloride with a co-polyester thermoplastic elastomer, the blend can undergo phase separation that leads to a significant increase in room-temperature impact strength.

By studying the dynamic mechanical properties, impact strength and the microscopic structure of the blend, a dependence on the thermal history of the specimen was found. Also, it was noted that both crazing and shear flow processes were involved in the mechanism of energy dissipation [90].

In the last few decades, there have been many successful attempts to improve the mechanical, thermal or physical properties of different types of polymers or polymer blends by heat treatment. These attempts involved heating the specimens to a wide range of temperatures that depended on the intended property boost [91, 92, 93]. Yet, these works did not address the consequences of heat treating a polymer-based composite.

In a 1992 work, heat treatments were carried out on two commercial and four experimental composites for dental applications. In this research, the composites were subjected to 10 minute and 3 hour treatments at 120°C. After 24 hours from heat treatment, fracture toughness, flexural modulus, micro-hardness and degree of response to the treatment (using FTIR) were determined. Significant improvements in degree of cure and mechanical properties of these dental composites occurred as a result of post-cure heat treatments at 120°C for both short and long times. Furthermore, it was shown that even after 7 days of the initial light-curing, the 3-hour heat treatment was capable of improving properties as much as the immediate heat treatment. A toughening of the filled resin matrix was indicated by the increase in properties and the results of fractography. The increase in toughness was ascribed to a possible improvement in the filler/matrix adhesion of the micro-fills [94, 95].

In another project, heat treatment of single polymer-carbon fiber composites and binary polymeric blend-carbon fiber composites were investigated. Mechanical and

thermal properties of 30 wt.% short-carbon fibers with epoxy (EP), unsaturated polyester (UPE), 80 % EP - 20 % polysulphide rubber (PSR) and 40% EP - 60 % UPE were evaluated before and after heat treatment at different temperatures. Mechanical mixing was used to make the binary blends as well as to incorporate carbon fibers within the polymeric matrices. After heat treating all the samples at 50°C, 75°C, 110°C and 220°C for 3 hours, it was found that ultimate tensile strength and hardness of all the samples were increased, such behavior was attributed to the convergence of polymeric molecules due to heat treatment [96].

In a very recent study, samples of epoxy with different MWCNT loadings were subjected to heat treatment after solidification. The composite was made by ultrasonication of the epoxy and MWCNTs mixture followed by mechanical stirring. After curing at room temperature for 24 hours the samples were heat treated at 50°C, 100°C and 150°C for 1 hour. To track changes in the mechanical properties of the composites before and after heat treatment, hardness and wear tests were conducted. It was shown that at a certain MWCNT addition (0.25 wt.% MWCNT) in epoxy, the composite after heat treatment at 100°C had the highest hardness and wear resistance [97]. The same experiment was performed using graphene instead of MWCNTs. In this case, an addition of 1 wt.% graphene in epoxy had the highest flexural strength and hardness when heat treated at 100°C for 1 hour [98].

Aside from being used to improve mechanical properties of graphene-polymer composites, heat treatment can also be used to control electrical properties of the composites. Heat treatment of a graphene-polyethylene composite for varying time at 180°C made the positive temperature coefficient of resistivity tunable. It was thought that

the treatment randomizes the graphene network and raises the resistivity, which leads to increasing the coefficient. According to this research, heat treatment also increased the crystallinity of the polymer matrix, which in turn caused local flow that allowed the graphene plates to move, weakening the conductive paths and increasing the positive temperature coefficient of resistivity [99].

Chapter 3

Experimental Procedure

In what follows, the experimental setup used to prepare samples of MWCNT-reinforced PA 66 for mechanical properties measurements is described. In addition, the procedure and influence of a post-fabrication heat treatment on structure and properties of GNF-reinforced PEEK and GNF-reinforced PA 66 is discussed.

3.1 Processing of MWCNT-Reinforced PA 66 Composites

3.1.1 Starting Materials and Characteristics

3.1.1.1 Multi-Wall Carbon Nanotubes

Multi-wall carbon nanotube (MWCNT) powder is obtained from CNano Technology. A sequence of back-scattered field emission scanning electron microscope FESEM micrographs, Figure 3.1, shows that a typical particle (10-50 μm) consists of loosely-agglomerated multi-wall CNTs 30-40 nm in diameter and $>50 \mu\text{m}$ in length, i.e. they have high aspect ratios (>1000). In several cases, the MWCNTs have white-contrasting tips, which are transition-metal catalyst particles. Hence, it is apparent that the MWCNTs are produced by the familiar particle-at-the-tip growth mechanism [100]. Figure 3.2 shows an X-ray diffraction pattern (XRD) of the MWCNT powder. It can be noticed that the MWCNTs are of a single dominant carbon structure (main peak at $2\theta = 26^\circ$).

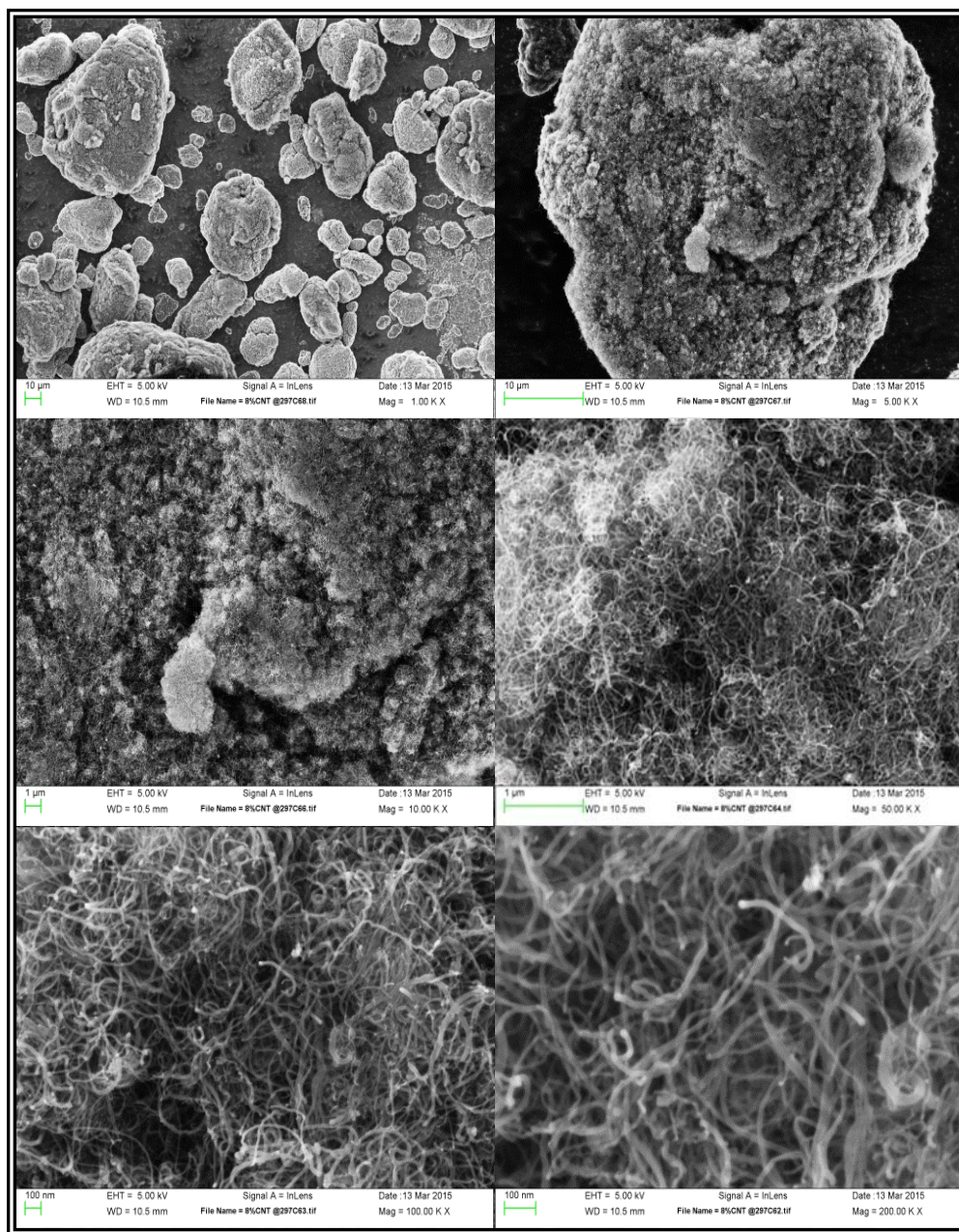


Figure 3.1: A series of SEM images arranged from low to high magnification showing that a typical as-produced particle consists of loosely-agglomerated multi-wall CNTs (MWCNTs).

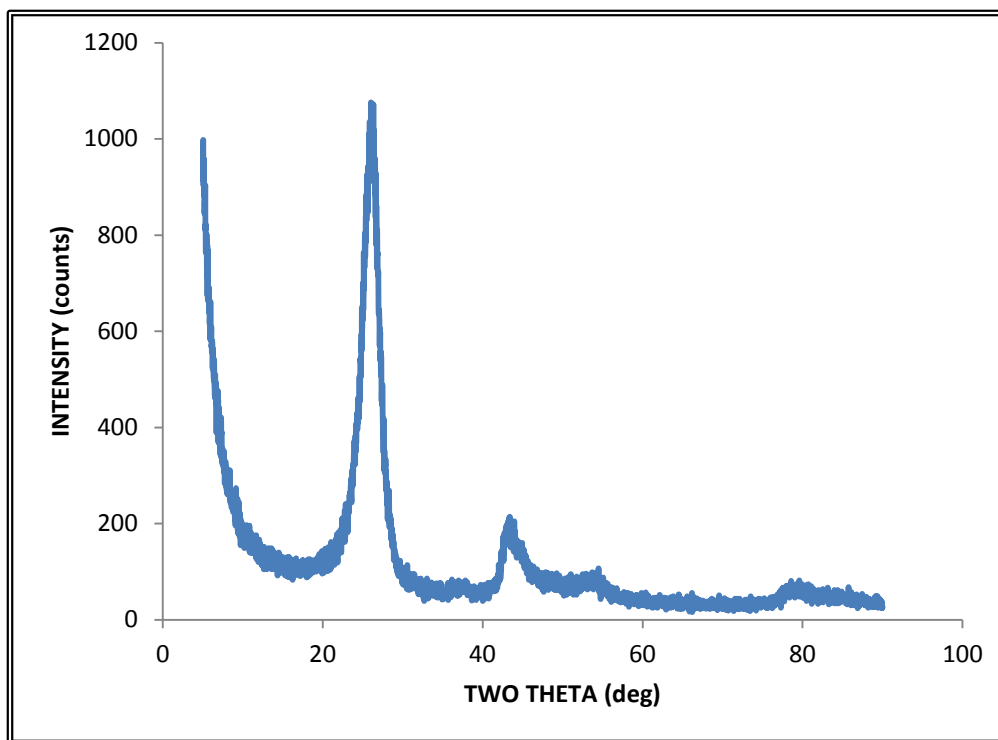


Figure 3.2: XRD spectra of MWCNT powder showing that single crystallization form is dominant throughout the powder.

3.1.1.2 Poly Amide 66 (PA 66)

Pelletized PA 66 (Nylon), with particle size in the 1-5 mm range, is acquired from DuPont Inc. Figure 3.3 shows differential scanning calorimetry DSC heating-cooling-heating curves over the range 20-280°C at 10°C/min for both heating and cooling rates. The melting and crystallization temperatures are 261.5°C and 225.2°C, respectively, glass transition temperature is about 60 °C.

The rheology behavior of PA 66 at the selected processing temperature is determined using a TA-AR2000 rheometer operating in the parallel-plate mode. First, to locate the linear viscosity region (LVR) of PA 66, a stress-sweep test is performed at 277°C (16°C above its melting point) using a frequency of 1 Hz and 10 points per decade (log mode). Figure 3.4 shows that the LVR region occurs on 0.1-1.0 % strain range. Second, a

frequency-sweep test is performed from 0.01-100 Hz at 277°C at a strain of 0.4 % to ensure testing occurs within the LVR. Figure 3.5 shows curves for G' (Pa), G'' (Pa) and Delta (degree) as a function of angular frequency (rad/s). These data show that processing PA 66 at 277°C provides the appropriate viscosity range at the shear rate induced in the batch mixer, and accounts for the increase in viscosity that occurs during mixing with the MWCNTs.

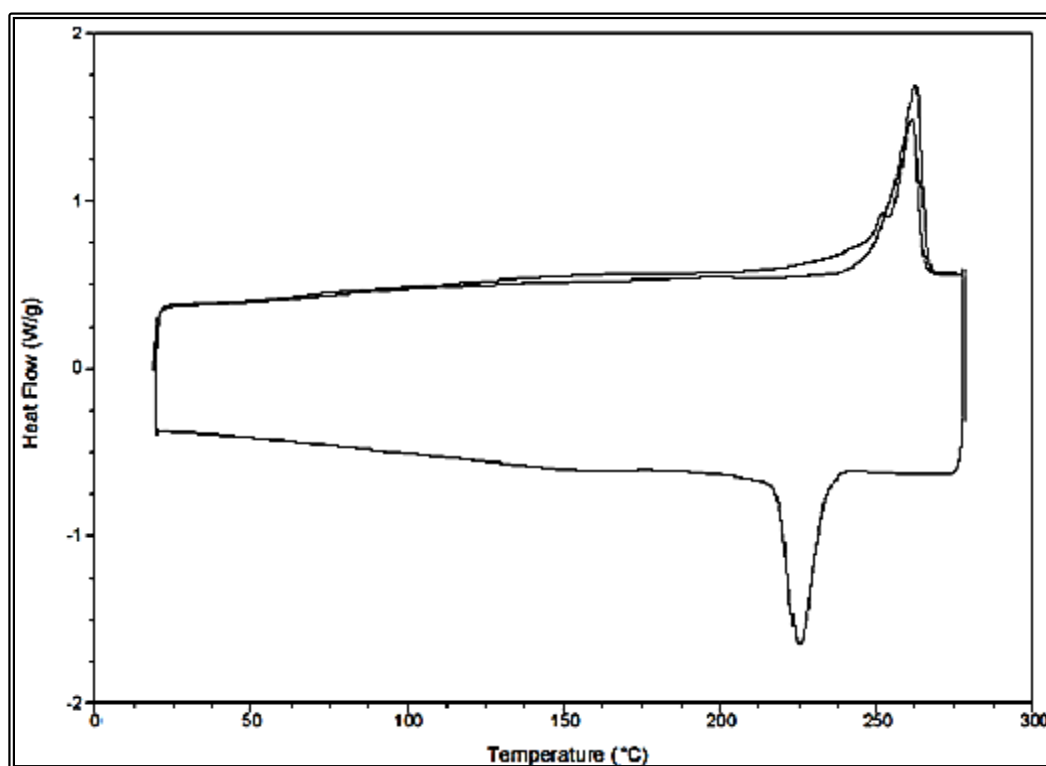


Figure 3.3: DSC curves for PA 66 showing that melting and crystallization temperatures are 261.5°C and 225.2°C, respectively.

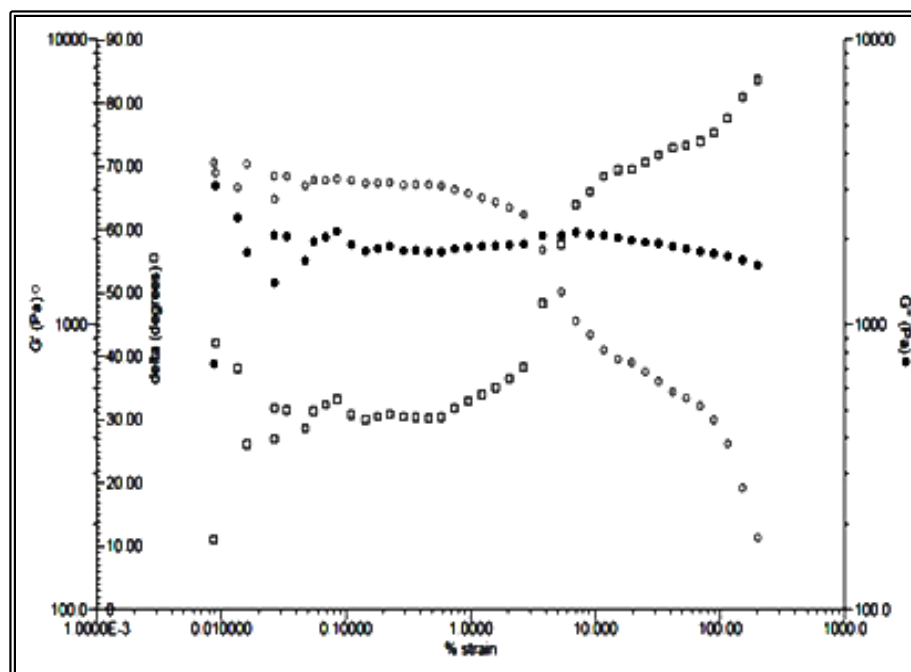


Figure 3.4: A plot of G' (Pa), G'' (Pa) and δ (degrees) vs. % strain in a stress sweep.

The linear viscosity region occurs between 0.1-1 % strain.

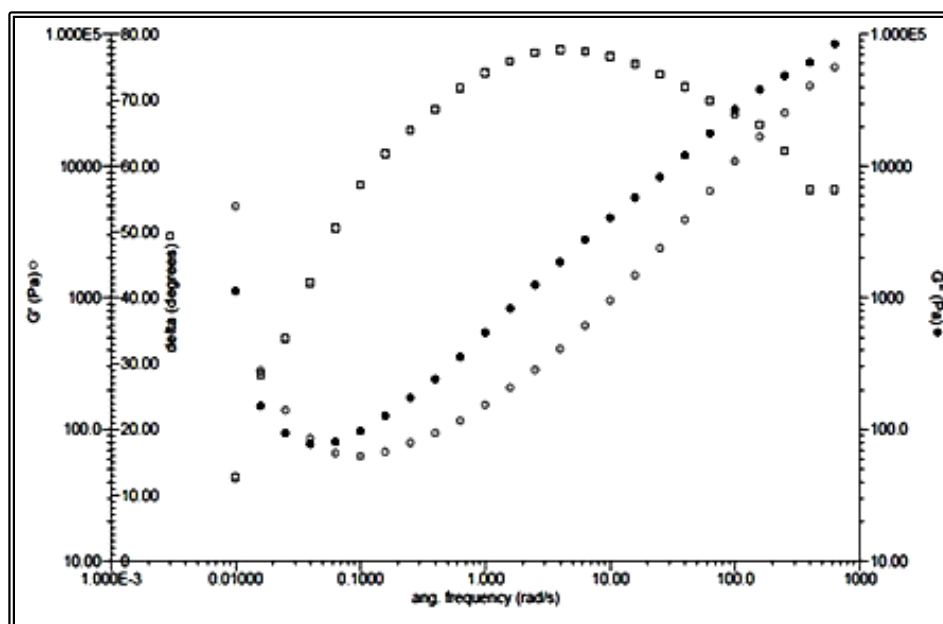


Figure 3.5: A plot of G' (Pa), G'' (Pa) and δ (degrees) vs. angular frequency (rad/s)

in a frequency sweep at 0.4% strain.

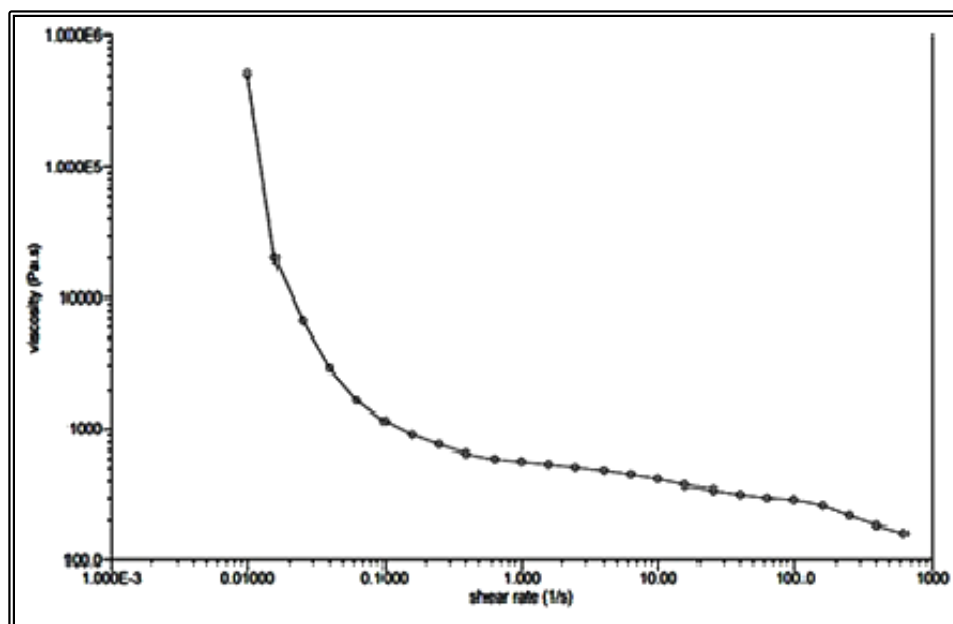


Figure 3.6: Viscosity (Pa.s) vs. shear rate (1/s) of PA 66.

3.1.2 Batch Mixer

A single-screw batch mixer, Figure 3.7, is used to prepare MWCNT-PA 66 composites. The mixing chamber is made of high speed steel and divided into two independently heated front and back barrels. To achieve the desired mixing, a specially designed screw made of hardened steel is incorporated in the mixing chamber. Two types of helically-aligned grooves of different spacing form channels on the cylindrical rotor. The polymer pellets and reinforcing MWCNTs are fed into the mixing chamber through a tube located on top of the front barrel.

A high power electrical motor is used to rotate a close-fitting screw in its barrel to achieve efficient mixing. Mixing speed and temperature are digitally controlled on a control panel, as well as the amperes required to maintain steady rotation whatever the viscosity of the fluid mixture.

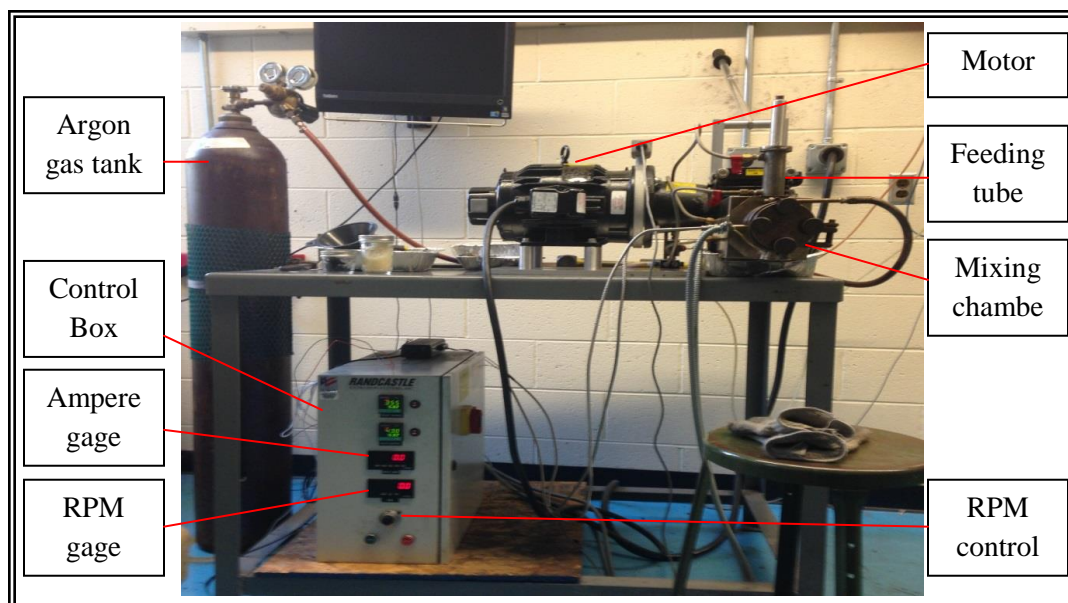


Figure 3.7: Laboratory-scale batch mixer used to prepare MWCNT-PA 66 composites.

To maintain an inert atmosphere inside the mixing chamber, a constant flow of argon gas of industrial grade is introduced through the powder feed tube. The presence of argon gas in the mixing chamber mitigates degradation of the polymer by interaction with impurities, such as water vapor and/or oxygen from the surroundings [101]. Filtered water is used to cool the powder-feed tube and the gear box that sustains the rotation of the screw in the barrel. Maintaining a low temperature in the feed region is necessary to prevent melting of the polymer before it reaches the mixing barrel. Depending on the specific volumes of the composite components, about 100-120 grams of powder is introduced into the mixing chamber in each experiment. Using a screw/barrel gap distance of about 0.85 cm, efficient mixing of the two components occurs via the high shear stresses developed by rotation of the screw inside its barrel.

3.1.3 Mixing Procedure

Loosely agglomerated MWCNT powder is cold pressed in a Carver press using a pressure of 4.5 metric tons and holding time of 5 minutes. After pressing, the disc-shaped compact is broken up into small pieces and vacuum dried at 90°C for 24 hours, along with PA 66, to overcome difficulties of feeding loose and highly volatile MWCNT powder into the mixing chamber. Also, vacuum drying of PA 66 is used to eliminate any absorbed moisture. Following degassing, the now much denser MWCNT powder is introduced into the batch mixer and dispersed in the PA 66 melt.

When the front and back sections of the mixing barrel reach 16°C above the 261°C melting temperature of PA 66:

- 1) Rotor speed is raised gradually up to 50 rpm in 5 minutes, and held at this speed for an additional 10 minutes;
- 2) 30g of PA 66 pellets is gradually fed into the chamber and melted;
- 3) Small pieces of cold-pressed MWCNT powder and PA 66 pellets are added periodically to the molten polymer to ensure good mixing and to stabilize the viscosity of the composite melt;
- 4) After feeding the desired amounts of MWCNT powder and PA 66 into the mixer, the mixing speed is raised slowly to 200 rpm, where it is held for 20 minutes to complete the process.
- 5) The rotor speed is gradually reduced until its motion is stopped, and then the composite is extracted at the mixing temperature.

Incremental additions of MWCNTs to the molten PA 66 are necessary to produce composites that contain high fractions of MWCNTs. Feeding process takes about 20

minutes to ensure that mixing parameters remain as stable as possible. After completion of extraction and upon cooling to ambient temperature, the material becomes hard and brittle. This is further evidence for chemical bonding between dispersed MWCNTs and PA 66 matrix.

3.2 Procedure of Heat Treatment of GNF-Polymer Composites

The effects of post-fabrication heat treatments on structures and properties of 35 wt. % GNF-PEEK and 35 wt. % GNF-PA 66 composites have been investigated. The composite samples were made in a specially designed exfoliation/injection molding machine that has the ability to in-situ exfoliate 300Mm graphite sheets in molten polymers and reduce the reinforcing material to few-layers or even a single-layer graphene. To minimize sample distortion, each composite requires a specific heat treatment procedure. Although, an optimal heat-treatment procedure has not yet been established for each composite, enough progress has been made to enable major structural and properties changes to be documented. A feature of both heat treatments is at least one extended annealing at a temperature just above the melting point of the polymer matrix phase, where reaction occurs between GNFs and polymer matrix.

3.2.1 35 wt. % GNF-PEEK Composite

Heat treatment of 35wt. % GNF-PEEK samples was performed in a resistively-heated furnace, with each sample placed vertically in the furnace. The first experiments involved heating composite specimens at a rate of 5°C/min to 200°C, 400°C, and 600°C, and held at each temperature for 20 minutes. The samples heated at 400°C and 600°C for 20 minutes experienced extensive decomposition of the PEEK matrix phase, leaving behind porous graphitic material. In addition, the specimens suffered from swelling, due to the

accumulation of PEEK-decomposition gases within the samples. Most of the swelling occurred in the upper half of the specimen, as would be expected from buoyancy effects.

After several experiments, a two-step heat treatment was found that did not degrade the PEEK matrix with weight loss of 1-2 wt. %. It involved first heating the composite at a rate of 5°C/minute to 200°C for 20 hours, and then to 380°C for 18 hours using the same heating rate. The resulting specimens retained their original shape, even though major structural modifications within the composite must have occurred to account for the observed changes in resulting samples.

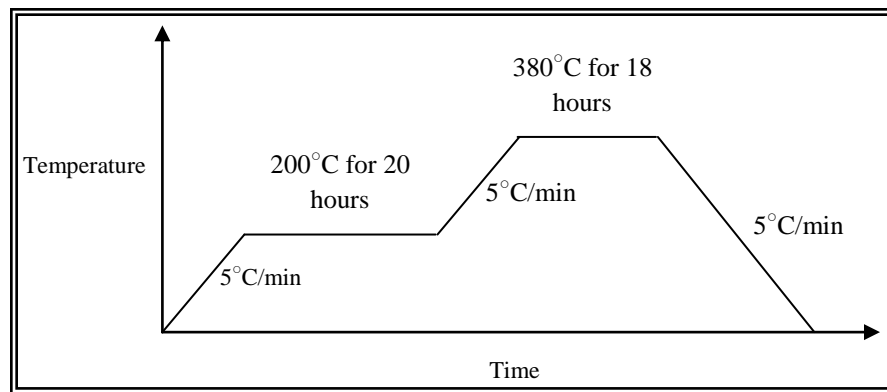


Figure 3.8: Heat treatment procedure of 35 wt. % GNF-PEEK composite.

3.2.2 35 wt. % GNF-PA 66 Composite

Heat treatment of 35 wt. % GNF-PA 66 samples invariably increased their thickness, although length and width were largely unaffected. This swelling problem was resolved by applying pressure (about 100 gr/cm²) to the flat samples during heat treatment, using steel plates and a weight placed on top of each sample to maintain a constant pressure throughout the sample. Heat treatment was carried out at 280°C for 24 hours (melting point 261°C) using a heating and cooling rate of 5°C/min.

Chapter 4

Analytical Instruments

In what follows, analytical instruments used to gain a better understanding of mechanisms and kinetics involved in composite processing and post-fabrication heat treatment are briefly described.

4.1 Scanning Electron Microscope

A Zeiss-Sigma Scanning Electron Microscope (SEM) with a Schottky Field Emission (FE) source and a GEMINI electron optical column is shown in Figures 4.1 and 4.2. It features detectors that allow imaging of particles and surfaces, as well as measurements of their compositions.

The instrument has 3 detectors and an image analyzer:

- In-lens secondary electron detector
- Lateral secondary electron detector
- 4-quadrant backscatter electron detector

EDS system with fully digital image collection, transfer and analysis

Apertures are 20-120 micron in size and maximum accelerating voltage is 30kV. The instrument includes a 5-axis rotary stage. Sample sizes up to 20 cm are allowed [102, 103, 104].



Figure 4.1: Zeiss-Sigma scanning electron microscope.

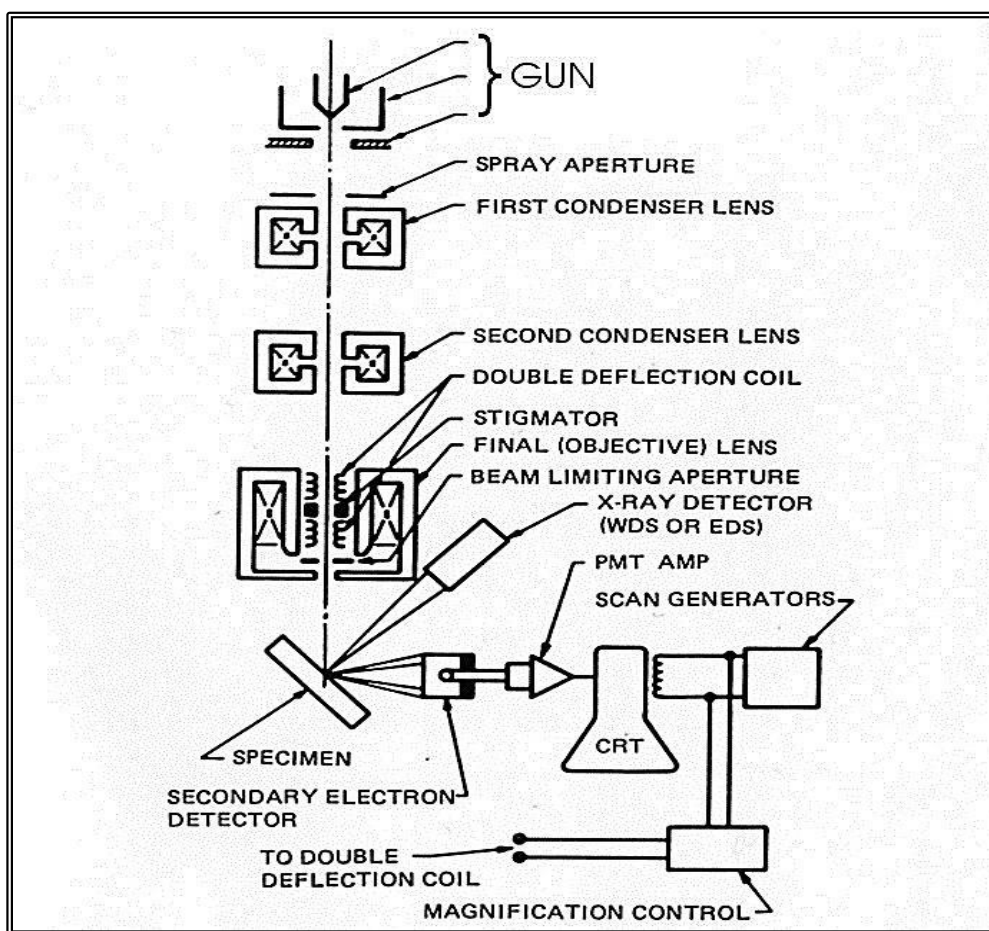


Figure 4.2: Schematic of a scanning electron microscope [105].

A FESEM collects signals generated when a focused beam of high energy electrons is scattered by the surface of a solid sample. The signals resulting from electron-sample interactions reveal information about morphology, chemical composition, crystalline structure, and orientation. In most cases, a 2-dimensional image is generated by collecting data over a selected area of the sample surface, while also providing qualitative or semi-quantitative analysis of chemical composition (using EDS), crystal orientations (using EBSD), and crystalline structure. According to the method and function adopted, the FESEM is considered to be similar to an Electron Probe Micro-Analyzer (EPMA), since there are common capabilities between the two instruments [105].

4.2 Differential Scanning Calorimeter

Using standard and temperature-modulated methods, a differential scanning calorimeter (DSC-model Q 1000, Figure 4.3) measures heat capacity, glass transition temperature, melting point, percentage of crystallinity and heat of fusion of samples. It is capable of performing up to 50 consecutive analyses with an auto sampler. Experiments can be conducted at temperatures as low as -180°C using a liquid- N_2 cooling system, and up to 550°C using a radiant heating system. Both standard aluminum pans and hermetically-sealed aluminum pans are available [106].



Figure 4.3: Q 1000 differential scanning calorimeter.

The DSC monitors the difference in heat flow between sample and reference material at the same temperature, and records data as a function of temperature. The reference material is made of an inert substance, such as alumina, or just an empty aluminum pan. The sample and reference material are heated at a constant rate. The heat flow equals the enthalpy change since the DSC is operated at constant pressure:

$$(dq/dt)_p = dH/dt$$

The difference in heat flow between the sample and the reference is:

$$\Delta(dH/dt) = (dH/dt)_{\text{sample}} - (dH/dt)_{\text{reference}}$$

This difference can be either positive or negative. In most phase transitions, heat is absorbed and therefore heat flow to the sample is higher than that to the reference material, which is called an endothermic process. Such endothermic processes include

melting, dehydration, reduction reaction, and some decomposition reactions in which the difference in heat flow is positive. In an exothermic process, such as crystallization, cross-linking processes, oxidation reactions and decomposition reactions, the difference in heat flow is negative [107].

- Endothermic: A transition that absorbs energy.
- Exothermic: A transition that releases energy.

4.3 Rheometer

The AR 2000 Rheometer equipped with a Mobius Drive, Figure 4.4, offers a broad torque range, high strain resolution, wide frequency range, and a Smart Swap for interchangeable temperature control options [108]. The apparatus has the following specifications:

Table 4.1: AR 2000 Rheometer features and specifications.

Feature	Specifications	Feature	Specifications
Minimum torque	0.1 $\mu\text{N.m}$	Motor inertia	15 $\mu\text{N.m.s}^2$
Maximum torque	200 mN.m	Angular velocity range	1 E-8 to 300 rad/s
Standard mobius drive	yes	frequency range	1.2E-7 to 100 Hz
Displacement resolution	0.04 μrad	Porous carbon air bearing	yes
Standard auto gap set	yes	gap resolution	0.06 μm
Normal force range	0.01 to 50 N	Peltier plate control	-20 to 200°C
concentric cylinder control	-10 to 150°C	Environmental test chamber	-150 to 600°C

Compared to other materials, such as metals and ceramics, the properties of polymers strongly depend on temperature and time, which is attributed to their inherent viscoelastic behavior, i.e. polymers react elastically to a rapidly applied force and in a more viscous fashion to a slowly applied force. This dual nature makes the plastic behavior of polymers very complex. In the elastic mode the deformation is proportional to the applied force, whereas in the viscous mode the deformation rate is proportional to the applied force [109].



Figure 4.4: AR 2000 rheometer.

In general, two mechanical elements are described to explain the viscoelastic behavior of polymers, Figure 4.5. A spring represents Hook's law of elasticity and a dashpot represents Newton's law of viscosity. These elements are used to explain two behavior models of polymeric materials. In the Voigt model spring and dashpot are placed in parallel, while in the Maxwell model they are placed in series. By combining these simple models, the behavior of polymers can be explained [110].

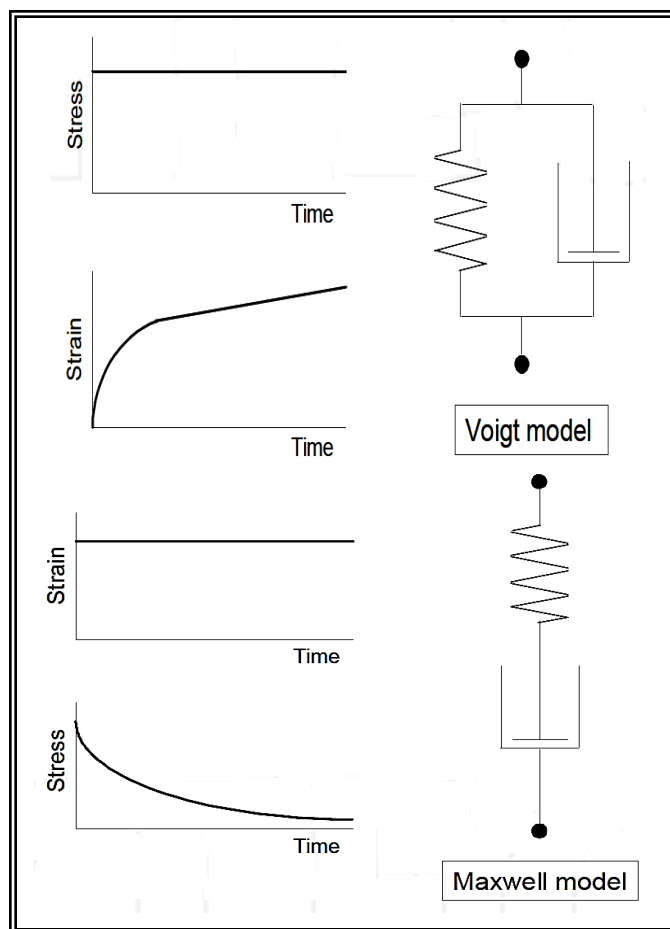


Figure 4.5: Voigt model illustrates the behavior of a polymer under a creep test, and Maxwell model illustrates the behavior of a polymer under a stress-relaxation test [110].

4.4 X-Ray Diffraction Unit

A PANalytical X-ray diffraction (XRD) unit equipped with on-board control electronics, offers high throughput, high-quality phase identification and quantification, residual stress analysis, grazing incidence diffraction, X-ray reflectometry, small-angle X-ray scattering, pair distribution function analysis, and non-ambient diffraction [111].

When the wavelength of the incident radiation is comparable with or smaller than the lattice constant of a crystal, the diffracted beams are obtained in directions different from the incident direction. W.L. Bragg put forward a simple explanation. If the incident

waves are reflected specularly from parallel planes of atoms in the crystal, with each plane reflecting only a very small fraction of the radiation, the angle of incidence is equal to the angle of reflection. The diffracted beams are formed when reflections from parallel planes of atoms experience constructive interference [112]. According to Bragg's analysis:

$$2d \sin\theta = 2\pi n\lambda$$

Where (d) is the spacing of parallel atomic planes and ($2\pi n$) is the difference in phase between reflections from successive planes. The reflection planes have nothing to do with the surface planes bounding the particular specimen [112].

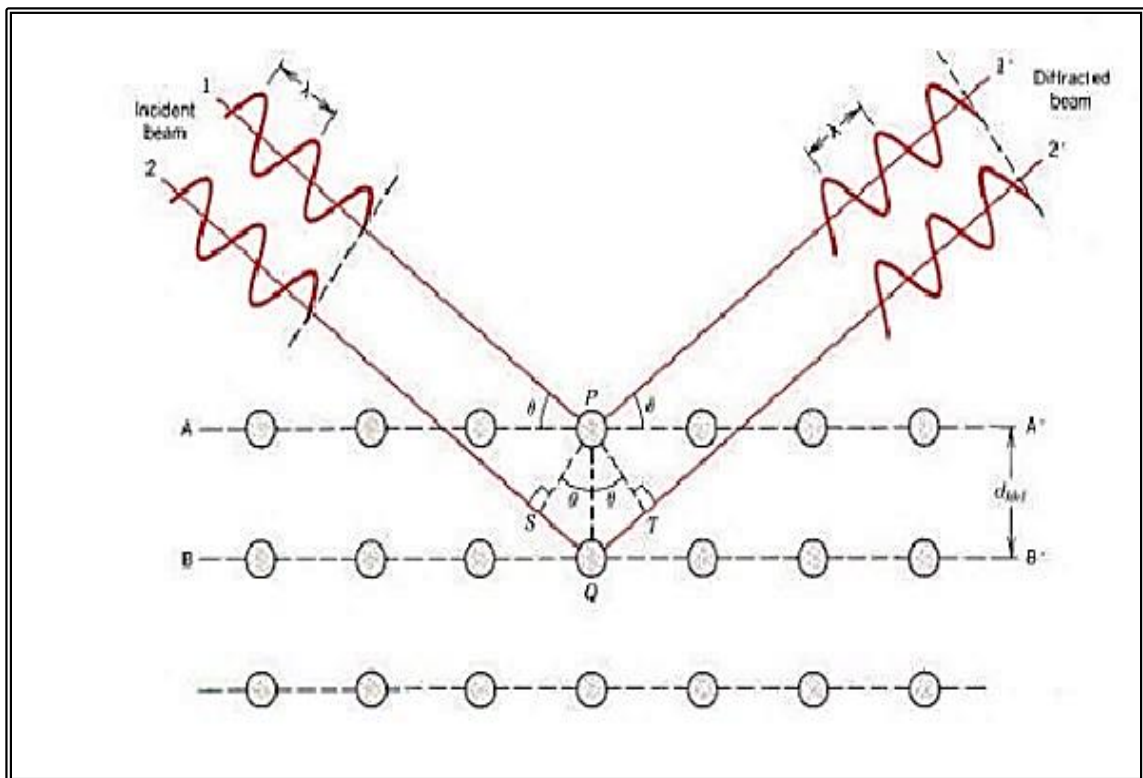


Figure 4.6: Incident and diffracted beams on a crystal plane [112].

4.5 Fourier Transform Infrared Spectroscopy

A hand-held 4100 ExoScan FTIR unit, Figure 4.7, is capable of analyzing samples on site that in the past could only be carried out in the laboratory. It is a versatile method for molecular compound identification and quantification, and allows analysis to be performed without damaging the sample, i.e. it is a non-destructive tool [113].

The instrument has the following specifications [113]:

Table 4.2: 4100 FTIR Spectrometer features and specifications.

Feature	Specifications
High-throughput Michelson interferometer with fixed and moving flat mirrors	
Standard beam splitter, zinc selenide	
Maximum spectral resolution	4 cm^{-1}
Low power solid state laser	
Wire-wound element source	
Spectral range	$4000\text{ to }650\text{ cm}^{-1}$
Detector	1.3 mm diameter, thermoelectrically cooled



Figure 4.7: 4100 ExoScan FTIR unit.

FTIR spectrometer uses a source of infrared (IR) light to pass through the sample and onto a detector, then the amount of light absorbed by that sample is measured precisely. The amount of absorption is a unique spectral fingerprint that identifies the molecular structure of the sample, and determines the exact quantity of a particular compound in a mixture [113].

4.6 Universal Testing Machine

An MTS Q Test 25 universal testing machine, Figure 4.8, is ideal for tensile testing of plastics, elastomers, and their composites. It is also suitable for flexural, shear, peel or compression tests on materials and components [114].

An MTS Q Test 25 testing machine has the following specifications [114]:

Table 4.3: MTS Q Test universal testing machine features and specifications.

Feature	Specifications
Load capacity	25 kN
Maximum crosshead speed	1,016 mm/min
Minimum crosshead speed	0.025 mm/min
Speed accuracy	0.25%
Frame stiffness	123 kN/mm



Figure 4.8: MTS Q Test 25 universal testing machine.

4.7 Impact Testing Machine

An Instron POE2000 low-energy impact machine is used for testing plastics, ceramics, composites, and other non-metals, using specimen standard ASTM D256-92 and ISO 180-1982(E) [115].

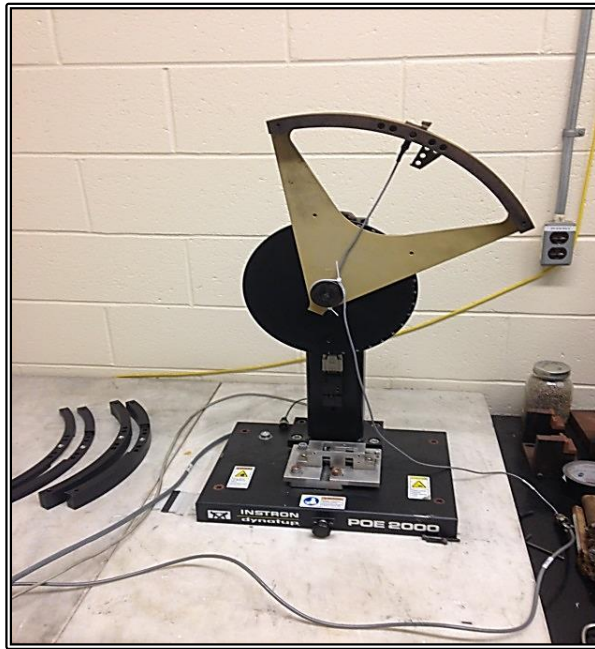


Figure 4.9: Instron POE2000 low energy pendulum tester.

This instrument has the following specifications [115]:

Table 4.4: Instron POE2000 impact machine features and specifications.

Feature	Specifications
Radius of strike	318.3 mm
Drop height	adjustable from 0.62m
Maximum impact velocity	3.5 m/s with adjustable angle of fall

4.8 X-ray Photoelectron Spectrometer

Thermo Scientific's K-Alpha X-ray photoelectron spectrometer (XPS) is designed for a multi-user environment. The analytical options include tilt module for data collection, and recirculating inert-gas glove box for transfer of air-sensitive samples [116].

The K-Alpha XPS has the following specifications [116]:

Table 4.5: K-Alpha XPS features and specifications.

Feature	Specifications
Analyzer	180° double focusing hemispherical analyzer, 128-channel detector
X-ray source	Al K α micro-focused monochromator, with variable spot size 30-400 μm
Charge compensation	Dual beam source, ultra-low energy electron beam Ion Gun
Energy range	100 eV to 4 keV
Sample handling	60 \times 60 mm sample area, 20 mm maximum sample thickness
Vacuum system	2 x 260 l/s turbo-molecular pumps for entry and analysis chambers

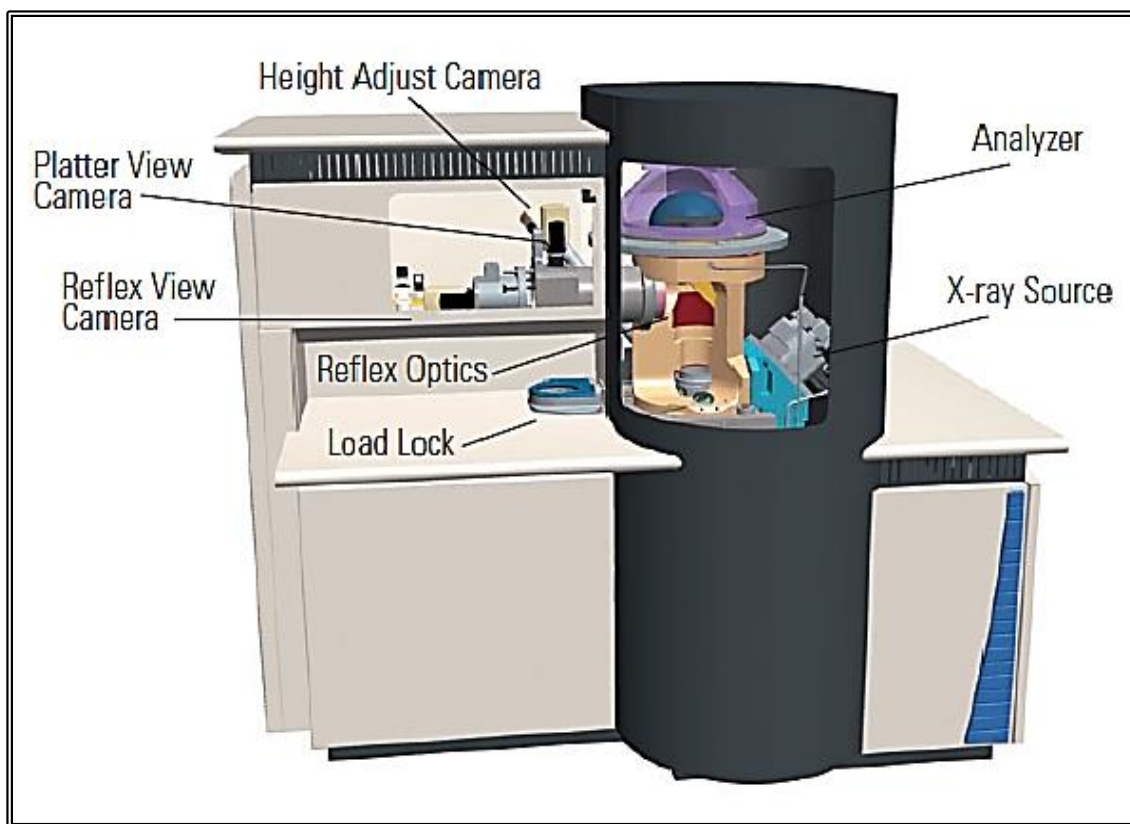


Figure 4.10: Thermo Scientific's K-Alpha X-ray photoelectron spectrometer [116].

When an X-ray beam is directed onto the surface of a material, its energy causes excitation of the bonding electrons and giving them enough kinetic energy to leave that surface into the surrounding, Figure 4.11. Due to the fact that every bond in the material surface has different amounts of electrons with different kinetic energies, this effect is adopted as means to determine the nature of bonding on any surface [117].

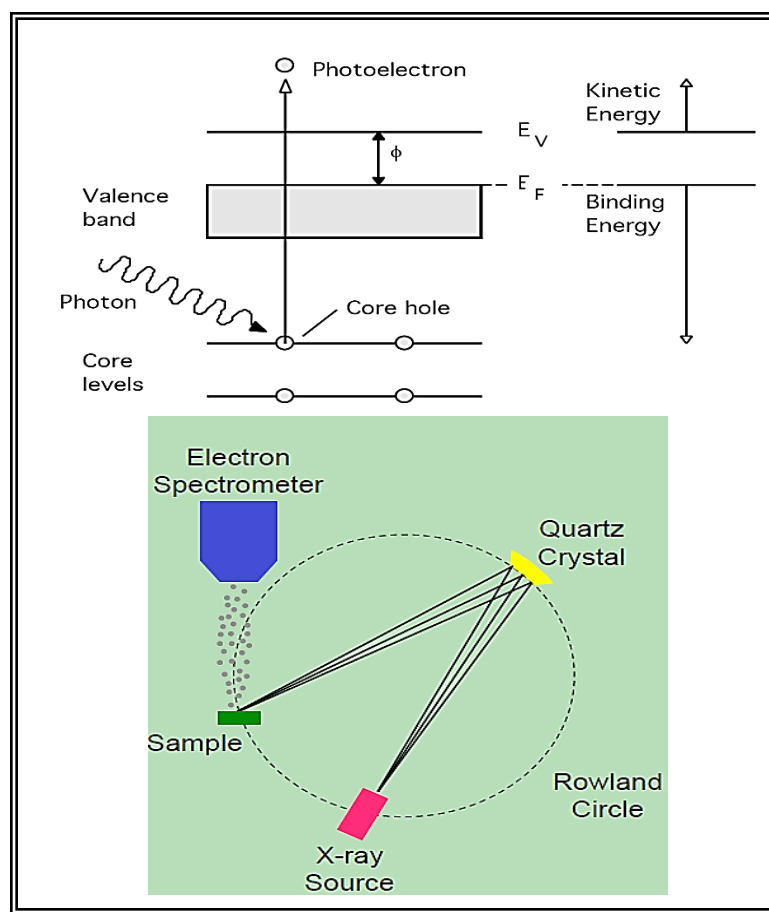


Figure 4.11: Photoelectric effect (up) and XPS work principle (down) [117].

4.9 Transmission Electron Microscope

JEOL's 2010F Field-Emission Scanning Transmission Electron Microscope (FE-STEM) is capable of direct lattice imaging and composition analysis via EDS and EELS/GIF [118].

JEOL's FE-STEM has the following specifications [119]:

- Acceleration voltage 20-200kV with ZrO-W field emission source
- Scanning Transmission Electron Microscopy (STEM) interface
- Digital imaging with 1Kx1K CCD camera
- BF/DF STEM detectors
- HADF STEM detector

- Electron Energy Loss (EELS) spectrometer
- Kx2K GATAN imaging EELS filter (GIF)
- Heating (1400K) and cooling (90K) holders



Figure 4.12: JEOL 2010F scanning transmission electron microscope.

A schematic ray diagram, Figure 4.13, shows:

- 1) Illumination system, which takes the electrons from the gun and transfers them to the specimen, giving either a broad beam or a focused beam.
- 2) Objective lens and stage, which is the heart of the TEM.
- 3) TEM imaging system, which includes intermediate lens and projector lens.

At the back focal and image planes of the objective lens, the diffraction pattern and image are formed. To obtain the diffraction pattern on the screen, the back focal plane is selected as the objective plane of the intermediate lens and projector lens. In this case, the TEM works in a diffraction mode. To form an image on the screen, the image plane of the objective lens is selected as the objective plane of the intermediate lens and projector lens, which is called the imaging mode [120].

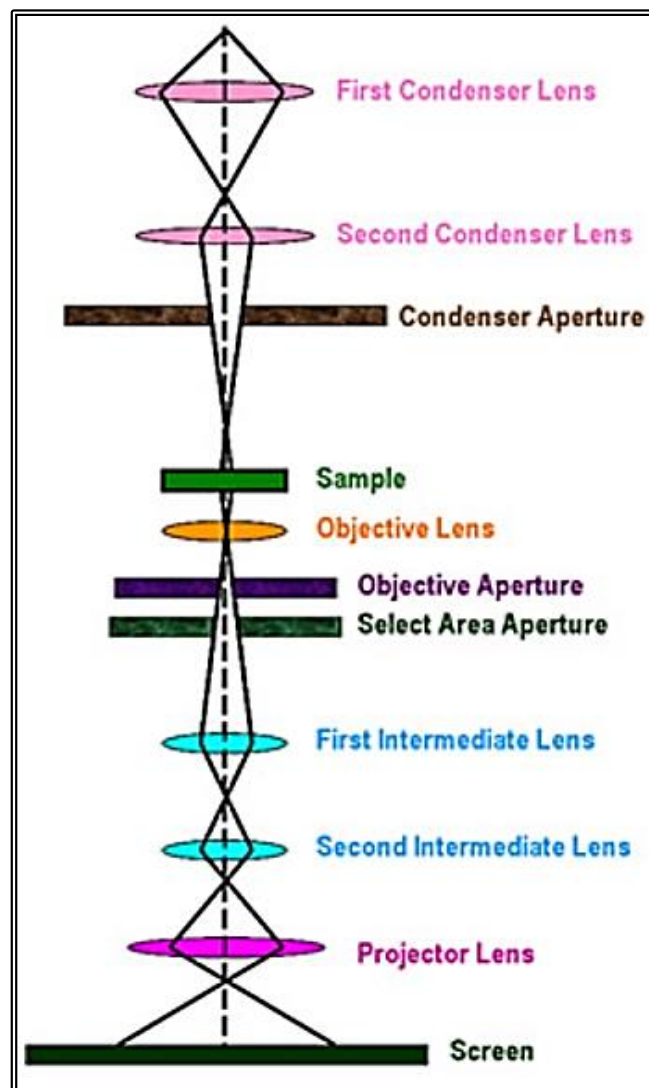


Figure 4.13: Ray diagram for a transmission electron microscope [120].

Chapter 5

Results and Discussion

Processing and Characteristics of MWCNT-Reinforced PA 66 Composites

In what follows, samples of 1-8 wt. % MWCNT-reinforced PA 66 (Nylon) composites, prepared using the batch mixer described in Chapter 3, are analyzed using the techniques described in Chapter 4, and the results discussed.

5.1 DSC Tests and Results

In this research, DSC tests are performed on PA 66 samples that contain 1-8 wt. % MWCNTs. All samples weighing 10-15 mg are vacuum dried at 90°C for 24 hours. Heating and cooling rates are set at 10°C per minute. The first heating cycle eliminates the thermal history of the sample resulting from previous processing. As the sample cools down slowly during the following cooling cycle, polymer chains rearrange themselves into ordered bundles characteristic of the crystalline state. The intensity of the corresponding crystallization peak increases with decreasing cooling rate due to a greater degree of crystallization. The second heating cycle of the sample reveals its glass transition temperature and melting point. Typically, the temperature range of a DSC test starts at 30-60°C below the lowest temperature expected transition and ends at about 30°C above the highest transition temperature.

Since the known glass transition, crystallization, and melting temperatures of PA 66 are 60°C, 225°C and 262.5°C respectively, (Figure 3.4) all tests are performed over the 0-350°C range to ensure that all phase transitions are detected. Each test is conducted three times on samples weighing about 10 mg using a standard heating-cooling heating cycles and 10°C/minute rate for both heating and cooling to obtain reliable data.

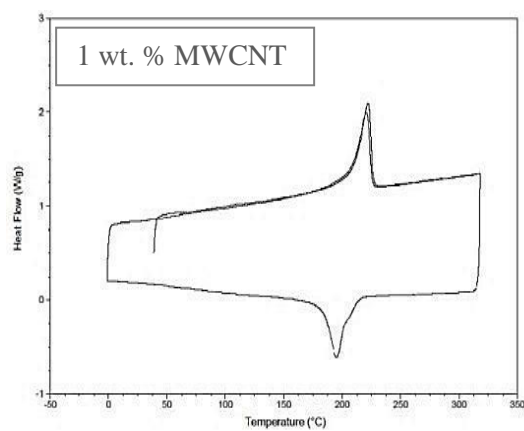
Figure 5.1 shows a series of DSC heating-cooling-heating curves for the composite samples, plotting heat flow (W/g) versus temperature ($^{\circ}\text{C}$). Figure 5.2 shows the first heating cycle, it reveals that the melting point of the PA 66 matrix decreases from 262°C to 220.2°C at MWCNT addition of 1 wt. % and continues decreasing to 219.2°C at MWCNT addition of 5 wt. %, then melting point increases to 256.7°C with MWCNT addition of 6 wt.% and continues increasing afterwards. The first decrease in melting point in the range 1-5 wt. % MWCNT-PA 66 is believed to be due to an increase in low molecular weight polymer fragments generated when MWCNTs are introduced into the mixing unit, as suggested by Kartel et al [121]. On the other hand, the following increase in melting point at higher weight fractions of MWCNTs is suggesting the beginning of a cross linking between polymer chain fragments.

Since the mixing process efficiently distributes and fractures the original MWCNTs, a very large number of dangling bonds are formed at their fractured ends. It is believed that these form covalent bonds with the molten polymer molecules, initiating a secondary crystallization process that yields a modified PA 66 structure, as discussed below. The transition to this new mode of crystallization occurs at 6 wt. % MWCNTs, at least for this particular mixing time and rate. Increasing mixing time and rate, under otherwise the same processing conditions, could reduce the critical concentration of MWCNTs required to induce this modified crystallization process. Direct observation by TEM indicates that the fractured ends of MWCNTs are associated with higher density regions of crystalline PA 66.

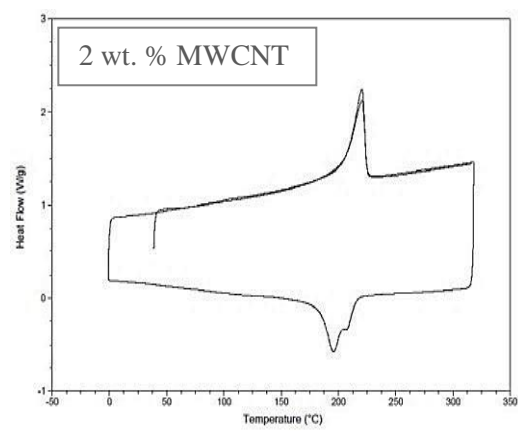
Such behavior is supported by the DSC cooling cycle curves in Figure 5.2, which show a gradual appearance of a second crystallization peak located above 200°C with

increasing additions of MWCNTs. The second peak grows in intensity, at the expense of the first peak, up to 6 wt. % CNT, at which point there is only a minor change in crystallization behavior. This suggests that 6 wt. % addition of MWCNTs appears to be a threshold composition, dividing the two regions of crystallization behavior.

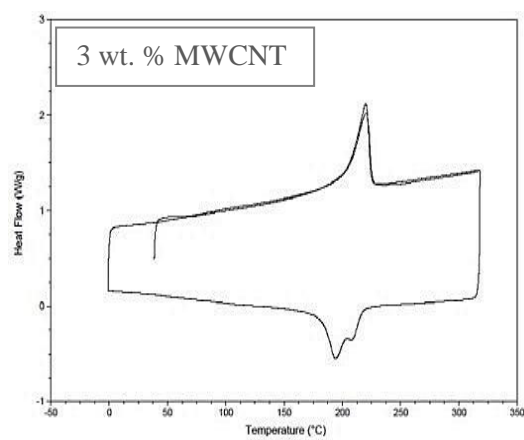
The second crystallization peak that grows in intensity with MWCNT additions in the 1-5 wt. % range indicates an increasing degree of interaction of polymer chains with MWCNTs in the composite, forming a more thermally stable crystalline state for the polymer matrix. This is described herein as secondary crystallization to distinguish it from primary crystallization. After passing the threshold at 6 wt. % MWCNTs, this new crystallization behavior dominates, corresponding to about 40°C increase in crystallization temperature. Close examination of the DSC curves indicates that the new exothermic peak increases from 236.7 to 238.9 to 239.3°C for 6, 7 and 8 wt. % MWCNTs, respectively.



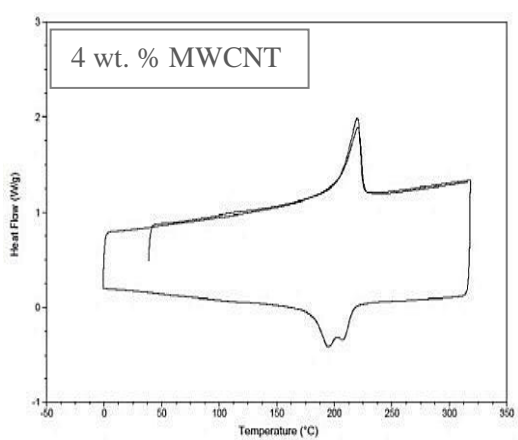
(a)



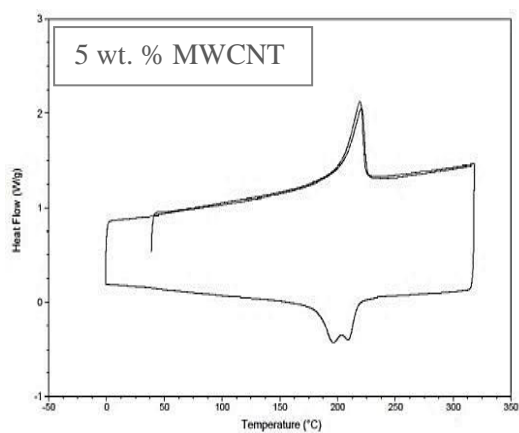
(b)



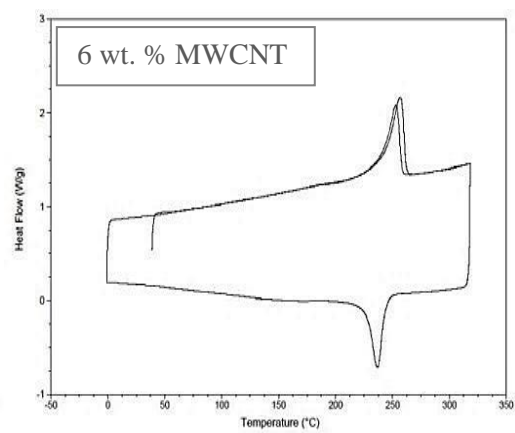
(c)



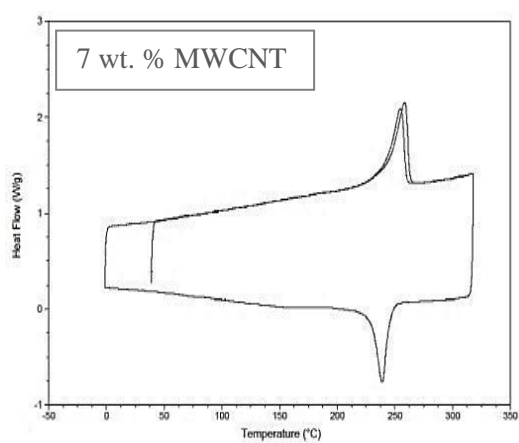
(d)



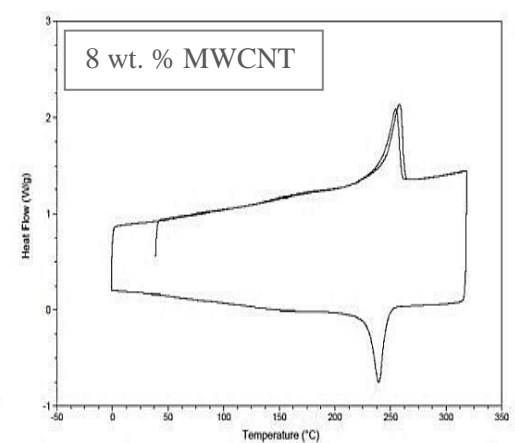
(e)



(f)

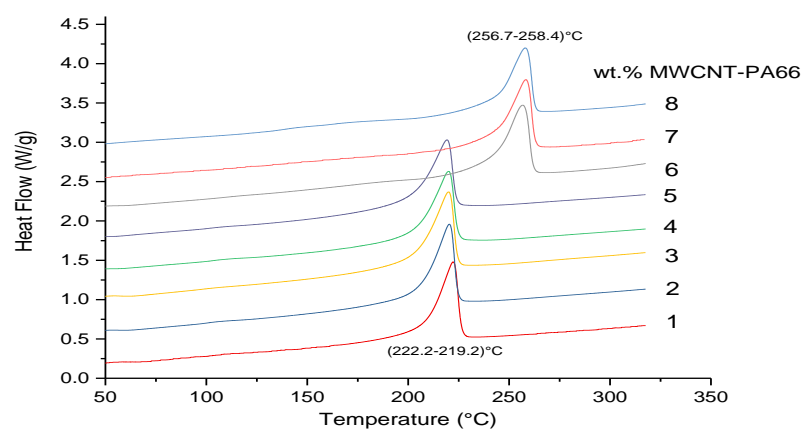


(g)

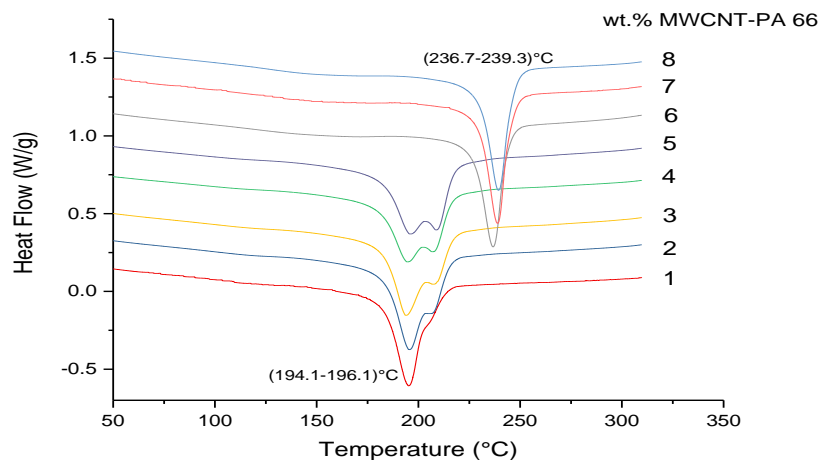


(h)

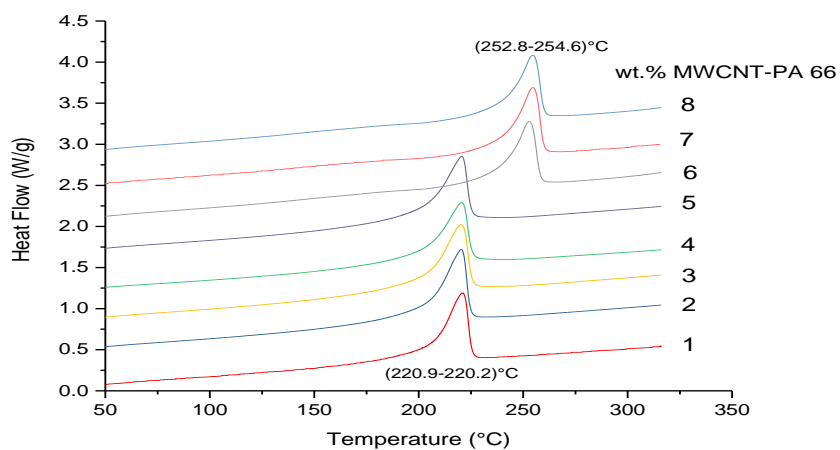
Figure 5.1: DSC curves of heat flow (W/g) vs. temperature (°C) for increasing wt. % MWCNTs in PA 66.



(a)

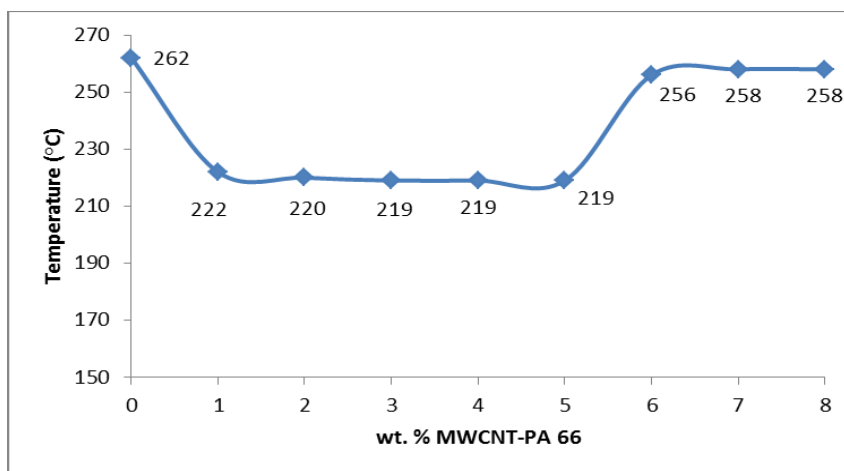


(b)

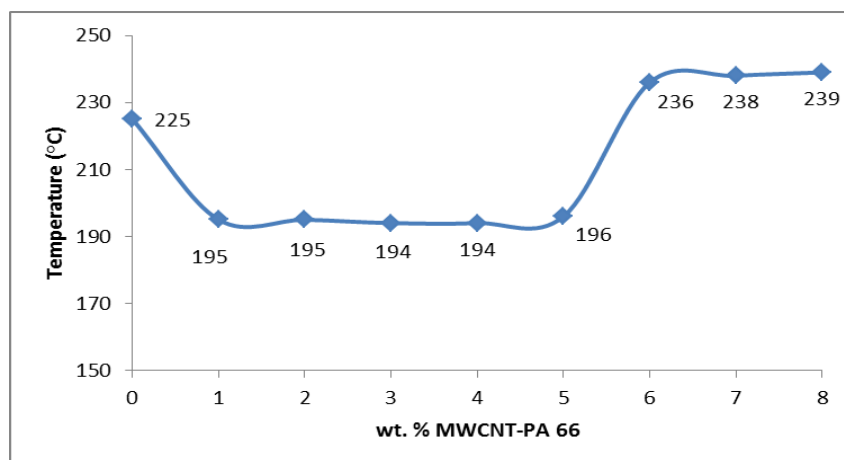


(c)

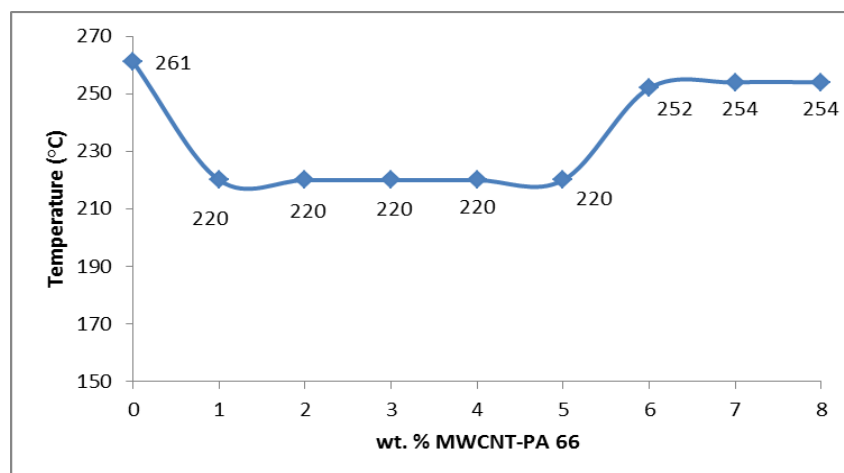
Figure 5.2: DSC curves of heat flow (W/g) vs. temperature (°C) for the (a) first heat, (b) cool, and (c) second heat.



(a)



(b)



(c)

Figure 5.3: a) first melting, b) crystallization, and c) second melting temperatures for PA 66 and MWCNT-PA 66 composites.

5.2 FTIR Tests and Results

Small amounts of PA 66 and its composites with MWCNTs are cryogenically milled in a SPEX unit and dried at 90°C for 24 hours. After drying, the fine powder is mixed with dried KBr (100°C for 6 hours), crushed using a pestle and mortar, and cold-pressed into disc-shaped specimens using a Carver press (5.5 metric ton pressure). Each specimen is 1 cm in diameter and 1-2 mm thick, weighs about 0.8 g, and comprises 2% sample-98% KBr. Specimens are placed in an FTIR cell and their spectra recorded. In all cases, a calibration test is run before the actual test and each specimen was tested on three different points.

Figure 5.4 shows an FTIR spectrum for PA 66. Frequencies of all fundamental bands, their relative intensities, and probable assignments are given in Table 5.1.

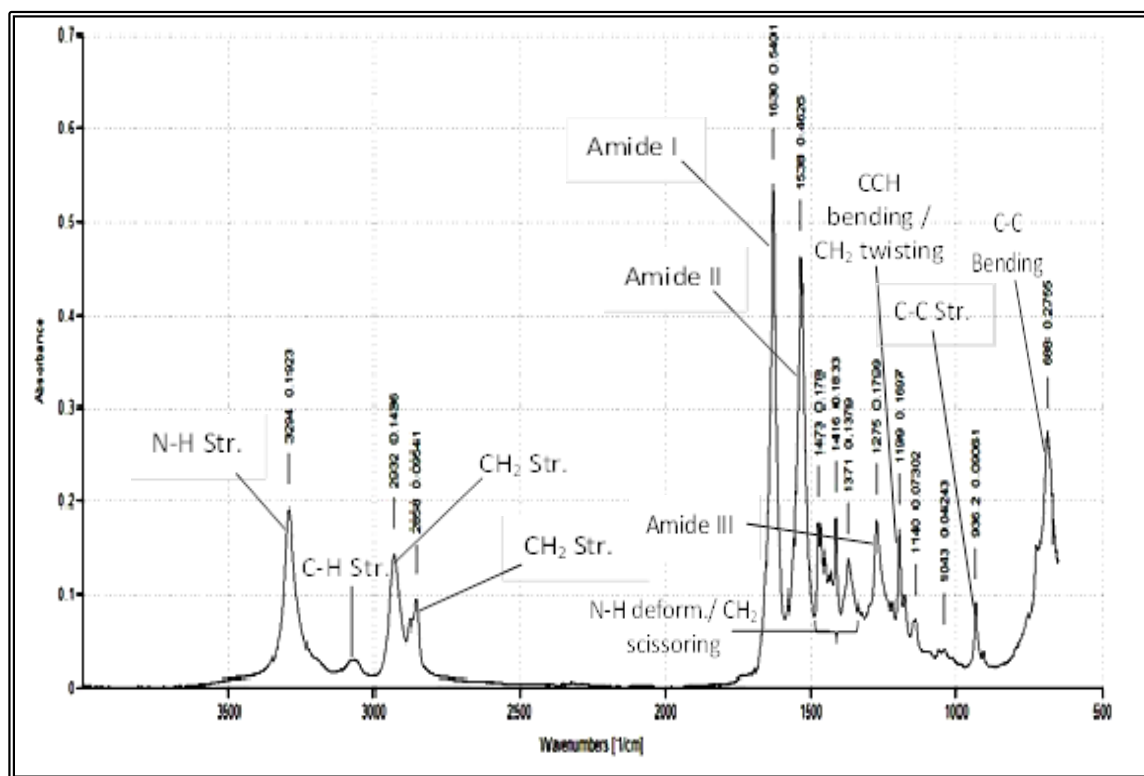
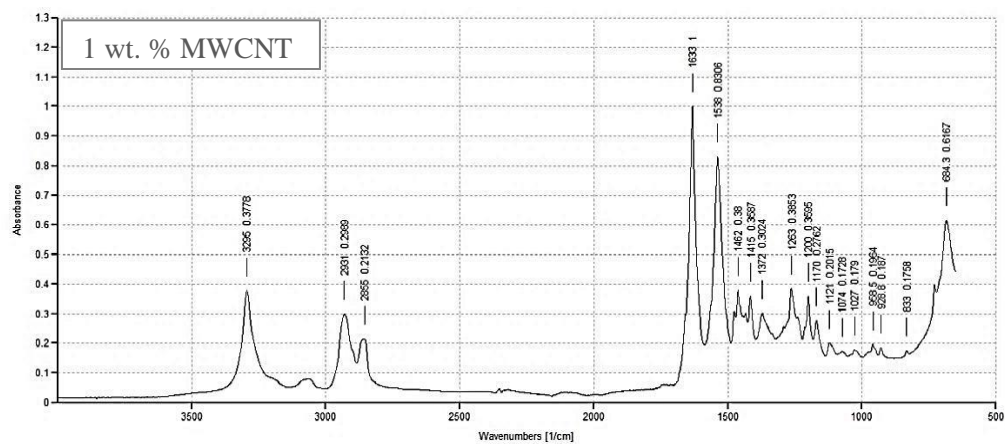


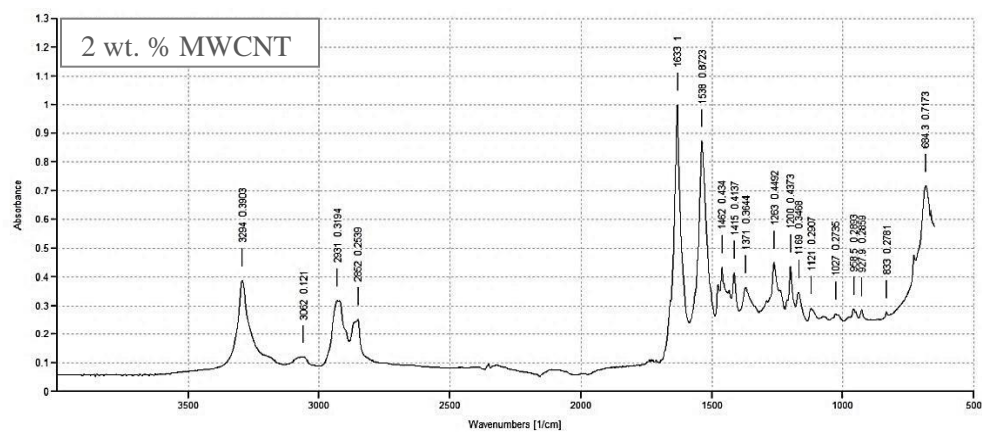
Figure 5.4: FTIR spectrum for PA 66, plotting absorbance vs. wave number (cm^{-1}).

Table 5.1: FTIR assignments of peaks for PA 66.

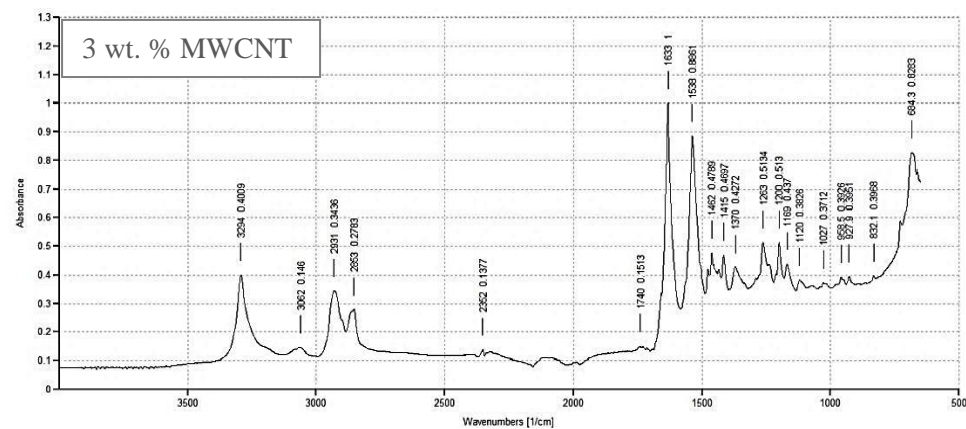
Wave number	Absorbance	Assignment
3294	0.1923	N-H stretching
3076	0.0305	C-H stretching
2932	0.1436	CH ₂ stretching
2858	0.0954	CH ₂ stretching
1630	0.5401	Amide I stretching (Carbonyl str. C=O)
1538	0.4626	Amide II stretching (N-H stretching)
1473	0.1780	N-H deformation /CH ₂ scissoring
1275	0.1799	Amide stretching
1199	0.1697	CCH bending/CH ₂ twisting
936	0.0906	C-C stretching
688	0.2755	C-C bending



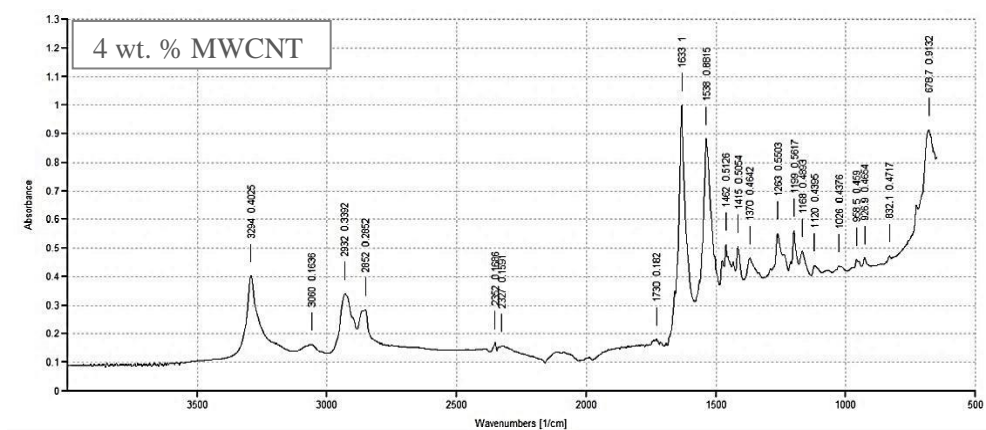
(a)



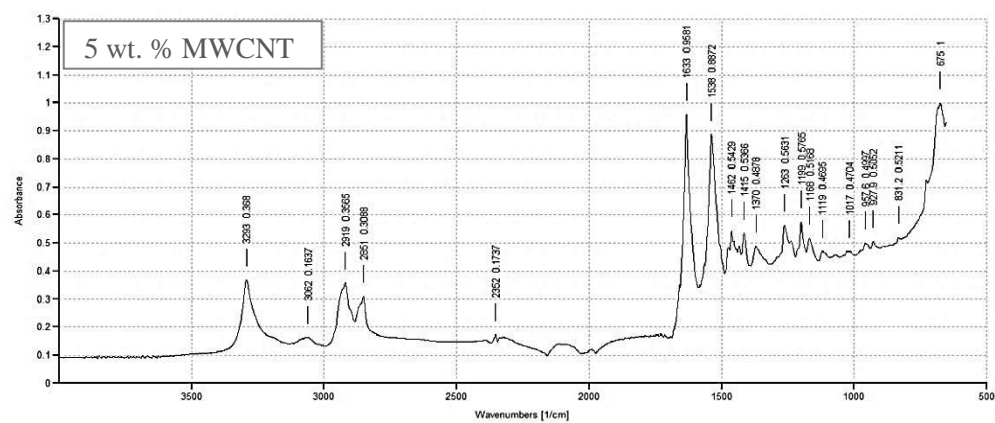
(b)



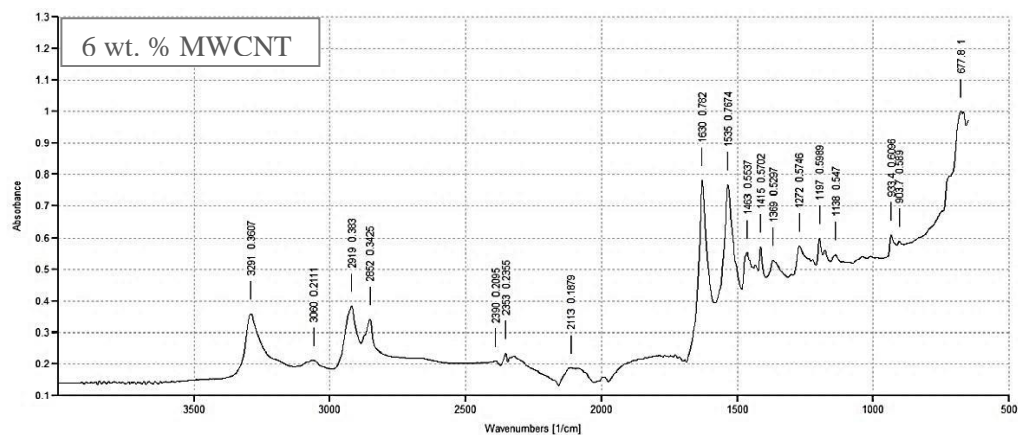
(c)



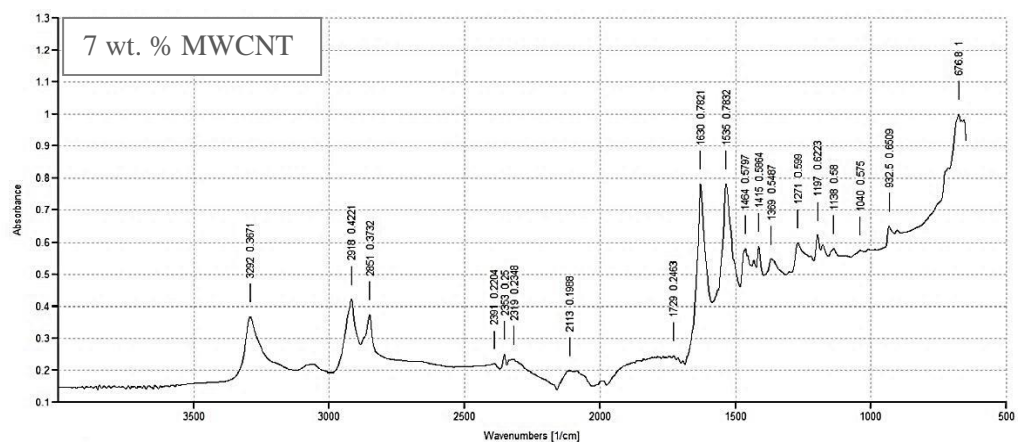
(d)



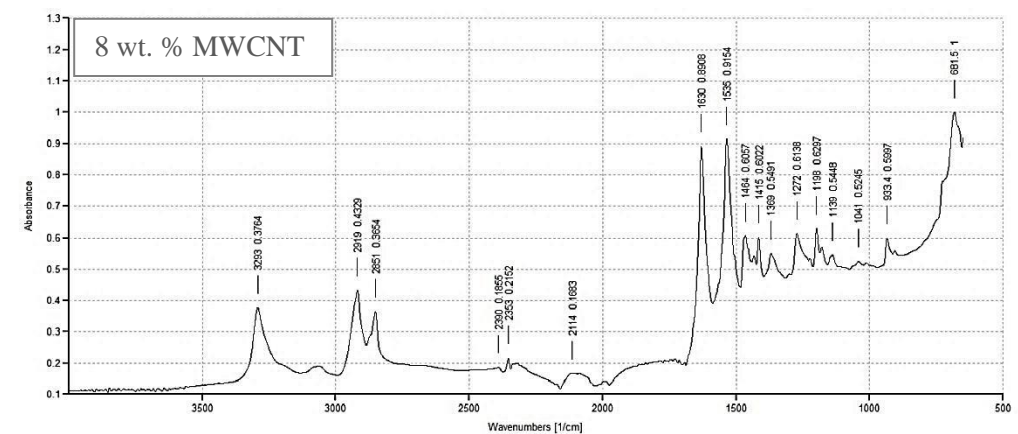
(e)



(f)



(g)



(h)

Figure 5.5: FTIR spectra showing absorbance vs. wave number (cm^{-1}) for increasing wt. % MWCNTs in PA 66.

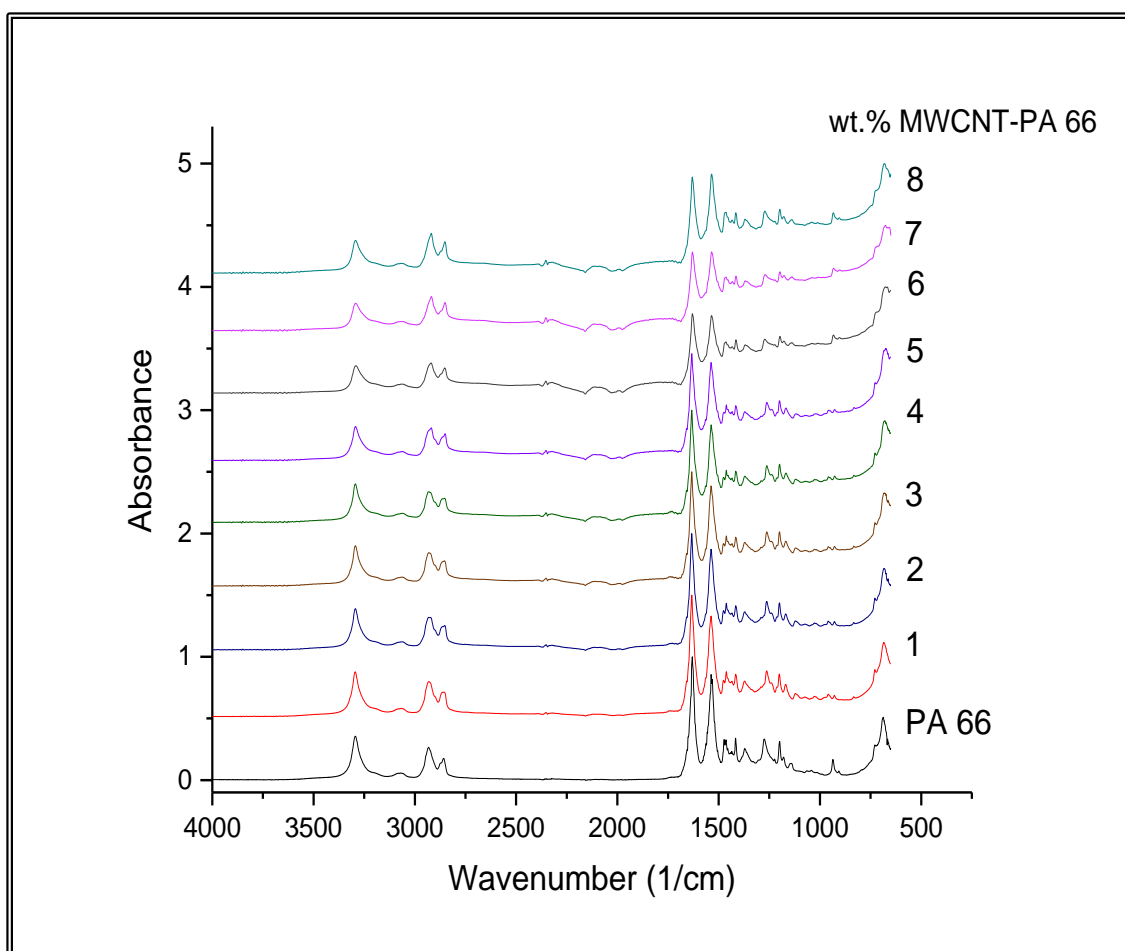


Figure 5.6: A collective draw of FTIR spectra showing absorbance vs. wave number (cm^{-1}).

Figure 5.5 (a) shows that when the MWCNTs are introduced into PA 66, all distinctive polymer peaks are doubled in intensity. This is probably due to the IR phonon sensitive nature of MWCNTs, which leads to general amplification of peak intensities. Also, there is no significant shifting in peak positions compared to pure PA 66, indicating no major disruption of the chemical structure. Moreover, the FTIR spectrum of 1 wt. % MWCNTs marks the appearance of a broad peak around 2100 cm^{-1} a distinguishing feature for additions of CNTs, graphite or carbon black.

The increase in intensities of peaks, including those for carbon-addition, proceeds systematically until 6 wt. % MWCNT, where a noticeable decrease in Amide I and Amide II stretching peak intensities occur, accompanied by a shift to lower (by 3) wave numbers. Meanwhile, all peaks positioned to the right of these ones (near C-C bonding region) continue to grow in intensity, with some shifting to higher wave numbers. This behavior suggests that at 6 wt. % MWCNTs, the PA 66 matrix shifts from its original structure to a new crystalline state. This effect is believed to occur at fractured ends of MWCNTs, as discussed in TEM results.

Then, all FTIR peaks of 6 wt. % MWCNT in PA 66 continue to grow steadily in intensity on 7 and 8 wt. % MWCNT, while maintaining the new shifted positions. As previously, we believe this effect can be attributed to the IR phonon sensitive nature of MWCNTs.

5.3 Mechanical Properties

Due to the limited capacity of the batch mixer, it was not possible to fabricate standard ASTM-D790 specimens (commonly called Type I ASTM specimens) to measure flexural modulus of MWCNT-PA 66 composites. Hence, all experiments were conducted using smaller than standard ASTM-D790 specimens (commonly called Type V ASTM specimens) that were fabricated using a manually-operated injection molder, Figure 5.7. These specimens were also used for impact testing, according to ASTM D 256.



Figure 5.7: Manually-operated injection molder.

5.3.1 Three-Point Flexural Test

Flexural properties were measured using a three-point bending device, Figure 4.8, according to a modified ASTM D 790 method. The cross-head speed was 5 mm/minute and maximum strain was set to 0.05 mm/mm. For each sample, 8 – 10 specimens were tested and resulting properties averaged.

Flexural results for 0-8 wt. % MWCNT-PA 66 composites are shown in Figure 5.8. The first decrease in flexural modulus (<3 wt. % MWCNT) might be ascribed to local degradation of the polymer matrix coming from the high thermal conductivity of MWCNTs or may be the introduction MWCNTs could disrupted the original crystallization of the matrix. At high concentrations of MWCNTs (>3 wt. %) the modulus increased gradually to reach 9.1 GPa at 8 wt. %, this could be attributed to repeated fracture of MWCNTs occurs during mixing, which increases stiffness via covalent bonding between newly-fractured ends of MWCNTs and the molten polymer matrix [122]. Specifically, it is proposed that dangling bonds formed at fractured ends of MWCNTs might covalently bond to the weakest links (e.g. oxygen bonds) in the long-chain molecules of PA 66. For this particular set of processing parameters, the transition from one mechanism to the other occurs at 3 wt. % MWCNTs, but this could change with mixing temperature, shear rate, and mixing time. The reduction in peak stress at fracture with increasing wt. % MWCNTs, Figure 5.9, is likely due to the embrittlement effect of introducing MWCNTs which makes the composite sensitive to any stress raisers.

When significant overlap or bridging between neighboring edge-covalently bonded regions occurs during high-shear mixing, near-maximum values of stiffness and strength are anticipated. In accord with the proposed model, observations by high-resolution TEM

(Section 5.5) show that the density of the polymer matrix is higher near fractured ends of MWCNTs. It is believed that polymer densification in these regions is responsible for the increased density, likely due to bonding that is observed at the ends of the fibers, and the resulting very close dangling bonds created, and satisfied with bonding to polymer chains.

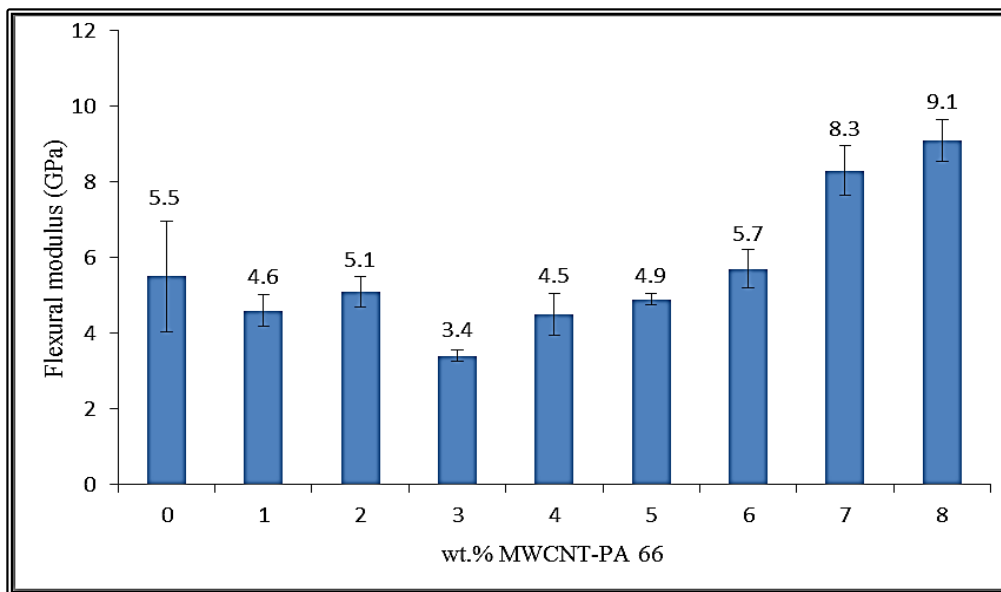


Figure 5.8: Bar chart showing flexural modulus (GPa) vs. wt. % MWCNTs in PA 66.

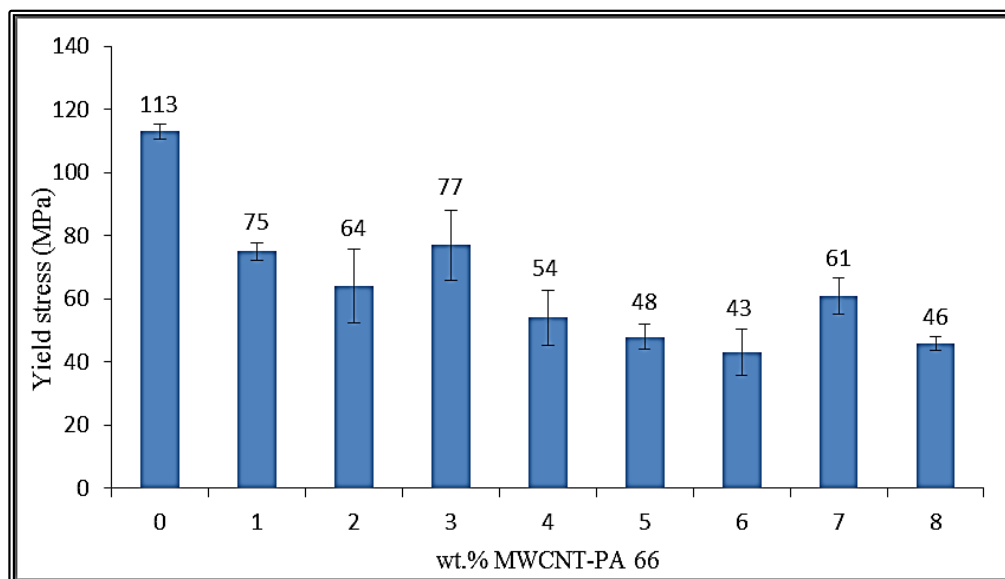


Figure 5.9: Bar chart showing peak stress (MPa) vs. wt. % MWCNTs in PA 66.

5.3.2 Impact Resistance

Izod impact resistance was determined using an instrumented pendulum Instron machine, Figure 4.9, according to ASTM D256. The impact energy was 21.7 J, and the impact velocity was 3.47 m/s. Before testing, width and thickness of each specimen were entered into the instrument software. For each sample, 8 – 10 specimens were tested and results averaged.

Impact resistance results (Figure 5.10) for 0 – 8 wt. % MWCNT-PA 66 composites, show a minimum of 43 J/m at 2 wt. % MWCNTs, a maximum of 434 J/m at 5 wt. %, and another minimum of 45 J/m at 8 wt. %. At low MWCNT percentages, the observed first decrease in impact resistance may be ascribed to local degradation of the polymer matrix due to high thermal conductivity of MWCNTs or disrupting original crystallization by MWCNTs introduction, whereas the following increase can be attributed to a dominant bridging mechanism resulting from length reduction of MWCNTs and covalent bonding at the MWCNT ends and PA66 matrix. As the amount of MWCNTs increases (>5 wt. %), embrittlement effect dominates the structure of the composite causing the second decrease in impact resistance [122].

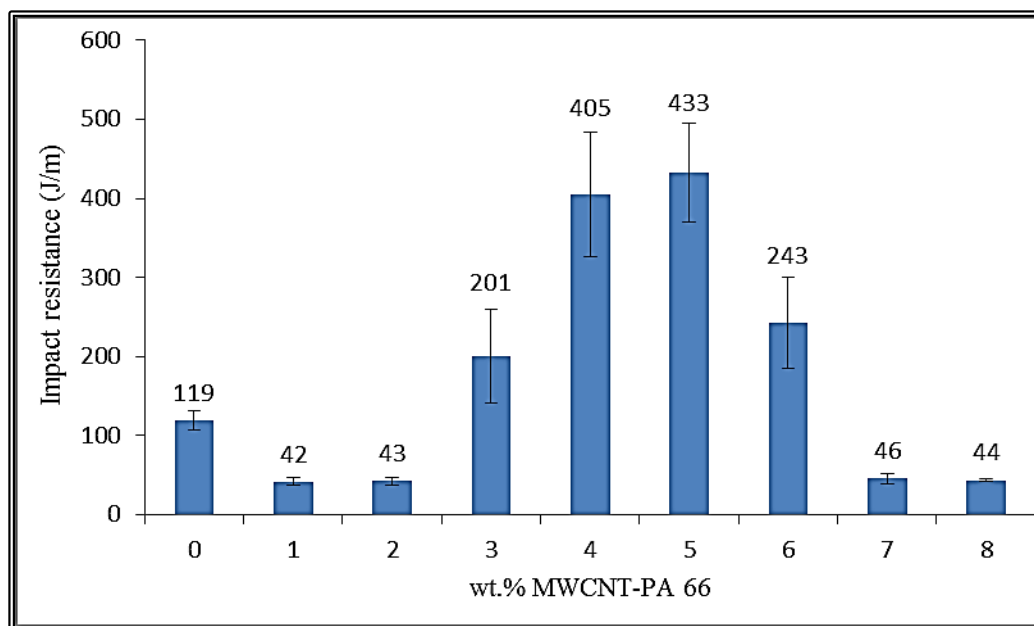


Figure 5.10: Bar chart showing impact resistance (J/m) vs. wt. % MWCNTs in PA 66.

5.4 Morphology and Fracture Behavior

Specimens of MWCNT-PA 66 composites were cryogenically fractured, vacuum dried at 85°C for 24 hours, attached to aluminum studs using double-sided adhesive carbon tape, sputter-coated with a 3-5 nm layer to mitigate electron beam- induced charging, and stored in a desiccator prior to FESEM observations.

At low magnifications, fractured surfaces invariably display wave-like patterns of micro-cracks, Figure 5.11. In the two examples shown, differences in contrast of micro-cracks are ascribed to differences in crack-opening displacements - larger in (a) 2 wt. % MWCNT-PA 66 than in (b) 7 wt. % MWCNT-PA 66. At high magnifications, large crack-opening displacements in Figure 5.12 are clearly revealed, as is the presence of fine-scale dispersions of MWCNTs in the PA 66 matrix. It can be noticed that some MWCNTs are bridging the crack-openings.

At 8 wt. % MWCNTs, showed in Figure 5.14, there are isolated regions where the density of MWCNTs is much lower than the average and they might be an indicative of incomplete mixing. This observation is consistent with experience in high-shear mixing of this particular composition, where, due a large increase in melt viscosity, considerable difficulties were experienced in processing the composite. A similar incomplete-mixing effect is observed at 7 wt. % MWCNTs, but the amount of unmixed polymer is much less, and smaller in size. It is concluded, therefore, that the ability to produce a uniform distribution of MWCNTs in PA 66 by high-shear mixing is limited to compositions <7 wt. % MWCNTs, at least using the present equipment.

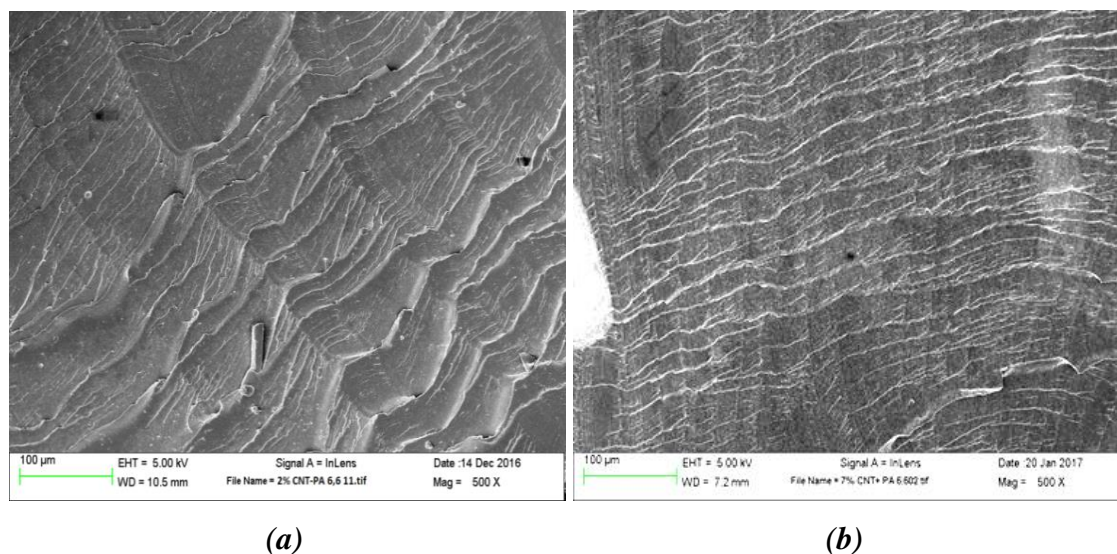


Figure 5.11: Low magnification FESEM images of fractured surfaces, showing wave-like patterns of micro-cracks.

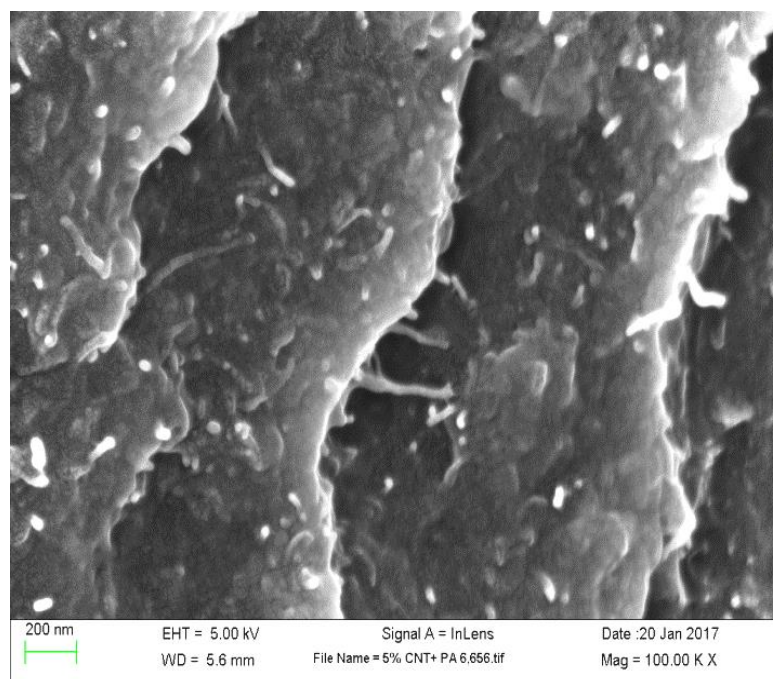
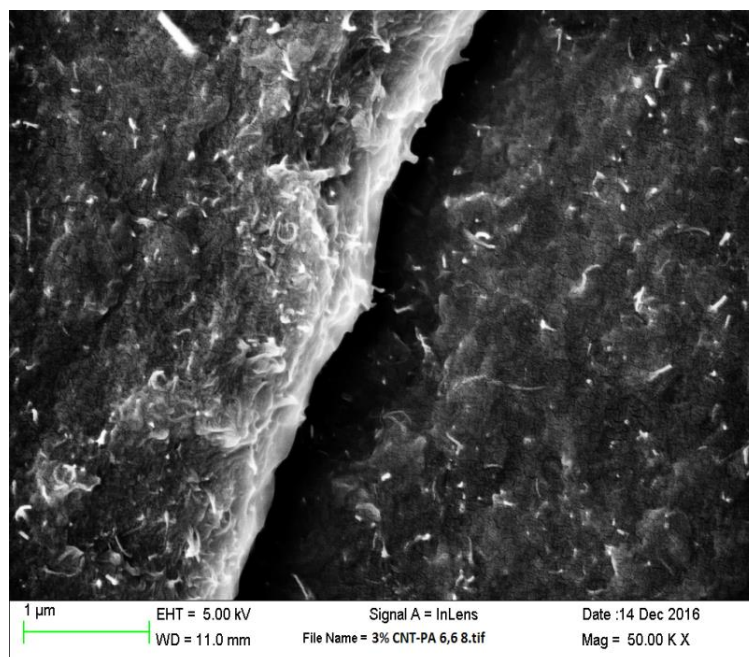
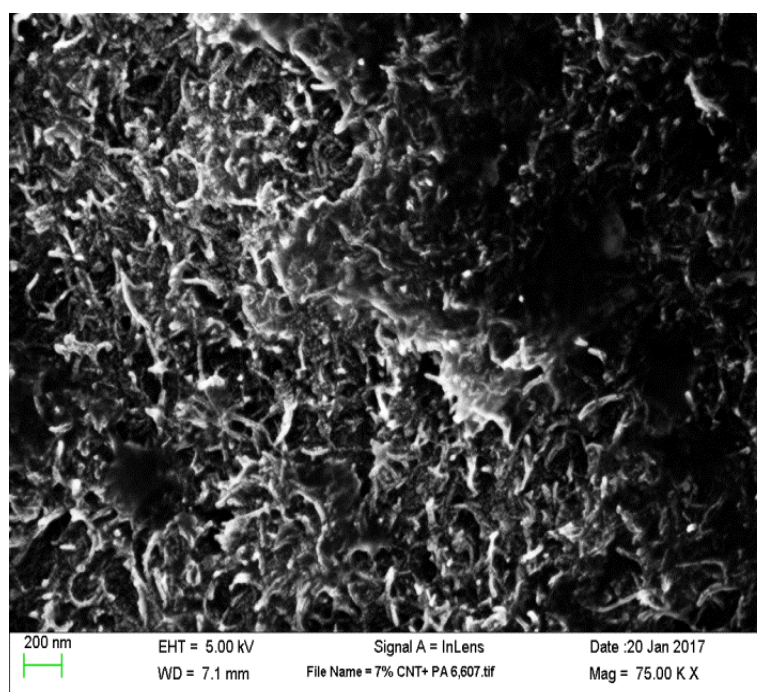


Figure 5.12: High magnification image of fractured surface of 5 wt. % MWCNT-PA 66 composite showing a series of micro-cracks and uniform distribution of MWCNTs.



(a)



(b)

Figure 5.13: High magnification images of MWCNTs in (a) 3 wt. % composition, and (b) 7 wt. % composition.

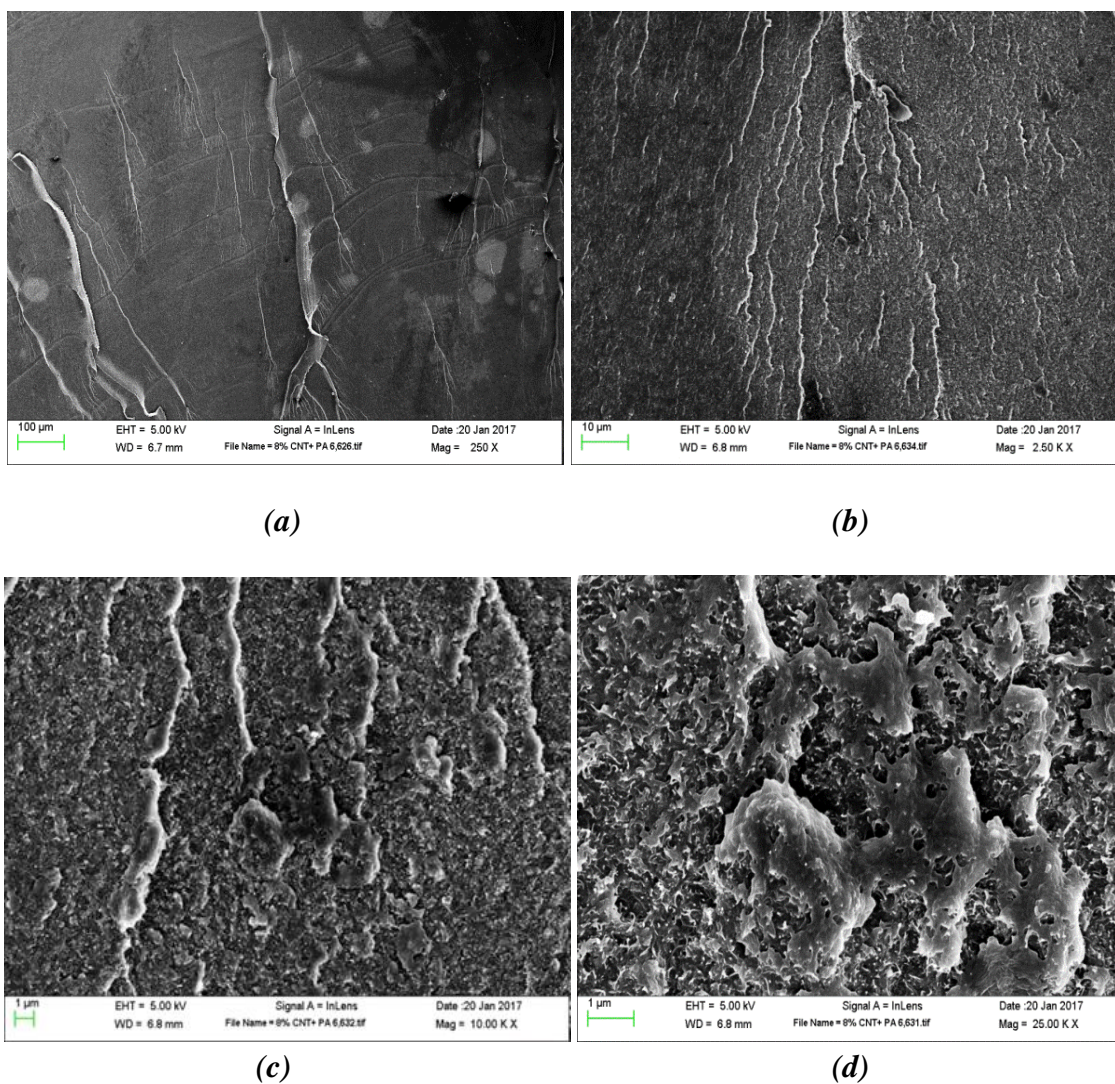
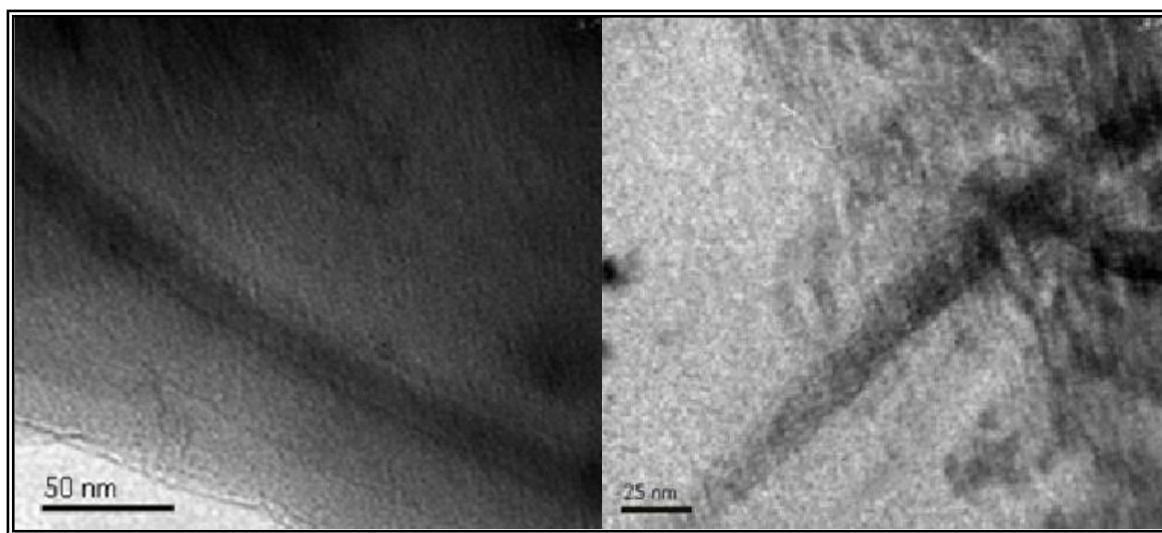


Figure 5.14: A series of low (top left) to high (bottom right) magnification images of 8 wt. % MWCNTs in PA 66 showing isolated regions where the MWCNT concentration is much lower than the average, could indicate incomplete mixing in these regions.

5.5 TEM Imaging

Figure 5.15 shows TEM images of a tapered edge of a cryogenically-milled particle of 5 wt. % MWCNT-PA66 composite. Such tapered edges are difficult to find, since only a tiny fraction of the milled particles have edges thin enough to allow transmission of the electron beam.

In Figure 5.15 (a), a single multi-wall CNT appears to be in intimate contact with the PA66 matrix, which is indicative of good adhesive bonding. In contrast, whenever a multi-wall CNT terminates in the field of view, higher density regions indicative of PA 66 crystallization are observed. An example is shown in Figure 5.15 (b), where the dark-contrasting regions represent crystalline PA 66 in an otherwise amorphous matrix. Some evidence has also been found that such crystallization occurs at steps or ledges in the MWCNTs.



(a)

(b)

Figure 5.15: TEM micrographs of (a) multi-wall CNT in intimate contact with amorphous PA 66 matrix, and (b) dark-contrasting regions of higher density crystalline PA 66 in an amorphous matrix.

It appears from the TEM observations that high-shear mixing at a temperature above the melting point of PA 66 results in a reduction of average length of MWCNTs, and the introduction of surface defects, such as ledges in the tubular structure, both of which are active sites for bonding with the polymer matrix, thus initiating crystallization.

5.6 XRD Analysis

Figure 5.16 shows XRD spectra for loosely-agglomerated MWCNT starting powder, cryogenically-milled PA 66 powder, and 1-8 wt. % MWCNT-PA 66 composites. All samples were vacuum dried at 85°C for 24 hours. Test parameters were V=45 kV, I=40 mA, and step size=0.08 arc sec.

The XRD curve for PA 66 shows commonly observed peaks of (002), (100) and (010,110) crystalline forms at $2\theta = 13.7, 20.4$ and 24 , respectively. While, some researchers designated these peaks as α or emergence of α and β crystalline forms, which are most thermodynamically stable at low temperatures [123, 124,125, 126, 127, 128], others argued that thermodynamically meta-stable γ -crystalline form can co-exist with α -crystalline form. In the last case, the peaks are designated as γ (002), α (100) and α (010,110) at $2\theta = 13.7, 20.4$ and 24 , respectively [129, 130, 131, 132]. That is known, the following XRD curves show the disappearance of the γ -crystalline form at 1-5 wt. % MWCNTs, and its reappearance at 6-8 wt. % MWCNTs. This may suggest that introducing MWCNTs promotes the formation of the α -crystalline form, while suppressing the formation of the γ -crystalline form, at least up to 5 wt. %. The reappearance of the γ -crystalline form is can be attributed to incomplete mixing, which contains a considerable amount of non-bonded polymer matrix phase as proposed in Section 5.4.

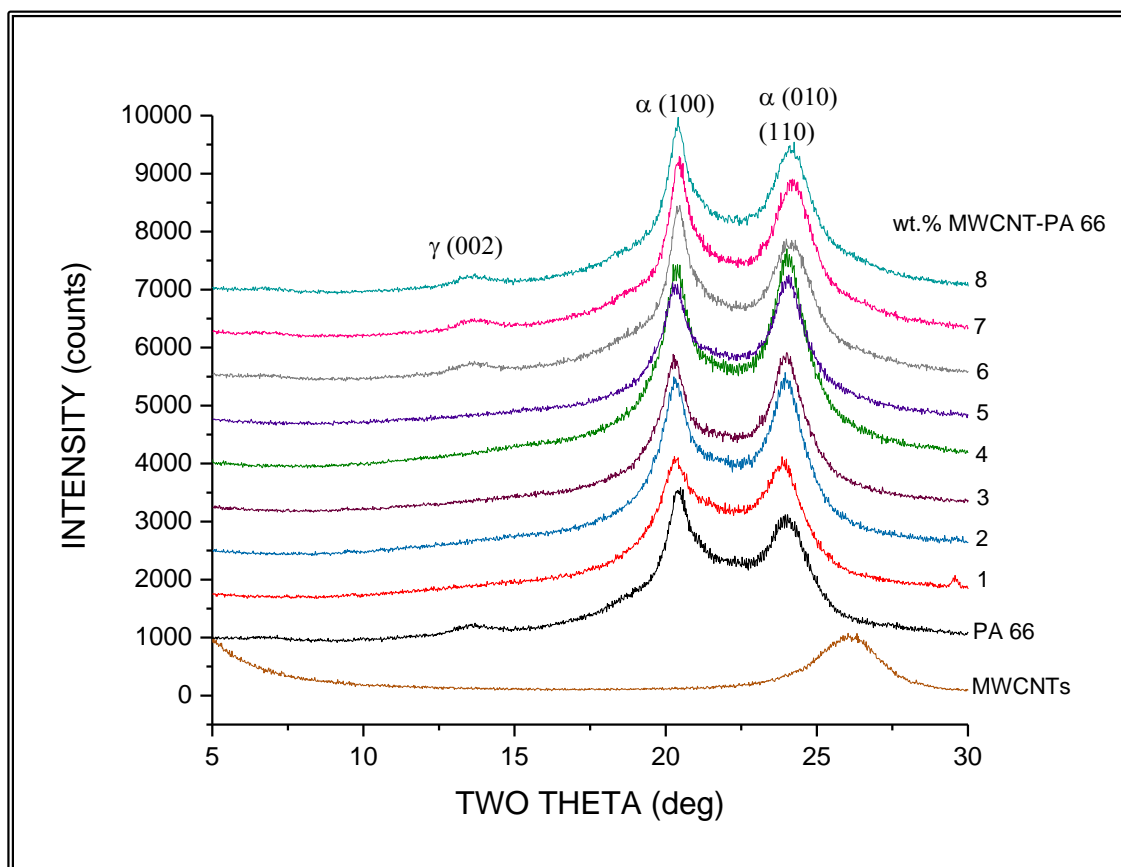


Figure 5.16: XRD curves of MWCNTs, PA 66, and 1-8 wt. % MWCNT-PA 66 composites.

Chapter 6

Post-Fabrication Heat Treatment of GNF-Polymer Composites

6.1 Post-Fabrication Heat Treatment of 35 wt. % GNF-PEEK Composite

During a hiatus in research on MWCNT-PA66 composites, due to equipment breakdown, an investigation was made of the effects of post-fabrication heat treatment on available 35 wt. % graphite exfoliated into graphene nano-flakes (GNFs) in PEEK (35G-PEEK) composite. Significant changes in composite structures were observed, which modified thermal, electrical and mechanical properties. In fact, it now appears that future development of G-PEEK composites, and similar thermoplastic composites, will take advantage of post heat treatment to enhance mechanical properties and performance.

Historically, post-fabrication heat treatment has been used to increase chain length and degree of crystallinity of thermoplastic polymers [20, 21]. For example, when applied to polyethylene, slow cooling from the melt yields a chain-folded crystalline phase consisting of thousands of monomers [22]. In contrast, rapid cooling from the melt yields a fine dispersion of crystalline domains in an amorphous or non-crystalline matrix.

In this research, 35G-PEEK samples were subjected to various heat treatments to establish an optimal processing procedure. This led to the adoption of the following two-step annealing treatment for all experiments: 1) heating the composite at 200°C (above T_g for PEEK – at 150 °C) for up to 20 hr; and 2) further heating of the composite at 380°C (above T_m for PEEK - at 344°C) for up to 18 hr. Under these conditions, little distortion and weight loss of the composite was observed. post-fabrication heat treatment for long times at either temperature gave the largest improvements in stiffness and strength, which has been attributed to the combined effects of planar-adhesive and edge-

covalent bonding between graphene nano-flakes (GNFs) and PEEK matrix, brought about by the high-shear mixing process.

A one-step heat treatment of a 35G-PEEK sample at 380°C (well above T_m) causes gross swelling, due to gasification of the PEEK matrix. As would be expected, decomposition of the PEEK matrix starts at the sample surface and propagates into the sample's interior, thus creating a porous preform of graphene nano-flakes.

Current research is focused on the development of an integrated process, comprising high-shear mixing, injection molding and post-fabrication heat treatment, for the cost-effective fabrication of high performance graphite polymer matrix composites G-PMCs for structural and functional applications.

6.1.1 Influence of Post-Fabrication Heat Treatment

Samples of 35G-PEEK were heat treated at 400-600°C for 20 minutes experienced swelling due to the accumulation of PEEK-decomposition gases within each sample. Most of the swelling occurs in the upper half of a test piece placed vertically in the heat-treatment furnace, apparently due to buoyancy forces. After post-heat treatment at 600°C for 60 minutes, decomposition of the PEEK matrix is essentially complete, leaving behind a porous-graphitic preform that displays some rigidity. The latter is attributed to the presence of some fraction of pyrolyzed PEEK (amorphous carbon) forming bridges between neighboring GNFs. Interestingly; this effect opens opportunities for subsequent infiltration of a porous-graphitic preform with reactive or non-reactive materials.

Using the two-step heat treatment described above avoids sample degradation, thus permitting an investigation of the influence of post- heat treatment on the mechanical properties of 35G-PEEK and 35G-PA66; data for the latter are given in Section 6.2.

6.1.2 Chemical Resistance

Small samples of 35G-PEEK, before and after post heat treatment, are immersed in concentrated sulfuric acid (98%) for 24 hr. As shown in Figure 6.1, the heat-treated sample survives immersion in the acid, whereas the untreated sample does not. In fact, the latter undergoes complete disintegration, forming a fine-scale suspension of GNFs in the acidic solution. This test shows that the two-step annealing treatment introduces effective bonding between neighboring GNFs in the composite, such that upon acid etching to remove the remaining PEEK a moderately rigid porous GNF-based structure is realized. One possible mechanism is the formation of bridges of pyrolyzed carbon between neighboring GNFs in the porous structure, as noted in section 6.1 above.

6.1.3 FESEM Observations

After injection molding of a sample of graphite-PEEK, irrespective of its composition, near-surface alignment or texturing of GNFs occurs. However, in the mid-section of the sample, a spiral-shaped flow pattern is observed, Figure 6.2 (a). Such behavior is to be expected when frictional forces experienced during injection molding dominate, as is the case for a relatively thin sample, e.g. a flat tensile bar. At higher magnification, Figure 6.2 (b), the presence of micro-porosity is revealed, as well as evidence for intimate particle-matrix interaction with possible edge-covalent bonding between GNFs and PEEK matrix.

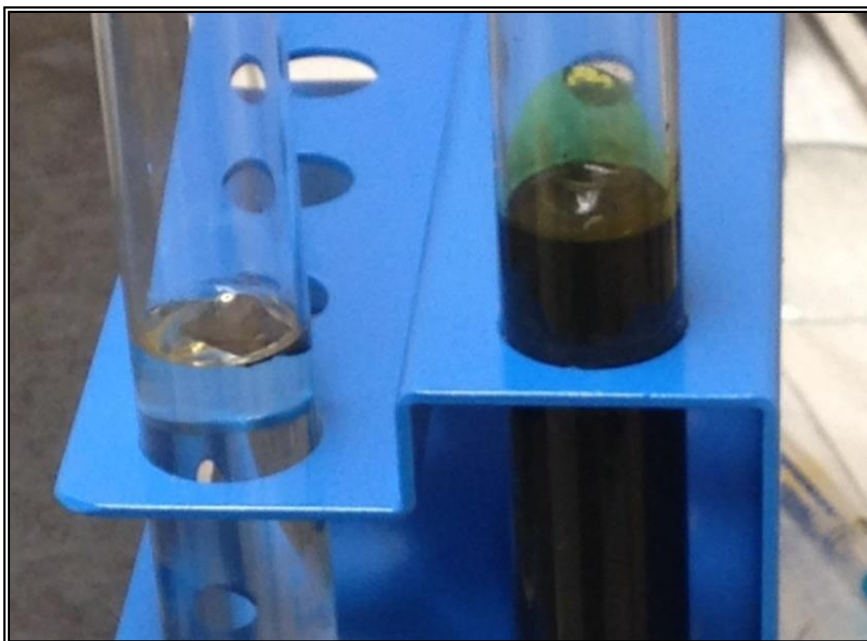
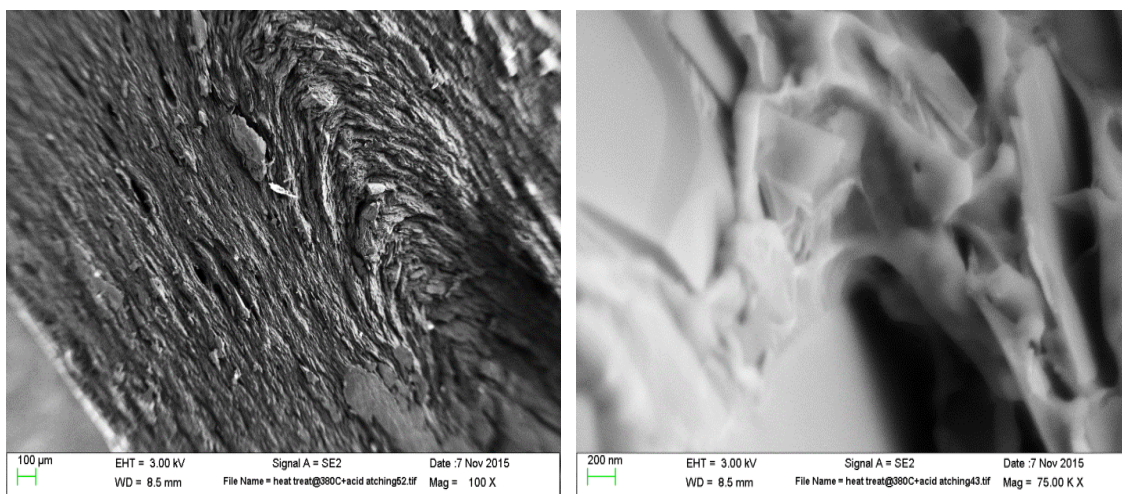


Figure 6.1: Samples of 35G-PEEK after immersion in 98% sulfuric acid for 24 hours: after heat treatment (left), and before heat treatment (right), showing that the post-annealed sample resists chemical attack.



(a)

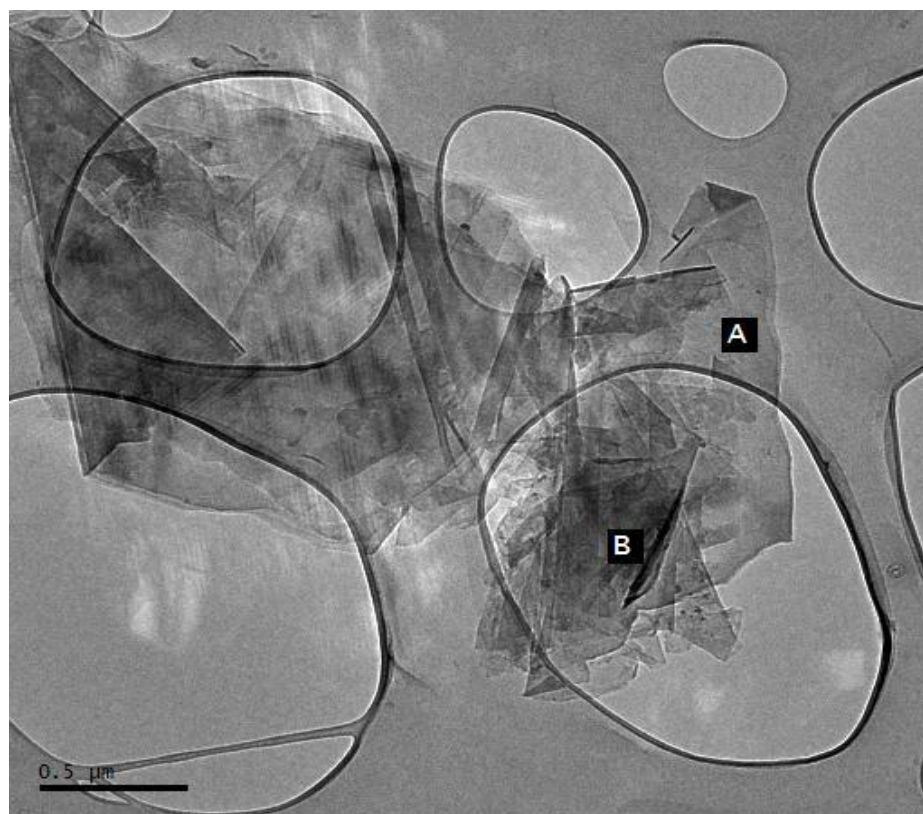
(b)

Figure 6.2: FESEM images of a sample of 35G-PEEK after post annealing, showing (a) textured GNF structure, and (b) evidence for intimate particle-matrix interaction with possible edge-covalent bonding between GNFs and PEEK matrix.

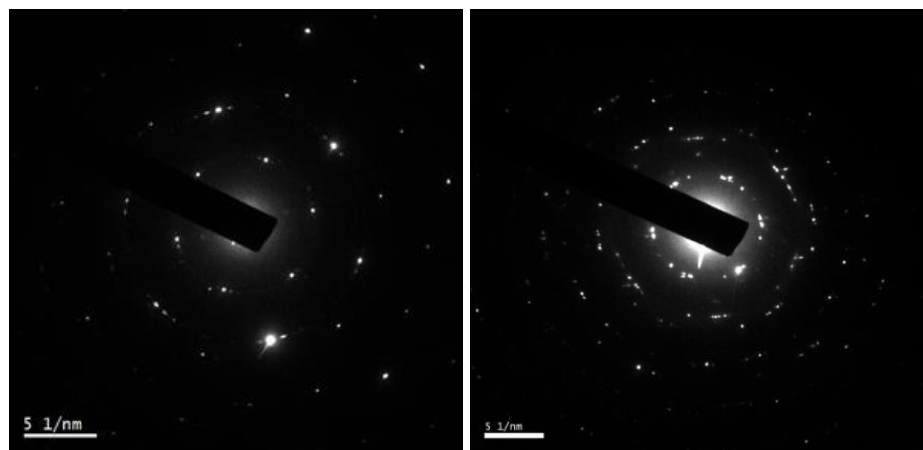
6.1.4 TEM Observations

Graphite - Few-layer graphene flakes, suitable for TEM observations, are prepared by cryogenic milling of graphite powder. Figure 6.3 (a) shows a low-magnification image of graphene flakes supported on a lacy-carbon film. At location A, an isolated flake gives a single-crystal pattern, Figure 6.3 (b), whereas at location B several flakes overlap to give a spotty-ring diffraction pattern, Figure 6.3 (c). Both patterns index as pure graphite, with the isolated flake an example of few-layer graphene.

PEEK - Cryogenically-milling of PEEK pellets is used to prepare fine particles, some of which had very thin tapered edges suitable for direct observations by TEM. Both amorphous and crystalline regions are observed, Figure 6.4, as expected for PEEK.



(a)



(b)

(c)

Figure 6.3: (a) TEM image of few-layer graphene flakes, mostly overlapping, (b) and (c) electron diffraction patterns taken at locations A and B in (a).

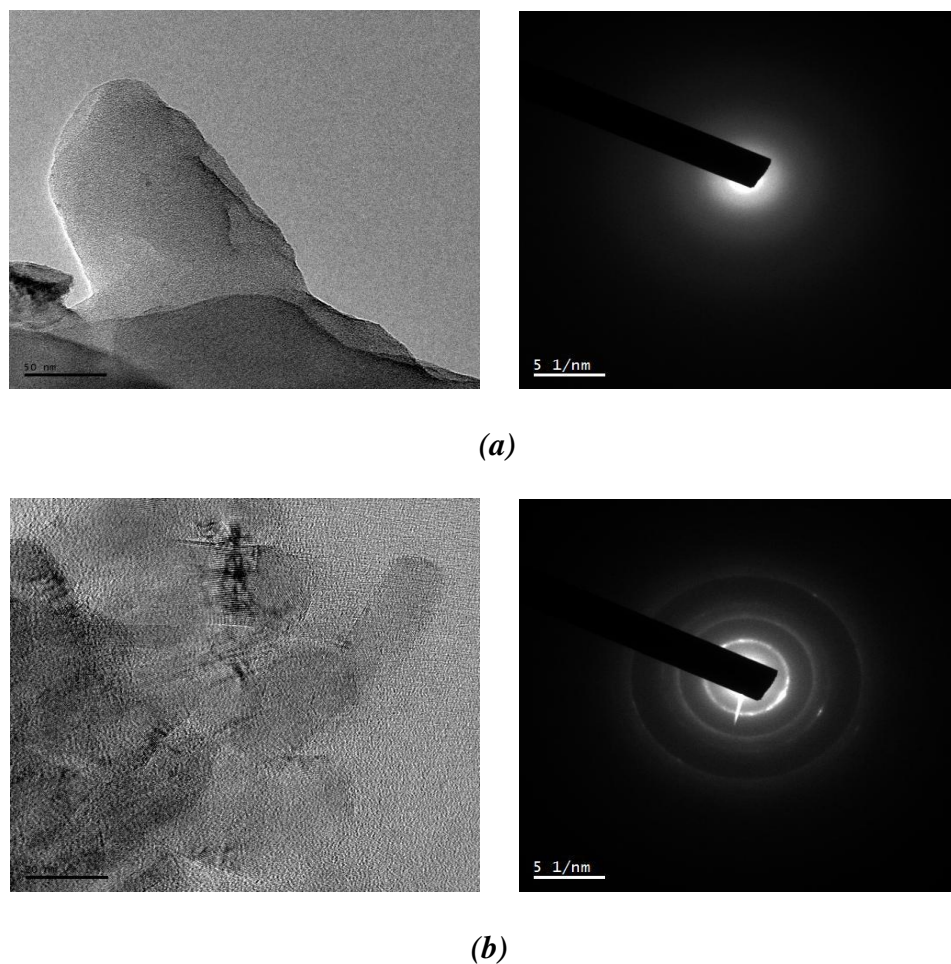


Figure 6.4: TEM images of (a) amorphous PEEK and (b) crystalline PEEK, and their corresponding electron diffraction patterns.

Graphite/PEEK - A typical TEM image of as-processed 35G-PEEK, Figure 6.5, shows that the crystallized component of PEEK tends to form as a thin layer adjacent to the GNFs, whereas the amorphous component of PEEK dominates the rest of the composite. In marked contrast, after post-fabrication annealing, TEM images show that the crystallized form of PEEK starts at the edges of GNFs and expands to occupy most of the polymer composite.

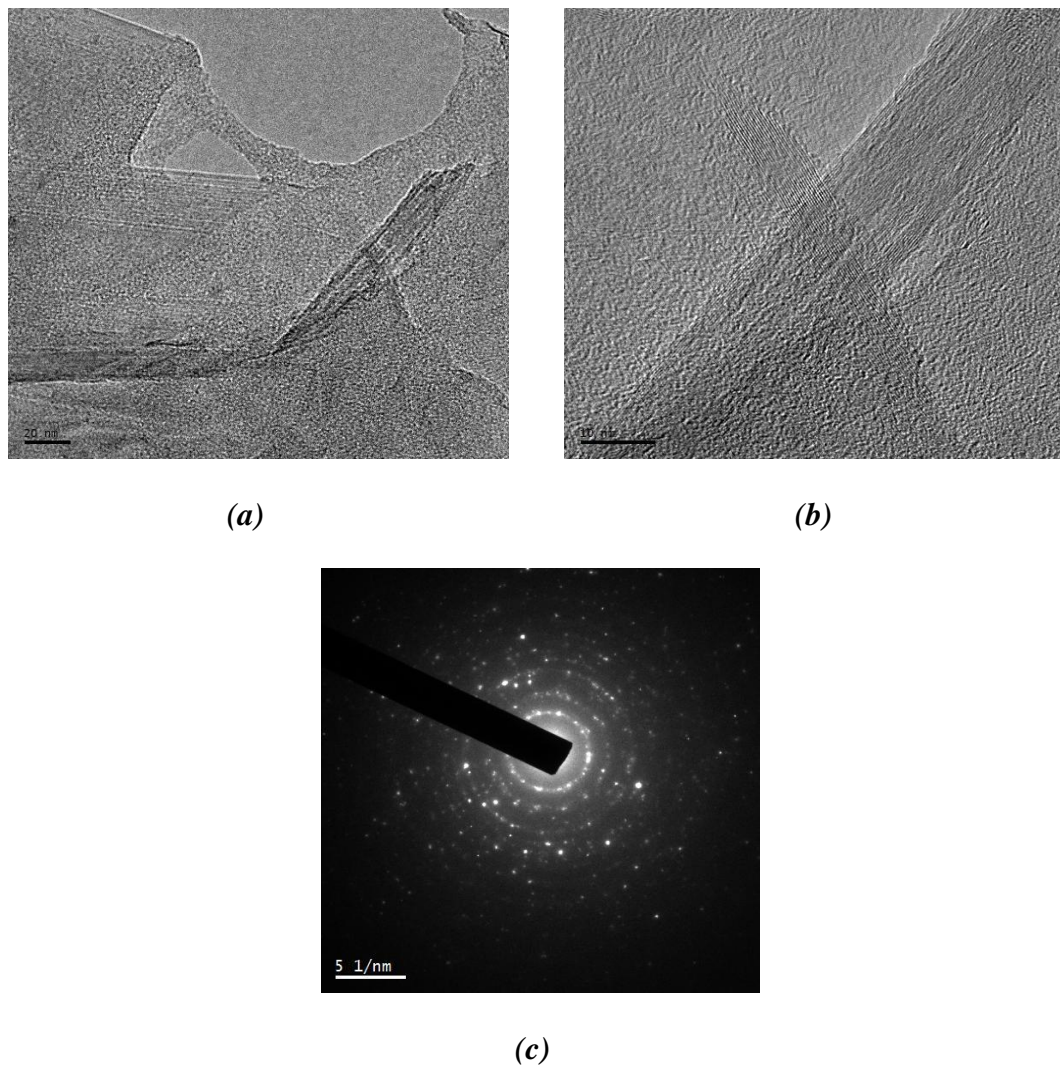


Figure 6.5: TEM image of as-processed 35G-PEEK, showing a graphite flake in (a), which at higher magnification in (b) appears to be decorated with crystalline PEEK and (c) its corresponding electron diffraction pattern.

In contrast, the same material after post-fabrication heat treatment, Figure 6.6, shows extensive crystallization of PEEK, which may be responsible for the increase in stiffness and strength. An unusual feature in these images is what appears to be a layered-graphitic structure. The nature and origin of this layered-composite is not yet understood.

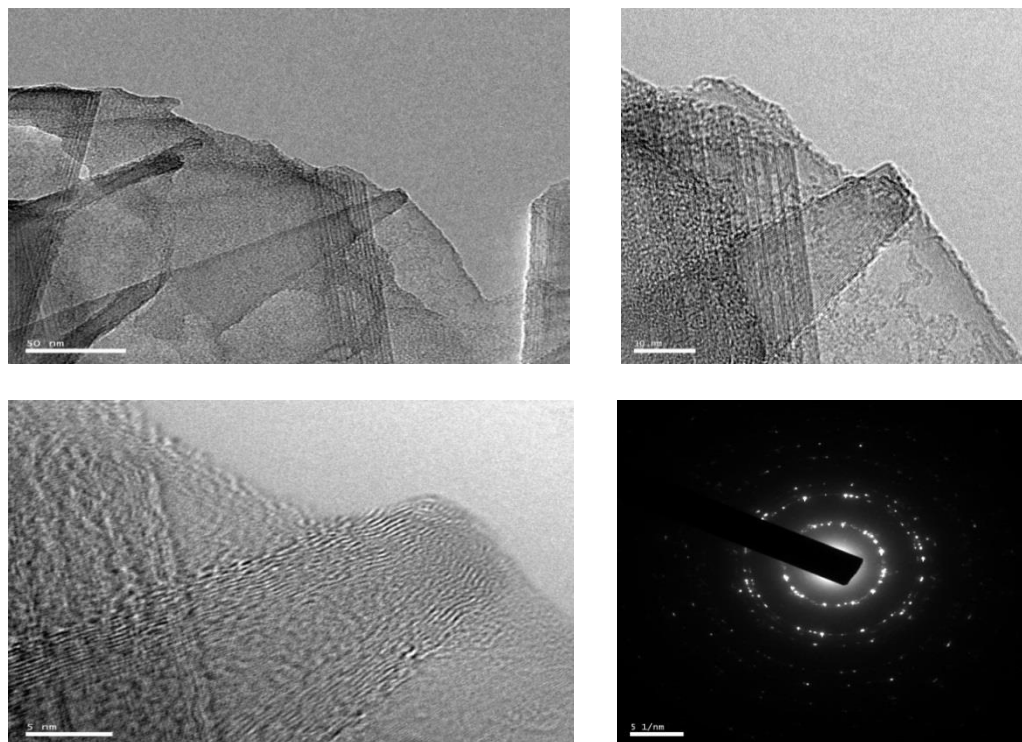


Figure 6.6: TEM images with increasing magnification, showing evidence for crystallization of PEEK as a major phase.

6.1.5 XPS Analysis

Surface scans of PEEK, as-processed 35G-PEEK and heat treated 35G-PEEK are shown in Figure 6.7. The two main peaks, known as (C1s) and (O1s), occur at binding energies of 285 and 533 (eV), respectively. Smaller peaks are ascribed to the Auger effect. Compared to PEEK, peak intensities of (C1s) show increases for both as-processed and heat treated 35G-PEEK, which reflects the graphite content of the composite. In contrast, the intensity of the (O1s) peak is similar for all three samples.

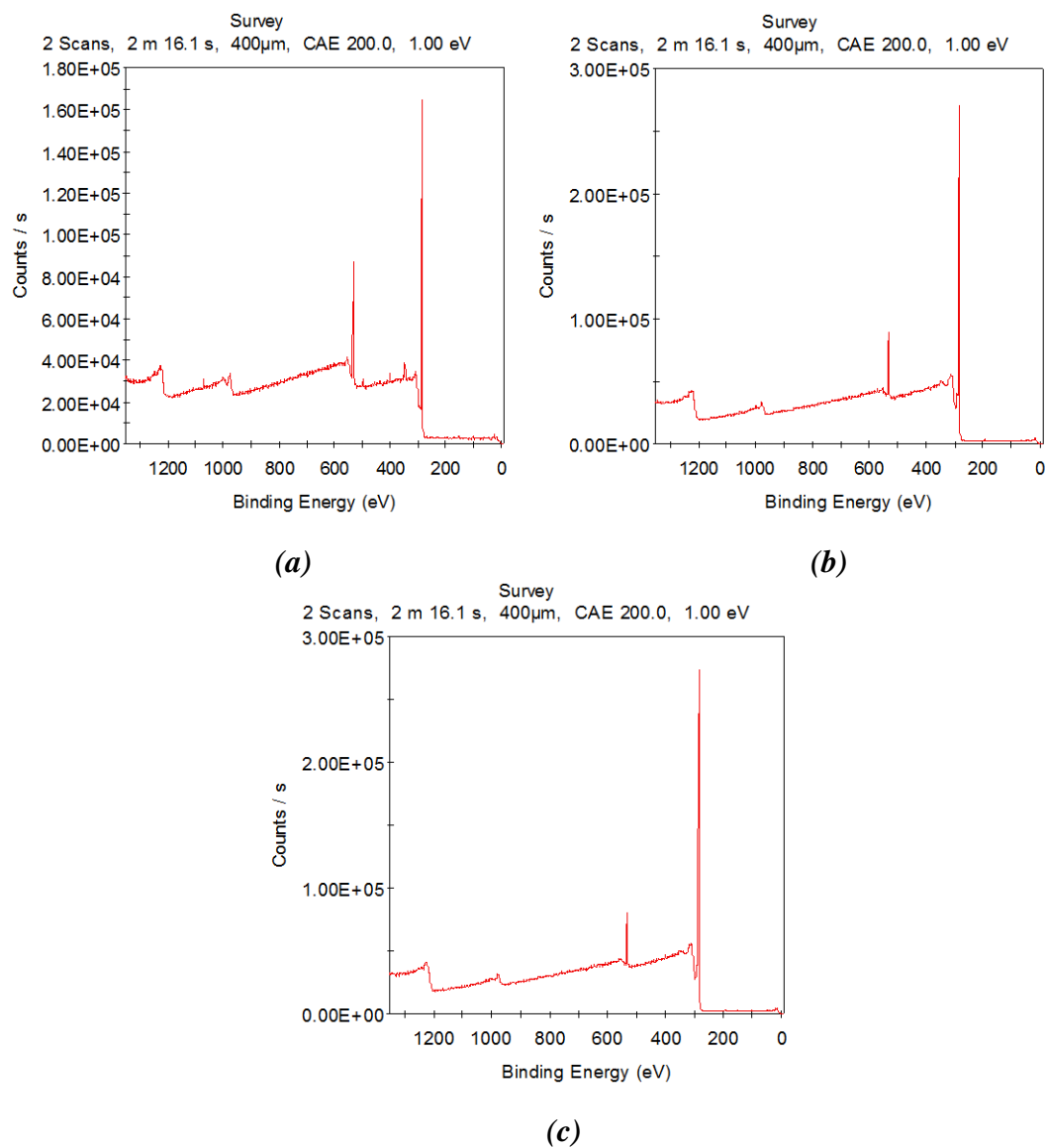


Figure 6.7: XPS scans of (a) PEEK, (b) as-processed 35G-PEEK and (c) heat treated 35G-PEEK.

Figure 6.8 shows splitting of the (C1s) peak into three distinct sub-peaks. The first one is for (C-C) bonding, and represents the backbone-bonding of benzene rings in the PEEK, and occurs at 284.8 (eV). The second one is for (C-O-C) bonding, and represents two of the three bridges between benzene rings, and occurs at 286 (eV). The third one is for a ketone group (C=O), and occurs at 288.3 (eV).

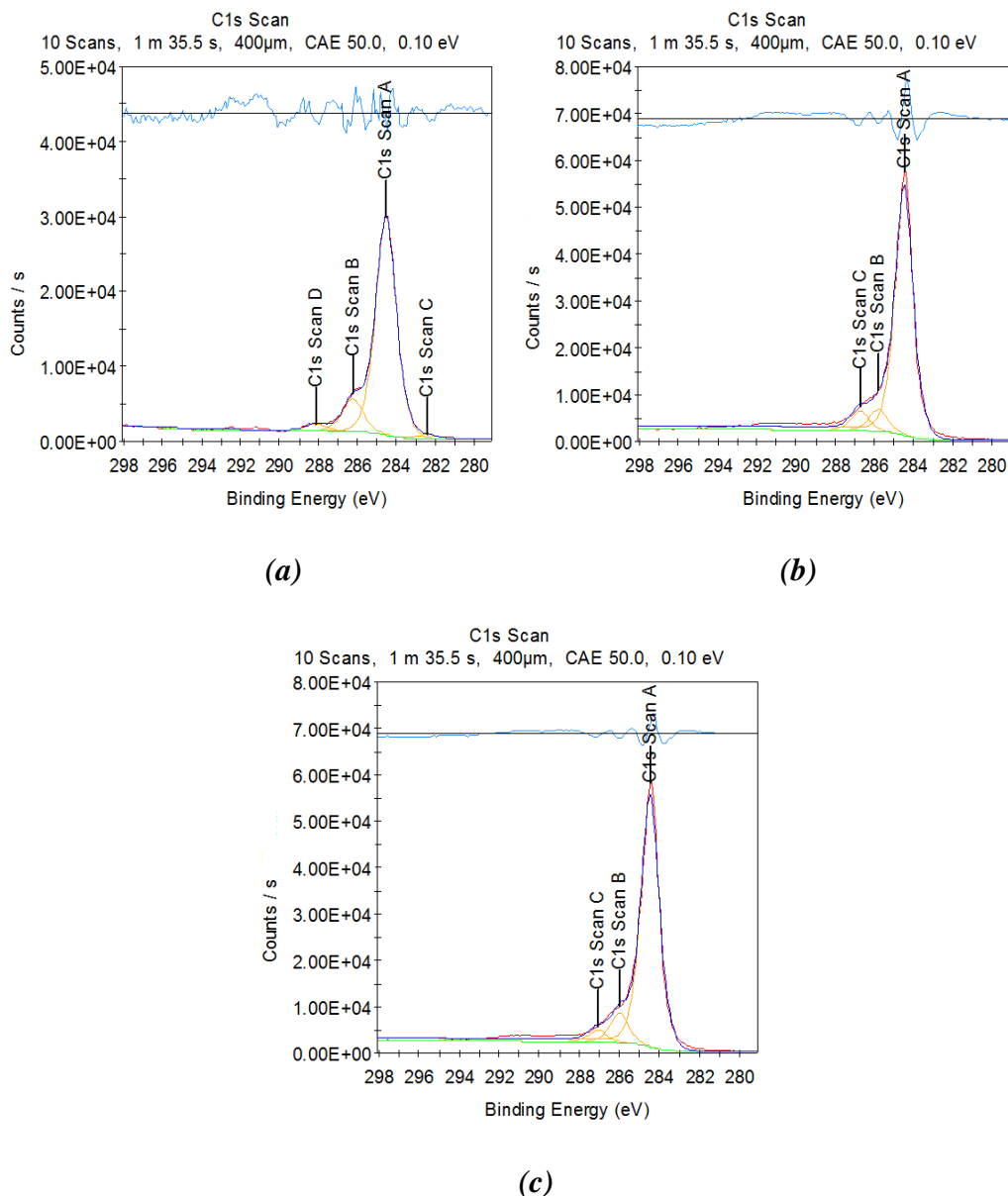


Figure 6.8: XPS (C1s) scans of (a) PEEK, (b) as-processed 35G-PEEK and (c) heat treated 35G-PEEK.

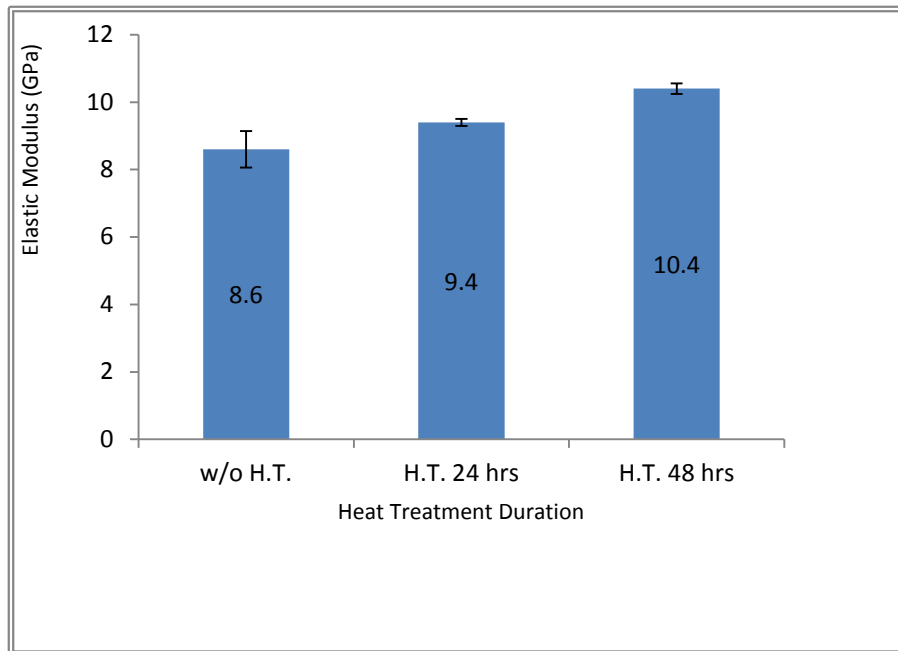
Figure 6.8 shows an increase in intensity of (C-C) bonding, which is attributed to the presence of graphite in the composite. At the same time, Figure 6.8 (b) shows the ketone (C=O) peak shifting towards (C-O-C) region. This behavior suggests that, at the processing temperature, cross-linking of GNFs with PEEK forms new (C-O) bonds, which would explain the increased thermal stability of the composite. Figure 6.8 (c) shows that such polymeric-chain breakages and bonding to graphite continues during heat treatment, which accounts for the progressive increase in thermal stability of the composite.

6.2 Post-Fabrication Heat Treatment of 35G-PA 66 Composite

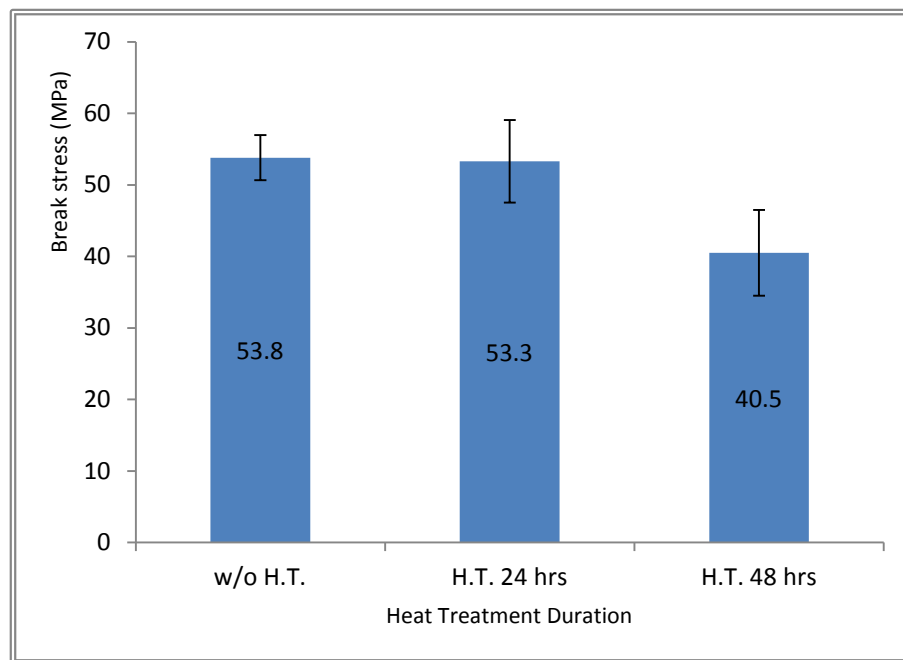
Heat treating 35 wt. % graphite exfoliated into GNFs within PA 66 (35G-PA 66) composite was performed by directly heating the material to 280°C for 24 hours and 48 hours. Heating and cooling rates were set to 5°C/min.

6.2.1 Tensile Properties

Tensile properties of 35G-PA66 before and after heat treatment were determined according to ASTM D 638. Figure 6.9 shows elastic modulus and break stress data of 35G-PA 66 composite, before and after post-heat treatment at 280°C for 24 and 48 hours. The elastic modulus increases and break stress decreases with increasing heat treatment time. The modest increase in elastic modulus is ascribed to crystallization (see below for DSC data) of the PA66 matrix due to interactions with GNFs. Gaining a better understanding of the mechanism involved is the focus of on-going research.



(a)



(b)

Figure 6.9: Elastic modulus and break stress for 35G-PA 66 Composite, without heat treatment and with heat treatment at 280°C for 24 and 48 hours.

6.2.2 DSC Analysis

Figure 6.10 shows first heating (a) – cooling (b) – second heating (c) curves for 35G-PA 66 composite without heat treatment (bottom), with heat treatment at 280°C for 24 hours (middle), and with heat treatment at 280°C for 48 hours (top). The most significant results are as follows:

- 1) Melting, Figure 6.10 (a) occurs over a relatively wide range of temperature, centered at ~260°C;
- 2) Freezing, Figure 6.10 (b), occurs over a much narrower range of temperatures, centered at ~240°C;
- 3) Re-melting, Figure 6.10 (c), occurs at ~260°C.

The melting temperature increases to ~275°C upon heat treatment for 24 and 48 hours. Also, a broad peak occurs at ~260°C.

After heat treatment, the initial melting peak of the composite is reduced to a small peak at ~260°C, and the main peak is shifted to a higher temperature ~275°C. This suggests that heat treatment creates a new crystalline phase of PA 66 with a higher melting point. However, it lacks thermal stability since it is eliminated by re-melting.

From an examination of the peak intensities after heat treatment (44.63 J/g after 24 hours and 19.87 J/g after 48 hours), it is evident that the new phase predominates in the PA 66 matrix after heat treatment for 24 hours, but co-exists with the normal PA 66 matrix after heat treatment for 48 hours. These findings correlate with results obtained by FTIR analysis (see below).

In all three cases, freezing behavior of the PA 66 matrix is similar, but with decreasing peak intensities of 42.39, 41.04 and 37.36 J/g, respectively. This is attributed to a decrease in mass of the polymer matrix due to degradation during heat treatment.

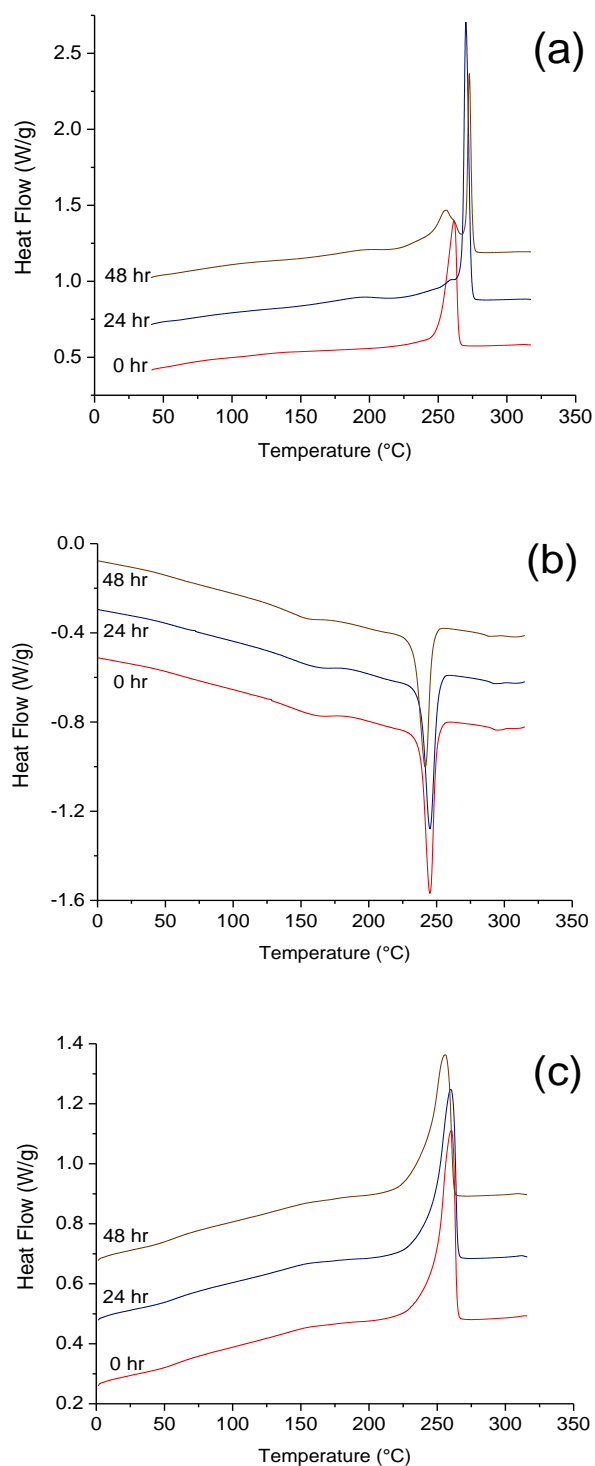


Figure 6.10: Shows (a) first heating - (b) cooling – (c) second heating curves for 35G-PA 66 composite; without heat treatment, with heat treatment at 280°C for 24 hours, and 48 hours.

6.2.3 FTIR Analysis

Figure 6.11 shows FTIR spectra for samples of 35G-PA 66 composite without heat treatment (bottom), after heat treatment at 280°C for 24 hours (middle), and after heat treatment at 280°C for 48 hours (top). The most significant results are as follows:

- 1) Spectra of all three samples show peaks that are characteristic of PA 66, but with different intensities.
- 2) All peaks show a decrease in sharpness/intensity with heat treatment time, attributed to the decrease of PA 66 mass due to degradation.
- 3) Peaks in the 600-1200 wavenumber region, representing C-C bonding, decrease in intensity with heat treatment, which is attributed to the domination of new crystallized phase that caused hindering of bonds stretching.
- 4) A distinctive peak at 936.2 wavenumber, representing C-C stretching, first increases in intensity and then decreases with increasing heat treatment time at 280°C, which suggests the thermally unstable new phase that reaches its highest amount around 24 hours heat treatment then diminishes with further heating duration.

In Section 6.1.4, it was shown that high-shear mixing of well-crystallized graphite particles in molten PEEK creates a uniform dispersion of few-layer graphene nanoflakes (GNFs) in the polymer host, thus providing clean planar surfaces for adhesive bonding and clean fractured edges for covalent bonding. The net effect was to increase elastic modulus dramatically, as well as to enhance impact resistance. The additional DSC and FTIR data presented above provides support for this model, and demonstrates that additional improvements in properties can be realized by post-fabrication heat treatment.

However, much remains to be done to optimize post-fabrication heat treatments to achieve superior mechanical properties and performance for G-PMCs

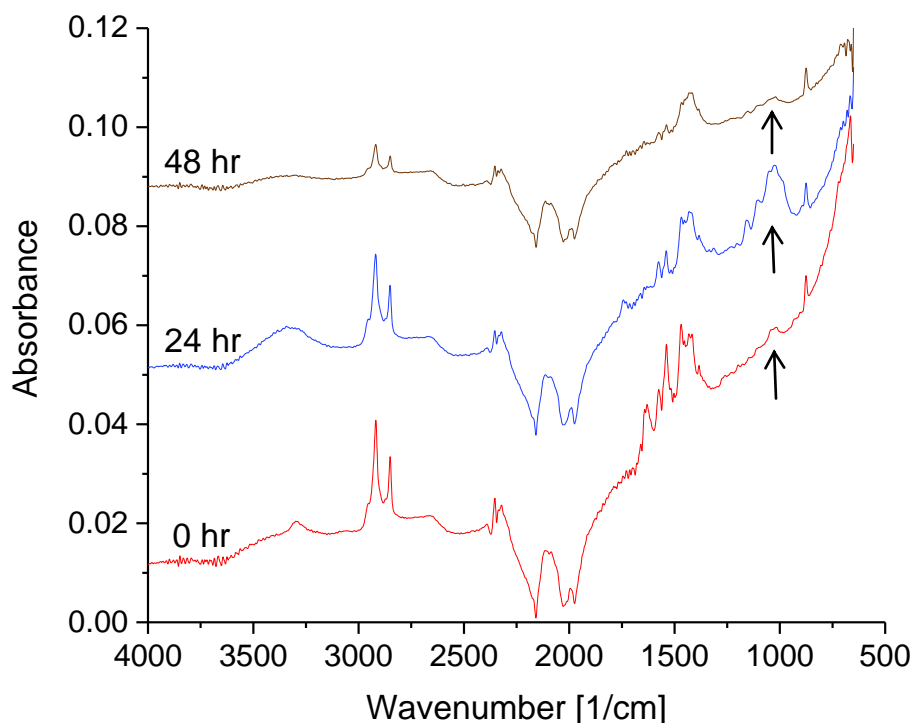


Figure 6.11: FTIR data for 35G-PA 66 composite: (0 hr) without heat treatment, (24 hr) after heat treatment at 280°C for 24 hours and (48 hr) after heat treatment at 280°C for 48 hours curves.

The above results pointing to the fact that heat treatment can be considered as a complementary step toward producing graphite-polymer composites with better mechanical and chemical properties. Achieving that goal requires performing more experiments to discover a suitable heat treatment procedure for each graphite-polymer composition. Finding a suitable heat treatment will involve encouraging bonding between the composite components as well as establishing good thermal and chemical stability all with keeping dimensional changes at minimum.

Chapter 7

Conclusions and Future Work

7.1 Conclusions

In this research, processing, characteristics and properties of MWCNT-PA 66 composites are investigated. Major changes in structural and mechanical properties occur due to the introduction of MWCNTs into the PA 66 matrix. The use of a batch mixer of novel design made it possible to avoid known problems arising from the incorporation of MWCNTs in a polymer matrix, such as incomplete dispersion and agglomeration. High-shear mixing is achieved by using a specially designed batch mixer, which creates active sites for the MWCNTs to bond with the long-chain polymer molecules.

A series of mechanical, thermal and structural tests were conducted on 1-8 wt. % MWCNT in PA 66, prepared by high-shear mixing at a temperature of 277°C, mixing time of 20 minutes, and at 200 RPMs. Structural examinations of the composites showed very good dispersion of the MWCNTs in the PA 66 matrix. It also showed how the MWCNTs interact with the polymer matrix to realize the strong bonding necessary for load transfer from polymer matrix to reinforcing MWCNTs. Thermal measurements conducted on the MWCNT-PA 66 composites indicated that a new crystallization behavior occurred and may be responsible for the reinforcement. Both structural and thermal predictions provided good correlation with mechanical calculations, and explained the major changes in mechanical properties of the composites.

Differential scanning calorimetry (DSC), represented by standard heating-cooling-heating curves, performed over a temperature range 0-350°C, showed the appearance and

growth of a second crystallization peak in the cooling cycle, as the MWCNTs introduced into the PA 66 matrix, increased from 1 to 5 wt. %. This suggests that a new type of crystallization occurs in the matrix, initiated by the MWCNTs, with the amount of the new crystalline phase increasing with increasing MWCNTs until it dominates the structure of the composite at 6, 7 and 8 wt. % MWCNTs in the PA 66 matrix.

The nature of the new crystalline phase was investigated using Fourier transform infrared spectroscopy (FTIR). Close inspection of the spectra showed a steady increase in intensities of all peaks in 1-5 wt. % MWCNT-PA 66 composites, until at 6 wt. % there is a sudden decrease in Amide I and Amide II stretching-peak intensities, accompanied by a shift to lower wave numbers. This behavior is attributed to matrix shift from its original structure to a new C-C rich bonded crystalline state, which is believed to occur primarily at fractured ends of the MWCNTs.

Three-point flexural testing was conducted at a cross-head speed of 5 mm/min and maximum strain of 0.055 mm/mm on PA 66 and its composites. The results showed a gradual increase in modulus as the amount of MWCNTs increased which may be attributed to repeated fracturing of MWCNTs took place during mixing and provided sites for the molten polymer to covalently bond to the fractured ends of the MWCNTs. In addition, a bridging effect of MWCNTs between edge-covalently bonded regions is believed to contribute to the increase in modulus after 3 wt. % MWCNTs in PA 66. The yield stress shows a decreasing trend with increasing MWCNT concentration that could be due to the embrittlement effect of introducing MWCNTs.

Izod impact resistance tests were performed using pendulum device. An initial decrease in impact resistance occurred as MWCNTs were introduced into the molten PA

66, which can be ascribed to dominant stress raiser activity due to inclusion of MWCNTs. A subsequent increase in impact resistance was accredited to the reduction in average length of the MWCNTs. Repeated fracture of MWCNTs formed dangling orbitals at their ends, which most likely bonded covalently to the weakest links (e.g. oxygen bonds) in the long-chain molecules of PA 66. This bonding led in turn to a bridging effect that becomes the dominant reinforcing mechanism. A decrease in impact resistance at high MWCNT additions suggests that the increase in covalent bonding throughout the matrix eventually forms a fully cross-linked like stiff structure of low impact resistance also the appearance of incomplete mixing regions at high MWCNT additions.

Cryogenically fractured surfaces of the composites were examined by FESEM. Low magnification images showed wave-like patterns of micro-cracks on the fracture surface and good dispersion of MWCNTs throughout the PA 66 matrix. Higher magnification images of low wt. % compositions revealed pull-out of many of the fibers, indicating weak fiber/matrix interfaces. Such behavior is expected due to the absence of a significant reduction in lengths of MWCNTs that leads to covalent bonding at their ends. Higher magnification imaging of 7 and 8 wt. % compositions revealed isolated regions of incomplete mixing, indicating that complete mixing is achievable up to about 6 wt. %, at least using the current mixing parameter (20 minutes, 277°C and 200 rpm). TEM imaging of a 5 wt. % composition showed evidence for fracturing of MWCNTs during high-shear mixing and indications of fiber/matrix bonding.

X-ray diffraction (XRD) scans were performed on PA 66, MWCNTs and 1-8 wt. % MWCNT-PA 66 composites. The XRD curve of PA 66 showed peaks of γ (002), α (100)

and α (010,110) crystalline forms at $2\theta = 13.7, 20.4$ and 24 respectively. XRD scans of the composites showed the disappearance of the γ -crystalline form at 1-5 wt. %, and its reappearance at 6-8 wt. %. This suggests that introducing MWCNTs promotes the formation of the α -crystalline form, while suppressing the γ -crystalline form, at least up to 5 wt. %. The reappearance of the γ -crystalline form is attributed to incomplete mixing, which contains a considerable amount of non-bonded polymer matrix phase.

Heat treatment experiments were carried out initially on GNF-PEEK composites, and later on GNF-PA 66 composites. A series of tests performed on 35 wt. % GNF-PEEK showed that a two-step heat treatment gave good dimensional stability. It involved heating the composite to 200°C for 20 hours at a heating rate of $5^{\circ}\text{C}/\text{min}$, and then reheating from 200°C to 380°C for 18 hours at the same heating rate. A small weight loss (1-2 wt. %) was recorded for heat treated composite, which was attributed to minimal decomposition and gasification of the polymer matrix. This was verified through FESEM imaging of a fractured surface, which showed the presence of micro-porosity. Examination of the samples by DSC and FTIR showed that a well-crystallized new phase, with higher melting point, was created by the two-step heat treatment. Similar results have been obtained for GNF-PA 66 composites, but more work is needed to clarify the mechanisms involved.

7.2 Recommendations for Future Work

- 1) Investigate the effects of various time-temperature-shear rate combinations on the properties of the resulting MWCNT-PA 66 composites.
- 2) Find the limits on high-shear mixing that yield a uniform dispersion of MWCNTs in the polymer matrix, for each of these combinations.
- 3) Explore the use of immiscible polymer blends to mitigate some limitations, such as high stiffness at high MWCNTs additions.
- 4) Investigate thermal, electrical and magnetic properties of MWCNT-polymer composites produced by high-shear mixing.
- 5) Investigate the effects of post-fabrication heat treatments on the properties of MWCNT-polymer composites, produced by high-shear mixing.
- 6) Determine the high-shear mixing of single- and double-wall CNT-polymer composites.
- 7) Determine the % crystallinity in the MWCNT composites from the thermal data produced using the DSC.
- 8) Perform DSC thermal scans at various heating/cooling rates to confirm the presence of two crystalline phases in the MWCNT-PA66 composites
- 9) Introduce other reinforcing materials such as GNFs into MWCNT-polymer composites and study interaction possibilities such as intercalation.
- 10) Investigate heat treating other GNF-PEEK and GNF-PA 66 composites.
- 11) Investigate the effects of heat treatment on thermal, electrical and magnetic properties of MWCNT-polymer and GNF-polymer composites.

12) Determine the effects of changing time, temperature, heating-cooling rates, and multi-step heat treatments on structure and properties of the resulting composites.

References

- [1] Bacon, Roger. "Growth, structure, and properties of graphite whiskers." *Journal of Applied Physics* 31, no. 2 (1960): 283-290.
- [2] Dresselhaus, Mildred S., Gene Dresselhaus, Ko Sugihara, Ian L. Spain, and Harris A. Goldberg. *Graphite fibers and filaments*. Vol. 5. Springer Science & Business Media, 2013.
- [3] Endo, M. "The growth mechanism of vapor-grown carbon fibers." PhD diss., Ph. D. thesis, University of Orleans, Orleans, France, 1975.
- [4] Oberlin, A., M. Endo, and T. Koyama. "High resolution electron microscope observations of graphitized carbon fibers." *Carbon* 14, no. 2 (1976): 133-135.
- [5] Oberlin, Agnes, M. Endo, and T. Koyama. "Filamentous growth of carbon through benzene decomposition." *Journal of crystal growth* 32, no. 3 (1976): 335-349.
- [6] Kroto, Harold W., James R. Heath, Sean C. O'Brien, Robert F. Curl, and Richard E. Smalley. "C 60: buckminsterfullerene." *Nature* 318, no. 6042 (1985): 162-163.
- [7] Saito, Riichiro, Gene Dresselhaus, and Mildred S. Dresselhaus. *Physical properties of carbon nanotubes*. Vol. 35. London: Imperial college press, 1998.
- [8] Iijima S. "Helical microtubules of graphitic carbon." *nature* 354, no. 6348 (1991): 56-58.
- [9] Wang, Wenjie, and N. Sanjeeva Murthy. *Characterization of Nanotube-Reinforced Polymer Composites*. INTECH Open Access Publisher, 2011.
- [10] Wei, B. Q., R. Vajtai, and P. M. Ajayan. "Reliability and current carrying capacity of carbon nanotubes." *Applied Physics Letters* 79, no. 8 (2001): 1172-1174.
- [11] Dürkop, T., B. M. Kim, and M. S. Fuhrer. "Properties and applications of high-mobility semiconducting nanotubes." *Journal of Physics: Condensed Matter* 16, no. 18 (2004): R553.
- [12] Chen, Guang-Xin, Hun-Sik Kim, Byung Hyun Park, and Jin-San Yoon. "Multi-walled carbon nanotubes reinforced nylon 6 composites." *Polymer* 47, no. 13 (2006): 4760-4767.
- [13] Tasis, Dimitrios, Nikos Tagmatarchis, Alberto Bianco, and Maurizio Prato. "Chemistry of carbon nanotubes." *Chemical reviews* 106, no. 3 (2006): 1105-1136.
- [14] Spitalsky, Zdenko, Dimitrios Tasis, Konstantinos Papagelis, and Costas Galiotis. "Carbon nanotube–polymer composites: chemistry, processing, mechanical and electrical properties." *Progress in polymer science* 35, no. 3 (2010): 357-401.

- [15] Cao, Liang, Wuli Yang, Junwei Yang, Changchun Wang, and Shoukuan Fu. "Hyperbranched poly (amidoamine)-modified multi-walled carbon nanotubes via grafting-from method." *Chemistry Letters* 33, no. 5 (2004): 490-491.
- [16] Liu, Zhimin, Xinhua Dai, Jian Xu, Buxing Han, Jianling Zhang, Yong Wang, Ying Huang, and Guanying Yang. "Encapsulation of polystyrene within carbon nanotubes with the aid of supercritical CO₂." *Carbon* 42, no. 2 (2004): 458-460.
- [17] Calvert, Paul. "Nanotube composites: a recipe for strength." *Nature* 399, no. 6733 (1999): 210-211.
- [18] Fu, Shao-Yun, Zhen-Kun Chen, Song Hong, and Charles C. Han. "The reduction of carbon nanotube (CNT) length during the manufacture of CNT/polymer composites and a method to simultaneously determine the resulting CNT and interfacial strengths." *Carbon* 47, no. 14 (2009): 3192-3200.
- [19] Kymakis, E., E. Koudoumas, I. Franghiadakis, and G. A. J. Amaratunga. "Post-fabrication annealing effects in polymer-nanotube photovoltaic cells." *Journal of Physics D: Applied Physics* 39, no. 6 (2006): 1058.
- [20] Yu, Xuan, Xiao-ming Yu, Zi-yang Hu, Jian-jun Zhang, Gengshen Zhao, and Ying Zhao. "Efficiency enhancement of polymer solar cells by post-additional annealing treatment." *Optoelectronics Letters* 9 (2013): 274-277.
- [21] Chen, Ziyu, M. J. Jenkins, and J. N. Hay. "Annealing of poly (ethylene terephthalate)." *European Polymer Journal* 50 (2014): 235-242.
- [22] Peterlin, A. "Crystallization and annealing of polyethylene." *Die Makromolekulare Chemie* 74, no. 1 (1964): 107-128.
- [23] Biddlestone, F., A. Harris, J. N. Hay, and T. Hammond. "The physical ageing of amorphous poly (hydroxybutyrate)." *Polymer international* 39, no. 3 (1996): 221-229.
- [24] Chen, Ziyu, J. N. Hay, and M. J. Jenkins. "FTIR spectroscopic analysis of poly (ethylene terephthalate) on crystallization." *European Polymer Journal* 48, no. 9 (2012): 1586-1610.
- [25] Fischer, E. W. "Effect of annealing and temperature on the morphological structure of polymers." *Pure and applied chemistry* 31, no. 1-2 (1972): 113-132.
- [26] Lorenzo, Arnaldo T., María L. Arnal, Johan J. Sánchez, and Alejandro J. Müller. "Effect of annealing time on the self-nucleation behavior of semicrystalline polymers." *Journal of Polymer Science Part B: Polymer Physics* 44, no. 12 (2006): 1738-1750.
- [27] Rastogi, Sanjay, A. B. Spoelstra, J. G. P. Goossens, and P. J. Lemstra. "Chain mobility in polymer systems: on the borderline between solid and melt. 1. Lamellar doubling during annealing of polyethylene." *Macromolecules* 30, no. 25 (1997): 7880-7889.

- [28] Mandelkern, L., R. K. Sharma, and J. F. Jackson. "On the annealing of polyethylene crystals formed from dilute solution." *Macromolecules* 2, no. 6 (1969): 644-647.
- [29] Ayman, A. A., E. B. Zeidan, A. M. Hamed, and W. Y. Ali. "Effect of heat treatment on the abrasion resistance of thermoplastic polymers." *EGTRIB Journal of the Egyptian Society of Tribology* 7, no. 4 (2010): 52-64.
- [30] Crist, B. "Semicrystalline Polymers: Plastic Deformation." *Encyclopedia of Materials: Science and Technology*, Oxford, Elsevier (2001).
- [31] Lee, B. J., A. S. Argon, D. M. Parks, Said Ahzi, and Z. Bartczak. "Simulation of large strain plastic deformation and texture evolution in high density polyethylene." *Polymer* 34, no. 17 (1993): 3555-3575.
- [32] Bellare, A., R. E. Cohen, and A. S. Argon. "Development of texture in poly (ethylene terephthalate) by plane-strain compression." *Polymer* 34, no. 7 (1993): 1393-1403.
- [33] Bartczak, Z., A. S. Argon, and R. E. Cohen. "Texture evolution in large strain simple shear deformation of high density polyethylene." *Polymer* 35, no. 16 (1994): 3427-3441.
- [34] Asano, Tsutomu, Francisco J. Balta Calleja, Araceli Flores, Motonori Tanigaki, Mohammad Forhad Mina, Chie Sawatari, Hideyuki Itagaki, Hiroshi Takahashi, and Ichiro Hatta. "Crystallization of oriented amorphous poly (ethylene terephthalate) as revealed by X-ray diffraction and microhardness." *Polymer* 40, no. 23 (1999): 6475-6484.
- [35] Bedia, Elinor L., Syozo Murakami, Taku Kitade, and Shinzo Kohjiya. "Structural development and mechanical properties of polyethylene naphthalate/polyethylene terephthalate blends during uniaxial drawing." *Polymer* 42, no. 17 (2001): 7299-7305.
- [36] Göschel, U., K. Deutscher, and V. Abetz. "Wide-angle X-ray scattering studies using an area detector: crystallite orientation in semicrystalline PET structures." *Polymer* 37, no. 1 (1996): 1-6.
- [37] Ishikawa, M., and I. Narisawa. "The effect of heat treatment on plane strain fracture of glassy polymers." *Journal of Materials Science* 18, no. 9 (1983): 2826-2834.
- [38] Panda, Jitendra Narayan, Jayashree Bijwe, and Raj K. Pandey. "Role of treatment to graphite particles to increase the thermal conductivity in controlling tribo-performance of polymer composites." *Wear* 360 (2016): 87-96.
- [39] Sheppard, R. G., D. M. Mathes, and D. J. Bray. "Properties and characteristics of graphite." *Poco Graphite, Inc* (2001).
- [40] Balandin, Alexander A. "Thermal properties of graphene and nanostructured carbon materials." *Nature materials* 10, no. 8 (2011): 569-581.

- [41] Radushkevich, L.V. and Luk'yanovich, V.M., Zh. Fiz.Khim., 1952, vol. 26, pp. 88–95.
- [42] Oberlin, Agnes, M. Endo, and T. Koyama. "Filamentous growth of carbon through benzene decomposition." *Journal of crystal growth* 32, no. 3 (1976): 335-349.
- [43] Iijima S. "Helical microtubules of graphitic carbon." *nature* 354, no. 6348 (1991): 56-58.
- [44] Iijima, Sumio, and Toshinari Ichihashi. "Single-shell carbon nanotubes of 1-nm diameter." (1993): 603-605.
- [45] Bethune, D. S., C. H. Klang, M. S. De Vries, G. Gorman, R. Savoy, J. Vazquez, and R. Beyers. "Cobalt-catalyzed growth of carbon nanotubes with single-atomic-layer walls." (1993): 605-607.
- [46] Dravid, V. P., X. Lin, Y. Wang, X. K. Wang, A. Yee, J. B. Ketterson, and R. P. H. Chang. "Buckytubes and derivatives: their growth and implications for buckyball formation." *Science* 259, no. 5101 (1993): 1601-1604.
- [47] Ge, Maohui, and Klaus Sattler. "Vapor-condensation generation and STM analysis of fullerene tubes." *Physics & Chemistry of Fullerenes: A Reprint Collection* 1 (1993): 226.
- [48] Zhou, O., R. M. Fleming, D. W. Murphy, C. H. Chen, R. C. Haddon, A. P. Ramirez, and S. H. Glarum. "Defects in carbon nanostructures." *Science* 263, no. 5154 (1994): 1744-1747.
- [49] Ajayan, Pulickel M., and Otto Z. Zhou. "Applications of carbon nanotubes." In *Carbon nanotubes*, pp. 391-425. Springer Berlin Heidelberg, 2001.
- [50] Ebbesen, Thomas W. "Carbon nanotubes." *Annual review of materials science* 24, no. 1 (1994): 235-264.
- [51] Paradise, Melissa, and Tarun Goswami. "Carbon nanotubes—production and industrial applications." *Materials & Design* 28, no. 5 (2007): 1477-1489.
- [52] Wang, X. K., X. W. Lin, V. P. Dravid, J. B. Ketterson, and Robert PH Chang. "Carbon nanotubes synthesized in a hydrogen arc discharge." *Applied Physics Letters* 66, no. 18 (1995): 2430-2432.
- [53] Zhang, Y., H. Gu, and S. Iijima. "Single-wall carbon nanotubes synthesized by laser ablation in a nitrogen atmosphere." *Applied physics letters* 73, no. 26 (1998): 3827-3829.
- [54] Che, G., B. B. Lakshmi, C. R. Martin, E. R. Fisher, and Rodney S. Ruoff. "Chemical vapor deposition based synthesis of carbon nanotubes and nanofibers using a template method." *Chemistry of Materials* 10, no. 1 (1998): 260-267.

- [55] Prasek, Jan, Jana Drbohlavova, Jana Chomoucka, Jaromir Hubalek, Ondrej Jasek, Vojtech Adam, and Rene Kizek. "Methods for carbon nanotubes synthesis—review." *Journal of Materials Chemistry* 21, no. 40 (2011): 15872-15884.
- [56] He, Z. B., Jean-Luc Maurice, C. S. Lee, C. S. Cojocaru, and D. Pribat. "Nickel catalyst faceting in plasma-enhanced direct current chemical vapor deposition of carbon nanofibers." *The Arabian Journal for Science and Engineering* 35, no. 1C (2010): 19.
- [57] Kunadian, Illayathambi, Rodney Andrews, Dali Qian, and M. Pinar Mengüç. "Growth kinetics of MWCNTs synthesized by a continuous-feed CVD method." *Carbon* 47, no. 2 (2009): 384-395.
- [58] Sandler, J. K. W., J. E. Kirk, I. A. Kinloch, M. S. P. Shaffer, and A. H. Windle. "Ultra-low electrical percolation threshold in carbon-nanotube-epoxy composites." *Polymer* 44, no. 19 (2003): 5893-5899.
- [59] Biercuk, M. J., Mark C. Llaguno, M. Radosavljevic, J. K. Hyun, Alan T. Johnson, and John E. Fischer. "Carbon nanotube composites for thermal management." *Applied physics letters* 80, no. 15 (2002): 2767-2769.
- [60] Thostenson, Erik T., and Tsu-Wei Chou. "On the elastic properties of carbon nanotube-based composites: modelling and characterization." *Journal of Physics D: Applied Physics* 36, no. 5 (2003): 573.
- [61] Odegard, G. M., T. S. Gates, K. E. Wise, C. Park, and E. J. Siochi. "Constitutive modeling of nanotube-reinforced polymer composites." *Composites science and technology* 63, no. 11 (2003): 1671-1687.
- [62] Ko, Frank, Yury Gogotsi, Ashraf Ali, Nevin Naguib, Haihui Ye, G. L. Yang, Christopher Li, and Peter Willis. "Electrospinning of continuous carbon nanotube-filled nanofiber yarns." *Advanced materials* 15, no. 14 (2003): 1161-1165.
- [63] Andrews, R., and M. C. Weisenberger. "Carbon nanotube polymer composites." *Current Opinion in Solid State and Materials Science* 8, no. 1 (2004): 31-37.
- [64] in het Panhuis, Marc, Amitesh Maiti, Alan B. Dalton, Albert van den Noort, Jonathan N. Coleman, Brendan McCarthy, and Werner J. Blau. "Selective interaction in a polymer-single-wall carbon nanotube composite." *The Journal of Physical Chemistry B* 107, no. 2 (2003): 478-482.
- [65] Liu, Tianxi, In Yee Phang, Lu Shen, Shue Yin Chow, and Wei-De Zhang. "Morphology and mechanical properties of multiwalled carbon nanotubes reinforced nylon-6 composites." *Macromolecules* 37, no. 19 (2004): 7214-7222.
- [66] Miaudet, P., S. Badaire, M. Maugey, A. Derre, V. Pichot, P. Launois, P. Poulin, and C. Zakri. "Hot-drawing of single and multiwall carbon nanotube fibers for high toughness and alignment." *Nano letters* 5, no. 11 (2005): 2212-2215.

- [67] Kozlov, Mikhail E., Ryan C. Capps, William M. Sampson, Von Howard Ebron, John P. Ferraris, and Ray H. Baughman. "Spinning Solid and Hollow Polymer-Free Carbon Nanotube Fibers." *Advanced Materials* 17, no. 5 (2005): 614-617.
- [68] Nan, Ce-Wen, Gang Liu, Yuanhua Lin, and Ming Li. "Interface effect on thermal conductivity of carbon nanotube composites." *Applied Physics Letters* 85, no. 16 (2004): 3549-3551.
- [69] Srivastava, Deepak, Chenyu Wei, and Kyeongjae Cho. "Nanomechanics of carbon nanotubes and composites." *Applied Mechanics Reviews* 56, no. 2 (2003): 215-230.
- [70] Wang, W., P. Ciselli, E. Kuznetsov, T. Peijs, and A. H. Barber. "Effective reinforcement in carbon nanotube-polymer composites." *Philosophical Transactions of the Royal Society of London A: Mathematical, Physical and Engineering Sciences* 366, no. 1870 (2008): 1613-1626.
- [71] Chen, Guang-Xin, Hun-Sik Kim, Byung Hyun Park, and Jin-San Yoon. "Multi-walled carbon nanotubes reinforced nylon 6 composites." *Polymer* 47, no. 13 (2006): 4760-4767.
- [72] Li, Lingyu, Christopher Y. Li, Chaoying Ni, Lixia Rong, and Benjamin Hsiao. "Structure and crystallization behavior of Nylon 66/multi-walled carbon nanotube nanocomposites at low carbon nanotube contents." *Polymer* 48, no. 12 (2007): 3452-3460.
- [73] Wang, Xin, Philip D. Bradford, Wei Liu, Haibo Zhao, Yoku Inoue, Jon-Paul Maria, Qingwen Li, Fuh-Gwo Yuan, and Yuntian Zhu. "Mechanical and electrical property improvement in CNT/Nylon composites through drawing and stretching." *Composites Science and Technology* 71, no. 14 (2011): 1677-1683.
- [74] Saeed, Khalid, and Soo-Young Park. "Preparation of multiwalled carbon nanotube/nylon-6 nanocomposites by in situ polymerization." *Journal of applied polymer science* 106, no. 6 (2007): 3729-3735.
- [75] Ajayan, Pulickel M., Linda S. Schadler, Cindy Giannaris, and Angel Rubio. "Single-walled carbon nanotube-polymer composites: strength and weakness." *Advanced Materials* 12, no. 10 (2000): 750-753.
- [76] Terrones, Mauricio. "Science and technology of the twenty-first century: synthesis, properties, and applications of carbon nanotubes." *Annual review of materials research* 33, no. 1 (2003): 419-501.
- [77] Barrera, Enrique V. "Key methods for developing single-wall nanotube composites." *JOM* 52, no. 11 (2000): 38-42.
- [78] McCarthy, B., J. N. Coleman, R. Czerw, A. B. Dalton, M. In Het Panhuis, A. Maiti, A. Drury et al. "A microscopic and spectroscopic study of interactions between carbon

nanotubes and a conjugated polymer." *The Journal of Physical Chemistry B* 106, no. 9 (2002): 2210-2216.

[79] Rahaman, Muhammad Syukri Abdul, Ahmad Fauzi Ismail, and Azeman Mustafa. "A review of heat treatment on polyacrylonitrile fiber." *Polymer Degradation and Stability* 92, no. 8 (2007): 1421-1432.

[80] Sutasinpromprae, Juthawan, Sujinda Jitjaicham, Manit Nithitanakul, Chidchanok Meechaisue, and Pitt Supaphol. "Preparation and characterization of ultrafine electrospun polyacrylonitrile fibers and their subsequent pyrolysis to carbon fibers." *Polymer International* 55, no. 8 (2006): 825-833.

[81] Wang, Yu, Santiago Serrano, and Jorge J. Santiago-Aviles. "Raman characterization of carbon nanofibers prepared using electrospinning." *Synthetic Metals* 138, no. 3 (2003): 423-427.

[82] Gu, S. Y., J. Ren, and G. J. Vancso. "Process optimization and empirical modeling for electrospun polyacrylonitrile (PAN) nanofiber precursor of carbon nanofibers." *European polymer journal* 41, no. 11 (2005): 2559-2568.

[83] Wang, Yu, and Jorge J. Santiago-Avilés. "Large negative magnetoresistance and two-dimensional weak localization in carbon nanofiber fabricated using electrospinning." *Journal of applied physics* 94, no. 3 (2003): 1721-1727.

[84] Peterlin, A. "Crystallization and annealing of polyethylene." *Die Makromolekulare Chemie* 74, no. 1 (1964): 107-128.

[85] Bair, H. E., R. Salovey, and T. W. Huseby. "Melting and annealing of polyethylene single crystals." *Polymer* 8 (1967): 9-20.

[86] Gruner, Charles L., Bernhard Wunderlich, and Richard C. Bopp. "Extended-chain crystals. VI. Annealing of polyethylene under elevated pressure." *Journal of Polymer Science Part A-2: Polymer Physics* 7, no. 12 (1969): 2099-2113.

[87] Spells, Stephen J., and Mary J. Hill. "Morphological changes on annealing polyethylene single crystals." *Polymer* 32, no. 15 (1991): 2716-2723.

[88] Rastogi, Sanjay, A. B. Spoelstra, J. G. P. Goossens, and P. J. Lemstra. "Chain mobility in polymer systems: on the borderline between solid and melt. 1. Lamellar doubling during annealing of polyethylene." *Macromolecules* 30, no. 25 (1997): 7880-7889.

[89] Ishikawa, M., and I. Narisawa. "The effect of heat treatment on plane strain fracture of glassy polymers." *Journal of Materials Science* 18, no. 9 (1983): 2826-2834.

[90] Nishi, T., and T. K. Kwei. "Improvement of the impact strength of a blend of poly (vinyl chloride) with copolyester thermoplastic elastomer by heat treatment." *Journal of Applied Polymer Science* 20, no. 5 (1976): 1331-1337.

- [91] Broyer, Ephraim. "Thermal treatment of thermoplastic filaments for the preparation of surgical sutures." U.S. Patent 5,451,461, issued September 19, 1995.
- [92] Tang, Shih Chieh. "Brightness enhancement film." U.S. Patent 6,277,471, issued August 21, 2001.
- [93] "Heat treatment of aromatic sulfide polymers." U.S. Patent 3,699,087, issued October 17, 1972.
- [94] Ferracane, J. L., and J. R. Condon. "Post-cure heat treatments for composites: properties and fractography." *Dental Materials* 8, no. 5 (1992): 290-295.
- [95] Miyazaki, Caroline Lumi, Igor Studart Medeiros, Ivone Lima Santana, Jivaldo do Rosário Matos, and Leonardo Eloy Rodrigues Filho. "Heat treatment of a direct composite resin: influence on flexural strength." *Brazilian oral research* 23, no. 3 (2009): 241-247.
- [96] Alallak, Nidaa. "Effect of Heat Treatment on Tensile Strength, Hardness and Thermal Conductivity of Blended Polymer Composite." In *Materials Science Forum*, vol. 706, pp. 625-630. Trans Tech Publications, 2012.
- [97] Manjunatha, G., S. Rajesh, Raji George, and Kumara Naik. "Influence of Post Heat Treatment Temperatures on Wear Properties of MWCNTs Reinforced Epoxy Composites." *American Journal of Materials Science* 5, no. 3C (2015): 183-187.
- [98] Manjunatha, G., Raji George, and A. Manjunath. "A Study of Post Heat Treatment Temperature Variables on Mechanical Properties of Nanopolymer Composites." *American Journal of Materials Science* 5, no. 3C (2015): 116-120.
- [99] Pang, Huan, Yi-Chuan Zhang, Tao Chen, Bao-Qing Zeng, and Zhong-Ming Li. "Tunable positive temperature coefficient of resistivity in an electrically conducting polymer/graphene composite." *Applied Physics Letters* 96, no. 25 (2010): 251907.
- [100] Kumar, Mukul, and Yoshinori Ando. *Carbon nanotube synthesis and growth mechanism*. INTECH Open Access Publisher, 2011.
- [101] Hrachová, Jana, Leon E. Govaert, and Han EH Meijer. "Influence of water absorption on the mechanical properties of Polyamide 6 and Polyamide 4-6." (2010).
- [102] Materials Science and Engineering, Rutgers: (2016). Retrieved from <http://mse.rutgers.edu/laboratoriesfacilitieservices>
- [103] SIGMA scanning electron microscope ZEISS: (2016). Retrieved from http://www.zeiss.com/microscopy/en_de/products/scanning-electron-microscopes/sigma.html
- [104] Stanford Microscopy Facility, Stanford: (2015). Retrieved from <https://microscopy.stanford.edu/sem-zeiss-sigma-fesem-0>

- [105] Swapp, Susan. "Scanning electron microscopy (sem)." *Geochemical Instrumentation and Analysis* (2012).
- [106] Department of Chemistry, Tennessee: (2016). Retrieved from <http://www.chem.utk.edu/facilities/pcl/dsc-a2>
- [107] Particle Analytical: Analyses for the Pharmaceutical Industry: (2016). Retrieved from <http://particle.dk/methods-analytical-laboratory/dsc-differential-scanning-calorimetry-2/dsc-theory/>
- [108] TA Instruments Rheometers: (2016). Retrieved from <http://tainstruments.com/pdf/literature/ar2000brochure.pdf>
- [109] Murata, Hiroshi. "Rheology–Theory and Application to Biomaterials." *Janeza Trdine* 9, no. 51000 (2012): 403-426.
- [110] Nielsen LE, Landel RF. "Mechanical Properties of Polymers and Composites." 2nd edition. New York: Marcel Dekker Inc. (1994): pp. 63-232.
- [111] PANalytical a spectris company, X'Pert³ Powder: (2016). Retrieved from <http://www.panalytical.com/XPert3-Powder.htm>
- [112] Stanjek, H., and W. Häusler. "Basics of X-ray Diffraction." *Hyperfine Interactions* 154, no. 1-4 (2004): 107-119.
- [113] Agilent Technologies, Agilent 4100 ExoScan FTIR, Operation manual: (2013) Retrieved from <http://www.agilent.com/cs/library/usermanuals/public/0023-401.pdf>
- [114] Artisan Technology Group, QTest universal test frames: (2001) Retrieved from https://www.artisanng.com/info/MTS_Qtest_Datasheet.pdf
- [115] Nanyang Technological University (NTU), Singapore: (2016) Retrieved from http://www3.ntu.edu.sg/home/msllew/SOP_%20DynaTup_Charpy.pdf
- [116] Thermo Fisher Scientific, Thermo Scientific K-Alpha X-ray Photoelectron Spectrometer (XPS): (2016) Retrieved from <https://static.thermoscientific.com/images/D12992~.pdf>
- [117] Nicholls, Alan, and Tad Daniel. "X-Ray Photoelectron Spectroscopy: Theory and Practice." Lecture, RRC - Electron Microscopy Service from University of Illinois, Chicago, IL, Fall 2014.
- [118] NC state university, analytical instrumentation facility: (2016) Retrieved from <https://www.aif.ncsu.edu/equipment/jeol-2010f-stem/>

- [119] Rutgers the state university of New Jersey, Institute for advanced materials, Devices and nanotechnology: (2016) Retrieved from <http://iamdn.rutgers.edu/instrumentation/16-home/48-electron-microscopy>
- [120] Yong Ding, "Fundamental Theory of Transmission Electronic Microscopy," Professor Zhong L. Wang's nano research group: (2016) Retrieved from <http://www.nanoscience.gatech.edu/zlwang/research/tem.html>
- [121] Kartel, M., Yu Sementsov, S. Mahno, V. Trachevskiy, and Wang Bo. "Polymer Composites Filled with Multiwall Carbon Nanotubes." *Universal Journal of Materials Science* 4(2): 23-31, 2016.
- [122] Moniruzzaman, Mohammad, and Karen I. Winey. "Polymer nanocomposites containing carbon nanotubes." *Macromolecules* 39, no. 16 (2006): 5194-5205.
- [123] Beyer, Frederick L., and Christopher Ziegler. Wide-Angle X-Ray Scattering Characterization of the Morphology of Nylon 6 6 Obturator Materials. No. ARL-TR-3270. ARMY RESEARCH LAB ABERDEEN PROVING GROUND MD, 2004.
- [124] Bunn, C. W., and E. V. Garner. "The crystal structures of two polyamides ('nylons')." In *Proceedings of the Royal Society of London A: Mathematical, Physical and Engineering Sciences*, vol. 189, no. 1016, pp. 39-68. The Royal Society, 1947.
- [125] Jones, N. A., E. D. T. Atkins, and M. J. Hill. "Investigation of solution-grown, chain-folded lamellar crystals of the even-even nylons: 6 6, 8 6, 8 8, 10 6, 10 8, 10 10, 12 6, 12 8, 12 10, and 12 12." *Journal of Polymer Science Part B: Polymer Physics* 38, no. 9 (2000): 1209-1221.
- [126] Liu, Xiaohui, Qiuju Wu, and Lars A. Berglund. "Polymorphism in polyamide 66/clay nanocomposites." *Polymer* 43, no. 18 (2002): 4967-4972.
- [127] Li, Jidong, Yi Zuo, Xianmiao Cheng, Weihua Yang, Huanan Wang, and Yubao Li. "Preparation and characterization of nano-hydroxyapatite/polyamide 66 composite GBR membrane with asymmetric porous structure." *Journal of Materials Science: Materials in Medicine* 20, no. 5 (2009): 1031.
- [128] Zhang, Xiang, Yu-Bao Li, Yi Zuo, Guo-Yu Lv, Yuan-Hua Mu, and Hong Li. "Morphology, hydrogen-bonding and crystallinity of nano-hydroxyapatite/polyamide 66 biocomposites." *Composites Part A: Applied Science and Manufacturing* 38, no. 3 (2007): 843-848.
- [129] Cheval, Nicolas, Fang Xu, Nabil Gindy, Richard Brooks, Yanqiu Zhu, and Amir Fahmi. "Morphology, crystallinity and thermal properties of polyamide 66/polyoxometalate nanocomposites synthesised via an in situ sol/gel process." *Macromolecular Chemistry and Physics* 212, no. 2 (2011): 180-190.

- [130] Karimi, Hajir, and Aboutaleb Ghadami Jadvall Ghadam. "Synthesis and Characterization of Polyamide-66/Calcium Carbonate Composites." *Journal of Chemical and Petroleum Engineering* 49, no. 1 (2015): 63-78.
- [131] Zhang, Xiaoyan, Xiangmin Xu, and Tao Wu. "Mechanical properties, thermal and crystallization behavior of different surface-modified silica nanoparticle-filled PA66 composites." *Journal of Polymer Engineering* (2017).
- [132] Stepaniak, R. F., A. Garton, D. J. Carlsson, and D. M. Wiles. "The characterization of nylon 6 filaments by x-ray diffraction." *Journal of Applied Polymer Science* 23, no. 6 (1979): 1747-1757.